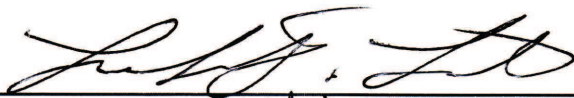Nader A. Naderi
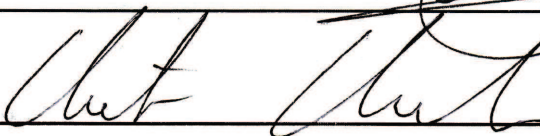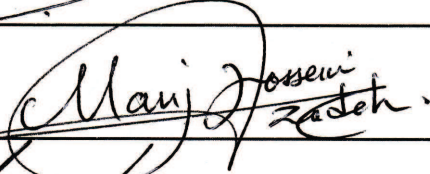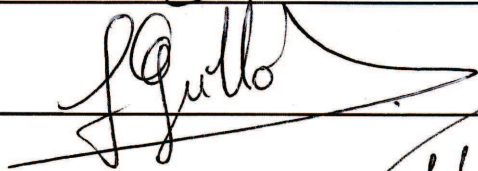_____
Candidate

Electrical and Computer Engineering
_____
Department

This dissertation is approved, and it is acceptable in quality
and form for publication:

Approved by the Dissertation Committee:

_____ , Chairperson

_____

_____

_____

_____

_____

_____

_____

**EXTERNAL CONTROL OF SEMICONDUCTOR
NANOSTRUCTURE LASERS**

BY

NADER A. NADERI

B.S., Applied Physics, University of Mashhad, 2000
M.S., Electrical Engineering, University of New Mexico, 2007

DISSERTATION

Submitted in Partial Fulfillment of the
Requirements for the Degree of

Doctor of Philosophy

Engineering

The University of New Mexico
Albuquerque, New Mexico

July, 2011

ACKNOWLEDGMENTS

I am foremost thankful to my advisor and dissertation committee chairman, Professor Luke Lester for his support and expert guidance throughout the course of this study. His patience and faith in my abilities has inspired me to find my career path and learn a lot in the field of optoelectronics.

In addition, special thanks are due to my thesis committee members Professor Christos Christodoulou, Professor Mani Hossein-Zadeh, and Professor Frederic Grillot who provided me great help and insightful comments in completing this dissertation.

I wish to acknowledge my gratitude to Dr. Yan Li, Dr. Michael Pochet, Dr. Mark Crowley, Nishant Patel and all of my other friends and colleagues at the Center for High Technology Materials, who contributed their valuable assistance and helpful discussions during completion of this research. My sincere thanks also go to Dr. Vassilios Kovanis, and Dr. Nicholas Usechak at the Air Force Research Laboratory, Wright-Patterson AFB, for their helpful advice and assistance during this investigation.

I am truly grateful to my beloved wife Shadi, for her endless support, patience, and understanding through these years. Lastly, I wish to dedicate this achievement to my family for all the love, support and encouragement.

**EXTERNAL CONTROL OF SEMICONDUCTOR
NANOSTRUCTURE LASERS**

BY

NADER A. NADERI

ABSTRACT OF DISSERTATION

Submitted in Partial Fulfillment of the
Requirements for the Degree of

Doctor of Philosophy

Engineering

The University of New Mexico
Albuquerque, New Mexico

July, 2011

External Control of Semiconductor Nanostructure Lasers

by

Nader A. Naderi

B.S., Applied Physics, University of Mashhad, 2000

M.S., Electrical Engineering, University of New Mexico, 2007

Ph.D., Engineering, University of New Mexico, 2011

ABSTRACT

Novel semiconductor nanostructure laser diodes such as Quantum-Dot (QD) and Quantum-Dash (QDash) are key optoelectronic components for many applications such as ultra fast optical communication. This is mainly due to their unique carrier dynamics compared to conventional quantum-well (QW) lasers that enables their potential for high differential gain and modified linewidth enhancement factor. However there are known intrinsic limitations associated with the semiconductor laser dynamics that can hinder its ultimate performance including the mode stability, linewidth, and direct modulation capabilities. One possible method to overcome these limitations is through external control techniques. The electrical and/or optical external perturbations can be implemented to improve the parameters associated with the laser's dynamics, such as threshold gain, damping, spectral linewidth, and mode selectivity. This work studied the

impact of external control techniques through optical injection-locking, optical feedback and asymmetric bias control on the overall performance of the nanostructure lasers in order to understand the associated intrinsic limitations and to develop strategies for controlling the underlying dynamics to improve the laser performance.

In this document, the impact of external control through optical injection-locking on the modulation characteristics of QD and QDash lasers are investigated. Using the conventional rate equations describing an injection-locked system, a novel modulation response function is derived which implicitly incorporates non-linear gain through the free-running relaxation oscillation frequency and damping rate of the slave laser. It is shown that the model presented can be used to accurately model and extract the characteristic parameters of the coupled system directly from measured microwave experimental data. The significance of this modeling approach is that it allows all the external control parameters to be extracted in the frequency domain where they can be easily compared in order to further aid in optimizing the modulation performance of the system. Using the simulation results, the impact of intrinsic slave parameters, including the free-running relaxation oscillation, linewidth enhancement factor, and damping rate, on the injection-locked modulation transfer function are investigated. The impact of ultra-strong optical-injection on the slave linewidth enhancement factor found in QD and QDash lasers are analyzed using theoretical predictions and verified with experimental observations. The experimental findings presented in this dissertation show that the free-running linewidth enhancement factor in nanostructure lasers can be manipulated due to the significant threshold gain shift under strong optical injection. This novel finding along with the enhanced bandwidth advantages offered in the direct modulation of

injection-locked nanostructure lasers promises a path to realizing a new generation of compact, chirp-free, and ultrafast (>100 Gb/s) optical sources for data transmission.

Using an external optical feedback stabilization method and/or asymmetric bias control, a dual-wavelength emission mechanism is realized in a two-section QD distributed feedback (DFB) laser. It is shown that under asymmetric bias conditions, the powers between the ground-state and excited-state modes of the two-section device can be equalized, which is mainly attributed to the unique carrier dynamics of the QD gain medium. It is also found that the combination of significant inhomogeneous broadening and excited-state coupled mode operation allows the manipulation of the QD states through external optical stabilization. The technical design and external control approaches described in this study along with current on-chip photomixing capabilities have potential in engineering a compact and low-cost THz source for future applications.

TABLE OF CONTENTS

x

Chapter 3 123

Manipulation of the Linewidth Enhancement Factor in QDash Nanostructure Laser under Strong Optical Injection

Summary and Conclusion

LIST OF FIGURES

LIST OF TABLES

LIST OF PUBLICATIONS ASSOCIATED WITH THIS STUDY

Refereed Journal Articles and Book Chapter

N. A. Naderi, M. Pochet, F. Grillot, N. Terry, V. Kovanis, L. F. Lester, *"Modeling the Injection-Locked Behavior of a Quantum-Dash Semiconductor Laser,"* IEEE Journal of Selected Topics in Quantum Electronics, Vol. 15, No. 3, pp. 563-571, 2009.

N. A. Naderi, F. Grillot, K. Yang, J. B. Wright, A. Gin, and L. F. Lester, *"Two-Color Multi-Section Quantum Dot Distributed Feedback Laser,"* Optics Express, Vol. 18, No. 26, pp. 27028–27035, 2010.

M. Pochet, **N. A. Naderi**, V. Kovanis, and L. F. Lester, *"Modeling the Dynamic Response of an Optically-Injected Nanostructure Diode Laser,"* IEEE Journal of Quantum Electronics, Vol. 47, No. 6, pp. 827-833, 2011.

M. Pochet, **N. A. Naderi**, Y. Li, V. Kovanis, L. F. Lester, *"Tunable Photonic Oscillators Using Optically Injected Quantum-Dash Diode Lasers,"* IEEE Photonics Technology Letters, Vol. 22, No. 11, pp. 763-765, 2010.

F. Grillot, **N. A. Naderi**, M. Pochet, C.-Y. Lin, and L. F. Lester, *"The Critical Feedback Level in Nanostructure-Based Semiconductor Lasers,"* Book chapter in Semiconductor Technologies, Published by In-Tech, ISBN 978-953-307-080-3, April 2010.

M. Pochet, **N. A. Naderi**, N. Terry, V. Kovanis, L. F. Lester, *"Dynamic Behavior of an Injection-Locked Quantum-Dash Fabry-Perot Laser at Zero Detuning,"* Optics Express, Vol. 17, No. 23, pp. 20623-20630, 2009.

F. Grillot, **N. A. Naderi**, M. Pochet, C.-Y. Lin, P. Besnard, and L. F. Lester, *"Tuning of the Critical Feedback Level in 1.55-μm Quantum-Dash Semiconductor Laser Diodes,"* IET Optoelectronics, Vol. 3, No. 6, pp. 242-247, 2009.

N. B. Terry, **N. A. Naderi**, M. C. Pochet, A. J. Moscho, L. F. Lester and V. Kovanis, *"Bandwidth Enhancement of Injection-Locked 1.3-μm Quantum-Dot DFB Laser"*, Electronic Letters, Vol. 44, No. 15, pp. 904-905, 2008.

F. Grillot, **N. A. Naderi**, M. Pochet, C.-Y. Lin, and L. F. Lester, *"Variation of the Feedback Sensitivity in a 1.55-μm InAs/InP Quantum-Dash Fabry-Perot Semiconductor Laser,"* Applied Physics Letters, Vol. 93, pp. 191108-1-3, 2008.

Conference Proceedings

N. A. Naderi, M. C. Pochet, F. Grillot, A. Shirkhorshidian, V. Kovanis, L. F. Lester, *"Manipulation of the Linewidth Enhancement Factor in an Injection-Locked Quantum-Dash Fabry-Perot Laser at 1550nm,"* In proceedings of the 2010 IEEE/Photonics Society conference in Denver, CO.

N. A. Naderi, M. Pochet, V. Kovanis, L. F. Lester, *"Bandwidth Enhancement in an Injection-Locked Quantum Dot Laser Operating at 1.31-μm,"* In proceedings of the 2010 Photonic West Conference in San Francisco, CA.

N. A. Naderi, M. Pochet, F. Grillot, Y. Li, and L. F. Lester, *"Temperature Effects on the Modulation Response of an Injection-Locked InAs/InP Quantum-Dash Laser,"* In proceedings of the 2009 IEEE/IPRM Conference in Newport Beach, CA.

N. A. Naderi, M. Pochet, F. Grillot, N. Terry, V. Kovanis, L. F. Lester, *"Extraction of Physical Parameters from an Injection-Locked Quantum-Dash Fabry-Perot*

Laser," In proceedings of the 2008 IEEE/LEOS Society Meeting in Newport Beach, CA.

M. Pochet, **N. A. Naderi**, V. Kovanis, L. F. Lester, *"Optical-Injection of Quantum-Dashes Semiconductor Lasers at 1550nm for Tunable Photonic Oscillators,"* In proceedings of the 2011 Photonic West Conference in San Francisco, CA.

F. Grillot, **N. A. Naderi**, C.-Y. Lin, K. Yang, A. Gin, A. Shirkhorshidian, and L. F. Lester, *"Two-Color Quantum-Dot DFB Laser for Terahertz Applications,"* In proceedings of the 2010 IEEE/Photonics Society conference in Denver, CO.

M. Pochet, **N. A. Naderi**, N. Terry, V. Kovanis, L. F. Lester, *"Linewidth Enhancement factor and Dynamical Response of an Injection-Locked Quantum-Dot Fabry-Perot Laser at 1310nm,"* In proceedings of the 2010 Photonic West Conference in San Francisco, CA.

M. Pochet, **N. A. Naderi**, V. Kovanis, L. F. Lester, *"Optically Injected Quantum Dash Lasers at 1550nm Employed as Highly Tunable Photonic Oscillators,"* In proceedings of the 2010 CLEO/QELS Conference in San José, CA.

F. Grillot, **N. A. Naderi**, M. Pochet, C.-Y. Lin, and L. F. Lester, *"Influence of the Linewidth Enhancement Factor on the Critical Feedback Level in a Quantum Dash Laser,"* In proceedings of the 2009 CLEO/IQEC Conference in Baltimore, MD.

F. Grillot, **N. A. Naderi**, M. C. Pochet, C.-Y. Lin, P. Besnard, and L. F. Lester, *"Tuning of the Critical Feedback Level in 1.5-μm Quantum Dot Semiconductor Lasers,"* In proceedings of the 2009 SIOE Conference in Cardiff, United Kingdom.

F. Grillot, **N. A. Naderi**, M. C. Pochet, C.-Y. Lin, and L. F. Lester, *"Systematic Investigation of the Alpha Parameter Influence on the Critical Feedback Level in*

QD Lasers," In proceedings of the 2009 Photonic West Conference in San José, CA.

M. Pochet, **N. A. Naderi**, F. Grillot, N. Terry, V. Kovanis, L. F. Lester, *"Methods for Improved 3dB bandwidth in an Injection-Locked QDash Fabry Perot Laser at 1550nm,"* In proceedings of the 2009 CLEO/IQEC Conference in Baltimore, MD.

M. Pochet, **N. A. Naderi**, F. Grillot, N. Terry, V. Kovanis, L. F. Lester, *"Modulation Response of an Injection Locked Quantum-Dash Fabry Perot Laser at 1550nm,"* In proceedings of the 2009 Photonic West Conference in San José, CA.

V. Kovanis, N. G. Usechak, **N. A. Naderi**, M. Pochet, and L. F. Lester, *"Ultrafast Diode Lasers Via Strong Optical Injection,"* In proceedings of the 2009 ETOPIM Conference in Crete, Greece.

F. Grillot, **N. A. Naderi**, M. C. Pochet, C.-Y. Lin and L. F. Lester, *"Variation of the Critical Feedback Level in a 1550nm Quantum-Dash Fabry-Perot Semiconductor Laser,"* In proceedings of the 2008 IEEE/LEOS Society Meeting in Newport Beach, CA.

L. F. Lester, N. B. Terry, A. J. Moscho, M. L. Fanto, **N. A. Naderi**, Y. Li, and V. Kovanis, *"Giant nonlinear gain coefficient of an InAs/AlGaInAs quantum dot laser,"* In proceedings of the 2008 SPIE Photonic West Conference in San José, CA.

N. Terry, **N. A. Naderi**, M. C. Pochet, L. F. Lester, *"3-dB Bandwidth Enhancement via Strong Optical Injection-Locking of a Quantum Dot DFB at 1310 nm,"* In proceedings of the 2008 IEEE/LEOS Society Meeting in Newport Beach, CA.

Y. Li, **N. A. Naderi**, V. Kovanis, L. F. Lester, *"Modulation Response of an Injection-Locked 1550 nm Quantum Dash Semiconductor Laser,"* In proceedings of the 2007 IEEE/LEOS Society Meeting in Lake Buena Vista, FL.

<u>Other Publications</u>

Y. Li, **N. A. Naderi**, V. Kovanis, L. F. Lester, *"Enhancing the 3-dB Bandwidth via the Gain-Lever Effect in Quantum-Dot Lasers,"* IEEE Photonics Journal, Vol. 2, No. 3, pp. 321-329, 2010.

C.-Y. Lin, F. Grillot, **N. A. Naderi**, Y. Li, and L. F. Lester, *"RF Linewidth Reduction in a Quantum Dot Passively Mode-Locked Laser Subject to External Optical Feedback,"* Applied Physics Letters, Vol. 96, No. 5, pp. 051118, 2010.

J. H. Kim, C-Y. Lin, **N. A. Naderi**, Y.-C. Xin, L. F. Lester and C. G. Christodoulou, *"Pattern Estimation of a Microstrip Antenna Integrated With a Quantum Dot Mode-Locked Laser,"* IEEE Antennas and Wireless Propagation Letters, Vol. 9, pp. 954-957, 2010.

F. Grillot, C.-Y. Lin, **N. A. Naderi**, M. Pochet, L. F. Lester, *"Optical Feedback Instabilities in a Monolithic InAs/GaAs Quantum Dot Passively Mode-Locked Laser,"* Applied Physics Letters, Vol. 94, pp. 153503-1-3, 2009.

J. H. Kim, C. G. Christodoulu, Z. Ku, C.-Y. Lin, Y.-C. Xin, **N. A. Naderi**, and L. F. Lester, *"Hybrid Integration of a Bowtie Slot Antenna and a Quantum Dot Mode-Locked Laser,"* IEEE Antennas and Wireless Propagation Letters, Vol. 8, pp. 1337-1340, 2009.

N. G. Usechak, **N. A. Naderi**, M. Grupen, Y. Li, L. F. Lester, and V. Kovanis, *"Cavity-Enhanced Modulation in Gain-Lever Semiconductor Lasers,"* In proceedings of the 2010 IEEE/Photonics Society conference in Denver, CO.

C.-Y. Lin, F. Grillot, **N. A. Naderi**, Y. Li, L. F. Lester, *"Ultra-low RF Linewidth in a Quantum Dot Mode-Locked Laser Under External Optical Feedback Stabilization,"* In proceedings of the 2010 CLEO/QELS Conference in San José, CA.

J. H. Kim, C.-Y. Lin, Y. Li, **N. A. Naderi**, C. G. Christodoulou, and L. F. Lester, *"Beam steering of a linearly tapered slot antenna array integrated with quantum dot mode-locked lasers,"* In proceedings of the 2010 IEEE/Photonics Society conference in Denver, CO.

C.-Y. Lin, **N. A. Naderi**, F. L. Chiragh, J. Kim, C. G. Christodoulou and L. F. Lester, *"31% DC to RF Differential Efficiency Using Monolithic Quantum Dot Passively Mode-Locked Lasers,"* In proceedings of the 2009 CLEO/IQEC Conference in Baltimore, MD.

J. H. Kim, C. G. Christodoulou, Z. Ku, C.-Y Lin, **N. A. Naderi**, L. F. Lester, J. P. Kim, *"A Bowtie Slot Antenna coupled to a Quantum-Dot Mode Locked Laser,"* In proceedings of the 2009 IEEE International Symposium on Antennas and Propagation and USNC/URSI (U.S. National Committee of the International Union of Radio Science) in Charleston, SC.

C.-Y. Lin, Y.-C. Xin, **N. A. Naderi**, F. L. Chiragh and L. F. Lester, *"Monolithic 1.58-micron InAs/InP quantum dash passively mode-locked lasers,"* In proceedings of the 2009 Photonic West Conference in San José, CA.

F. Grillot, C.-Y. Lin, **N. A. Naderi**, M. Pochet, and L. F. Lester, *"Effects of Optical Feedback in InAs/GaAs Monolithic Quantum Dot Passively Mode-Locked Lasers,"* In proceedings of the 2009 CLEO/IQEC Conference in Baltimore, MD.

J. H. Kim, C. G. Christodoulou, L. F. Lester, Y.-C. Xin, **N. A. Naderi**, Z. Ku, *"Quantum-Dot Laser Coupled Bowtie Antenna,"* In proceedings of the 2008 IEEE International Symposium on Antennas and Propagation and USNC/URSI in San Diego, CA.

Y. Li, **N. A. Naderi**, Y.-C. Xin, C. Dziak, and L. F. Lester, *"Multi-section gain-lever quantum dot lasers,"* In proceedings of the 2007 Photonic West Conference in San José, CA.

Y. Li, **N. A. Naderi**, Y.-C. Xin, V. Kovanis, L. F. Lester, *"Two-Section Quantum Dot Lasers with 20-dB Modulation Efficiency Improvement,"* In proceedings of the 2007 CLEO/QELS Conference in Baltimore, MD.

N. A. Naderi, Y. Li, C. Dziak, Y. C. Xin, V. Kovanis, L. F. Lester, *"Quantum Dot Gain-Lever Laser Diode,"* In proceedings of the 2006 IEEE/LEOS Society Meeting in Montreal, Canada.

Chapter 1

External Control Techniques in Semiconductor Nanostructure Lasers

1.1   Introduction

Semiconductor coherent light-emitting diodes are one of the key optoelectronic components that have been widely used in many fields such as ultrafast optical communication systems, spectroscopy, remote sensing, and optical data storage. The intrinsic dynamics of semiconductor lasers are unique depending on their structural design and the make-up of their material system. Over the past 50 years there have been many efforts devoted to improving semiconductor laser performance by improving the internal laser properties through the invention of novel semiconductor material systems and designing better cavity structures or by implementing external control techniques to enhance the laser characteristics. With the developments in crystal growth technology and the invention of novel semiconductor materials, the internal performance of semiconductor lasers has been significantly improved over the past few decades. The following is an up-to-date and brief summary of the advancement in growth of novel semiconductor structures used in laser devices.

A definite breakthrough in the field of semiconductor lasers was the invention of double heterostructure (DH) lasers in 1963 [1] in which both carrier and optical mode confinement [2]-[6] improvements resulted in reduction of the threshold current density and also enabled continuous wave (CW) operation at room temperature[7], [8]. Further

1

developments in semiconductor material systems were achieved by advancements in crystal growth techniques and realizing the concept of quantum size effects which resulted in the first demonstration of a quantum well (QW) laser structure in 1977 [9], [10]. In the QW material system, the carriers are confined within quantized energy levels due to the reduction in the physical space volume in one dimension which helps to reduce the threshold current density and allows for control of the lasing wavelength by changing the quantum well thickness [11]-[12]. The advantages of one dimensional confinement in QWs motivated more efforts to study the higher orders of carrier confinement, which lead to the development of new nanostructure materials systems such as quantum dot (QD) and quantum dash (QDash) [13]-[15]. The interest in QD and QDash arises from their unique carrier dynamics resulting form three-dimensional (3-D) carrier confinement. This confinement in all directions leads to discrete quantized energy levels that can be controlled by changing the size and shape of the nanostructures. Predicted by Arakawa *et. al*, semiconductor laser active regions made from 3-D confinement systems should exhibit better internal performance compared to QW active region lasers [16], [17]. The potential internal improvements in QD materials have been experimentally verified on actual laser devices, which include low transparency current density [18], less temperature dependence of threshold current density [19], increased gain and differential gain [17], and a reduced linewidth enhancement factor [20]. Despite all the improvements made in 3-D confinement material systems, there are still several limitations associated with their carrier dynamics that can hinder the ultimate laser performance including the mode stability, linewidth, and direct modulation capabilities.

A clear example of these limitations can be seen in the direct modulation of semiconductor lasers. Directly-modulated semiconductor lasers have become one of the most efficient candidates for high-speed communication in microwave frequencies because of their compactness and relatively low fabrication cost. Compared to external modulation techniques, directly-modulated lasers commonly used in optical fiber link, have simpler driver electronics and lower power consumption. Direct modulation involves changing the current input around the bias level above threshold. It is principally a simpler method and is easier to implement rather than external modulation, but the output light produced depends on the laser's complex internal dynamics. For instance, compared to QW lasers, higher gain and differential gain in nanostructure QD lasers would typically be expected to contribute to a larger modulation bandwidth [21]. Furthermore QD nanostructure lasers are known to exhibit near zero linewidth enhancement factors at threshold which theoretically predicts a chirp-free direct modulation performance [20]. In reality, strong gain saturation with carrier density in QD lasers as result of inhomogeneous broadening prevents the laser from reaching its ultimate high-speed performance. This is because the strong gain saturation in QDs causes both the damping effect and the linewidth enhancement factor to significantly increase with carrier density [22].

In general, high frequency chirp, small relaxation oscillation frequency, limited output power, excessive noise, and high distortion limit the high-speed performance of semiconductor lasers to transmissions at bit rates below 40 Gb/s. In order to improve the modulation characteristics, such as obtaining higher modulation bandwidth or minimal

frequency chirp, we need to be able to control and manipulate some of the intrinsic laser parameters such as optical gain and/or the linewidth enhancement factor.

1.2   Motivation for this Study

One possible method for improving the overall performance of semiconductor lasers is through various external control techniques. The original interest in using external control techniques in semiconductor lasers is motivated from a desire to understand the associated limitations and instabilities and to develop strategies for controlling the underlying dynamics to improve the laser performance. Using these techniques, external electrical and/or optical perturbations can affect the parameters associated with the laser's dynamics, such as threshold gain, damping, spectral linewidth, and mode selectivity. The external perturbations can often produce undesired instabilities in the laser, but they can be well controlled to produce desirable laser properties including improvement in the modulation characteristics and spectral stability.

The objective of this work is to implement common external control techniques to investigate their impact on the overall behavior of nanostructure lasers with a focus on improvement in direct modulation performance and spectral characteristics. The external control techniques studied in this dissertation include optical injection-locking, optical feedback, and asymmetric bias control. These techniques were previously studied thoroughly in bulk and QW lasers, but very little is known about the impact of external control on performance of nanostructure lasers including modulation characteristics and wavelength stability.

The work presented in this dissertation initially focuses on modeling the direct modulation behavior of injection-locked QD and QDash nanostructure lasers under strong optical injection and stable locking conditions. The existing modulation response model is reformulated using small-signal analysis of the coupled rate equations of the master and slave lasers. As a result, a novel modulation response function is developed that allows one to extract the key operating parameters of the system directly from measured microwave response data. The significance of this modeling approach is that it allows all the external control parameters to be extracted in the frequency domain where they can be easily compared in order to further aid in optimizing the modulation performance of the system. The model presented incorporates the impact of nonlinear gain, which is known to be significant in QD and QDash lasers, along with the field enhancement factor relating the deviation of the steady-state slave field amplitude from its free-running value at high injection strengths. This is one of the major differences in modeling the modulation response of an injection-locked QD and QDash laser. Using the simulation results, the impact of intrinsic slave parameters, including the free-running relaxation oscillation, linewidth enhancement factor, and damping rate, on the injection-locked modulation transfer function are studied.

Unique carrier dynamics in nanostructure lasers allows for the linewidth enhancement factor to fluctuate within a large range in these devices [23]. Previous studies found that the linewidth enhancement factor in nanostructure QD and QDash lasers strongly depends on the photon density due to the gain compression enhancement with carrier density in theses devices [22]. This work aims to investigate the impact of strong optical injection on the slave linewidth enhancement factor found in QD and

QDash lasers. The theoretical predictions and experimental findings presented in this dissertation show that the free-running linewidth enhancement factor in QDash lasers can be manipulated due to the significant threshold gain shift under strong optical injection. This novel finding along with the enhanced bandwidth advantages offered in the direct modulation of injection-locked nanostructure lasers promises a path to realizing a new generation of compact, chirp-free, and ultrafast (>100 Gb/s) optical sources for data transmission.

The second part of the dissertation focuses on generating dual-color emission in a single laser diode by using the external control techniques of optical feedback and asymmetric pumping. The device used for the dual-color demonstration was a two-section QD Distributed Feedback (DFB) laser diode with the Bragg wavelength only coupled to the excited state. Specifically, this part of the dissertation describes in detail how the dual-color operation is realized through simultaneous ground state emission that is uncoupled to the Bragg grating due to significant inhomogeneous broadening common in QD active region. In previous works, high performance dual-color optical sources have been intensively studied for terahertz (THz) signal generation using photomixing techniques [24]. Considering that the existing THz generation techniques are mostly reliant on bulk optics, this work was motivated by the need for compact and low-cost THz sources using externally controlled semiconductor lasers. In this study the technical design and fabrication of the two-section QD DFB laser diode is described. With the DFB device biased well above its threshold, it is shown that either applying external optical feedback or asymmetric pumping generates two single-mode emission peaks in the optical spectra–one line from the ground state and the other from the excited state.

The origin of this dual-color mechanism is shown to be associated with manipulating the QD carrier dynamics through controlled external perturbations provided by optical feedback and/or asymmetric pumping. The technical design and external control approaches described in this work along with current on-chip photomixing capabilities have potential in engineering a compact and low-cost CW THz source for future applications.

The following sections provide general overviews and applications of the external control techniques studied in this dissertation.

1.2.1   Optical Injection-Locking

Overview of the Injection-Locking Technique

Optical injection-locking of semiconductor lasers involves two laser diodes often referred to as the master and slave lasers as shown in Figure (1.1). There are two configurations of injection-locking systems. One choice is to inject the master light into one of the slave's facets and collect the light from the other facet. Usually an optical isolator is placed between the master and slave lasers to prevent reflections back to the master. In a simpler configuration, an optical circulator can be used such that the light from the master is injected from one slave facet and the output is collected from the same facet. The latter method is easier since it only requires one fiber coupled to the slave laser. The master laser is usually a single-mode, low linewidth, and high power tunable laser. Several commercially available laser sources can be used as the master, including external cavity lasers with wide wavelength tunability and highly linear, high-power butterfly-packaged DFB lasers capable of wide temperature tuning of the wavelength.

7
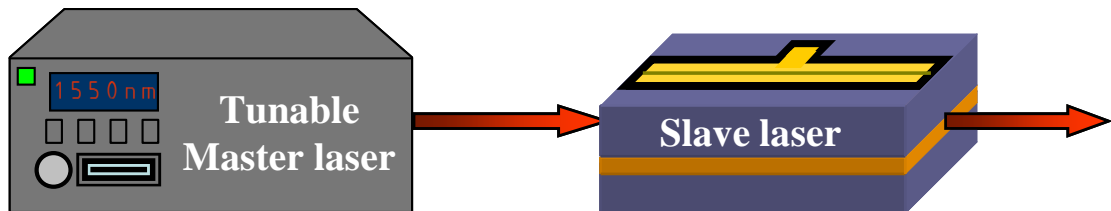
Figure (1.1) Schematic diagram of an optically injection-locked laser system. The red arrows represent the light emission from each laser. This is the less common configuration for the coupled system. Both mirrors of the slave laser in this arrangement would have to be partially reflecting. The more advance version, which uses an optical circulator between the master and slave lasers, is shown in chapter 2, Figure (2.3).
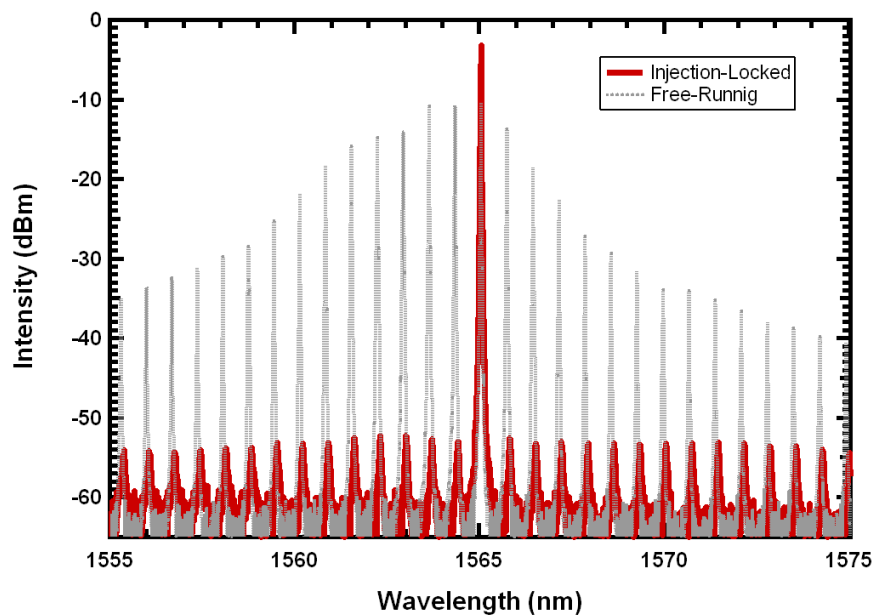
Figure (1.2) Optical spectra of an injection-locked Fabry-Perot Laser.

When the locking conditions are satisfied, the frequency of the slave is locked to that of the master with a constant phase offset. Figure (1.2) shows measured optical spectra of a Fabry-Perot (FP) slave laser with and without optical injection. As shown in this figure, optical injection suppresses all FP modes, resulting in single mode operation.

There are two primary injection-locking parameters; frequency detuning Δf, and external injection ratio, R_{ext}. Frequency detuning is defined as the frequency offset between master and slave laser. The external injection ratio is the master to slave power ratio at the slave emitting facet. As the frequency of the master is changed, the slave mode will follow that frequency until the system becomes unlocked. The locking range depends on several parameters including the external power ratio, coupling coefficient and linewidth enhancement factor of the slave laser.

A Brief History of Optical Injection-Locking

The concept of frequency locking between two coupled oscillators has attracted many researchers for centuries. The idea goes back to the 17th century, when Huygens discovered the synchronization phenomenon between two clock pendulums mounted on the same wall [25]. It was not until the early 1980s that the fundamental theory and the idea of frequency synchronization between two semiconductor lasers was first studied by Lang [26] and the benefits of this technique on actual devices was verified [27]. Most of the early research was focused on weak optical injection which typically yields a small locking range. It was found that this regime leads to unstable locking regime that exhibits resonant oscillation sidebands and chaotic behaviors [26], [28]-[32]. By the mid 1980s, further developments on the injection-locking technique explored the advantage of the

9

stable injection-locking in semiconductor lasers. It was found that using optical injection-locking as an external control technique in CW lasers can significantly reduce the laser's spectral linewidth and noise [33], [34]. These findings were considered as the most important benefits of optical injection-locking. In the meantime, with the advancement in laser designs and efficient material systems, the advantages of injection-locking on directly modulated lasers for applications such as coherent optical communications was realized [35], [36]. The improvements to the modulated free-running slave laser due to injection-locking include an enhancement in the relaxation oscillation, a reduction in laser relative intensity-to-noise (RIN), a reduction in nonlinear distortion, and most importantly reduction in linewidth and chirp [28], [37]-[46].

Typically, the modulation bandwidth of free-running semiconductor lasers is limited as a result of the resonance frequency and damping rate set by the *K-factor* [47]. It has been shown that the resonance frequency enhancement with optical injection-locking can result in improving the overall bandwidth [48]-[52]. Figure (1.3) shows the experimental results of an optically injection-locked laser demonstrating this improvement. The characteristics of the modulation response curves in Figure (1.3) are shown to vary as a function of the frequency detuning for constant injection strength. It is important to note that improvement of the modulation bandwidth does not always include the enhancement of the 3-dB bandwidth with resonance frequency. This is due to the occurrence of the pre-resonance dip observed at specific detuning conditions as shown in Figure (1.3). Depending on the detuning condition, enhanced modulation response of an injection locked laser can fall into broadband or narrowband regimes of operation as illustrated in Figure (1.3). Using optical injection-locking, a narrowband response with >80 GHz
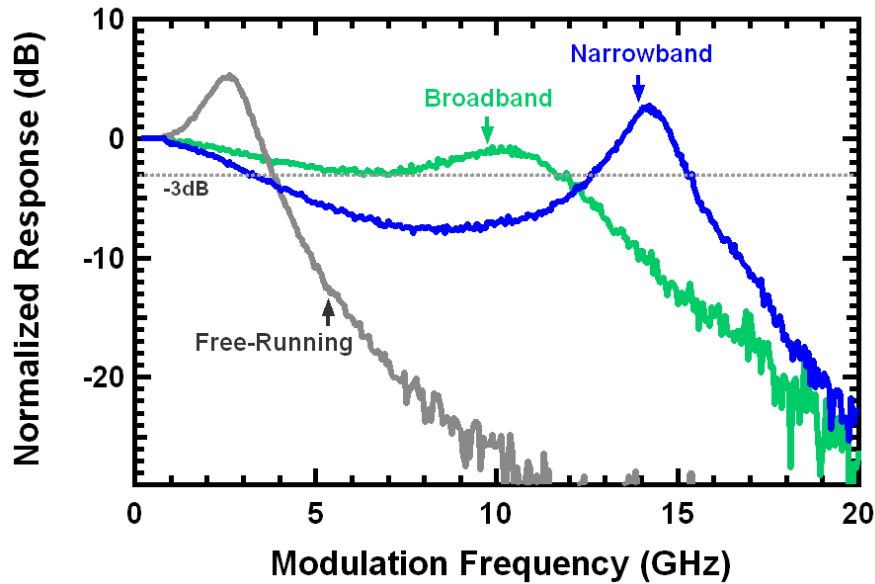
Figure (1.3) Measured modulation responses of an injection-locked FP laser, for various detuning conditions, indicating free-running, broadband and narrowband responses.

intrinsic bandwidth has been reported in a QW vertical cavity surface emitting laser (VCSEL) operating at 1510 nm [53]. Hwang *et. al* have demonstrated a two-fold improvement in the broadband response compared to the free-running case on a DFB laser at 1310 nm under strong optical injection [52].

Another important improvement in optically injection-locked systems over the free-running lasers is the reduction in linewidth and chirp. One important figure of merit in directly modulated free-running lasers is the bit rate-length (BL) product. Limited transmission distances in optical fiber links are mainly due to the linewidth broadening caused by frequency chirp. Reduced chirp by injection-locking decreases the linewidth broadening thereby reducing the pulse broadening caused by dispersive fibers. This important feature of injection-locking was reported to create low chirp, allowing for long-haul transmission with improved BL product [35].

Applications of Optically Injection-Locked Lasers

Recently, the external control technique of free-running lasers through optical injection-locking has been implemented in several state-of-the-art applications including millimeter-wave generation [54], all-optical signal processing [55], radio over fiber [56], and cable access TV (CATV) [57].

Goldberg *et al.*, first demonstrated millimeter-wave generation by the sideband injection-locking technique with sub-Herz RF linewidths [58], [59]. In this technique, two slave lasers were coherently coupled by locking them to the adjacent sidebands of the master laser. Using the millimeter carrier signal generated by sideband injection-locking, a 64 GHz carrier for data transmission at a rate of 155 Mb/s over ~13 km single mode fiber was demonstrated [60], [61]. With the new advancements in the field of millimeter wave generation using optically injection-locked sources, more compact designs along with tunability features have been developed that use only one modulated slave and a master laser as demonstrated in an injection-locked two-section DFB device [62], [63].

Pulse broadening due to fiber dispersion is one of the major limitations in long-haul digital communication systems. To prevent the in-line data loss and increased bit error rate, several electro-optical repeaters are typically required to regenerate and reshape the optical signal along the fiber link. The main drawback of using these repeaters is that they increase the cost and complexity of the system and they also introduce additional speed limitations as a result of electrical to optical and optical to electrical conversions. Fortunately, all-optical signal regeneration and pulse reshaping have been realized through a side-mode injection-locked DFB laser and a double injection-locked FP laser [64], [65]. This technique is based on switching the locking stability as a function of

injection strength. At a fixed frequency detuning, the locking threshold condition of the slave laser defines the lock or unlock states in the coupled system. In this method, the master laser is modulated with the digital signal and then it is weakly injection-locked into a side-mode of a DFB slave laser. At a digital "1" state, the injected power is enough to lock the master to slave and the slave output contains the master frequency information. At a digital "0" state, small injected power leads to the unlocked situation, and the output will be that of the slave. A bandpass filter is typically used to only transmit the master frequency at the output. Therefore, the abrupt threshold of the locking and unlocking processes is used to reshape the distorted signals, resulting in a frequency modulated signal with reduced noise.

Improved modulation characteristics of optical injection-locked lasers including the enhanced bandwidth and reduced chirp have been implemented in radio-over-fiber and CATV applications [56], [57]. In a recent study, the external optical injection technique has been employed in a hybrid radio-over-fiber system to improve the bit error rate performance [56]. Using the resonance frequency enhancement in an injection-locked DFB laser modulated with 125 Mb/s digital signals, narrowband transmission at the sharp resonance peak is demonstrated. A similar approach has been applied to a CATV transmission experiment using a directly modulated DFB laser under strong optical injection. The modulated signals were up-converted to the enhanced resonance frequency at 18.5 GHz and transmission parameters were compared to the baseband free-running transmission values. Comparing the transmission experiments under strong optical injection with the free-running results showed a 3-dB improvement in composite second

order (CSO) and composite triple beat (CTB) performances over a 100 km single mode fiber transmission [57].

1.2.2 External Control through Optical Feedback

Overview of External Optical feedback

Semiconductor lasers subjected to external optical feedback are known to exhibit very interesting nonlinear dynamics, which either lead to instabilities and chaotic behaviors at the laser output or result in practically useful impacts that can improve the device's intrinsic characteristics. Commercial application of semiconductor lasers in optical fiber links was the first practical motivation for studying the behavior of semiconductor lasers subject to optical feedback. Even a small back reflection from the fiber pigtail tip or optical fiber connectors into the diode laser module was shown to degrade the modulation characteristics and increase the intensity noise [66], [67]. To prevent these undesired effects, the laser diode transmitter modules are usually accommodated with an optical isolator which rejects any back reflection but increases the cost of using laser diodes in optical fiber links.

In 1980, Lang and Kobayashi reported on some aspects of the statics and dynamics of the semiconductor laser exposed to the external optical feedback from a distant reflector [68]. In that study, the authors brought to light the intrinsic characteristics of laser gain media including the broad gain spectrum, temperature dependence of the material refractive index, and the carrier density dependence of the refractive index, each exhibiting complex behavior under external feedback conditions. They also reported on

experimental observation of bistability and hysteresis in the laser output light output as a function of injected current characteristics.

Since then, understanding the effects of optical feedback on both dynamical and spectral features of semiconductor lasers has been pursued extensively [69]-[71]. Early studies on the spectral characteristics showed that the laser linewidth could be either narrowed [70] or broadened [69] under the influence of optical feedback. These behaviors were initially understood through the spectral response sensitivity to the phase of the reflected light. Goldberg *et. al* have demonstrated that by changing the feedback parameters somewhat, multi-stability can be observed as the system performs "*mode-hops*," where a laser diode operates on a single external cavity mode for some time, but then suddenly switches to another [72]. Another form of bistability, referred to as "*low-frequency fluctuations*" was studied by Mørk *et. al* [73]. This form of instability is observed when the laser is pumped close to the threshold and is subject to moderate feedback levels. At this condition, laser output shows sudden drops followed by a gradual build-up. The noise properties of semiconductor lasers subject to optical feedback have attracted considerable theoretical and practical interest [74], [75]. More generally, much effort has been devoted to modeling the impact of optical feedback on the dynamical behavior of semiconductor lasers [76], [77].
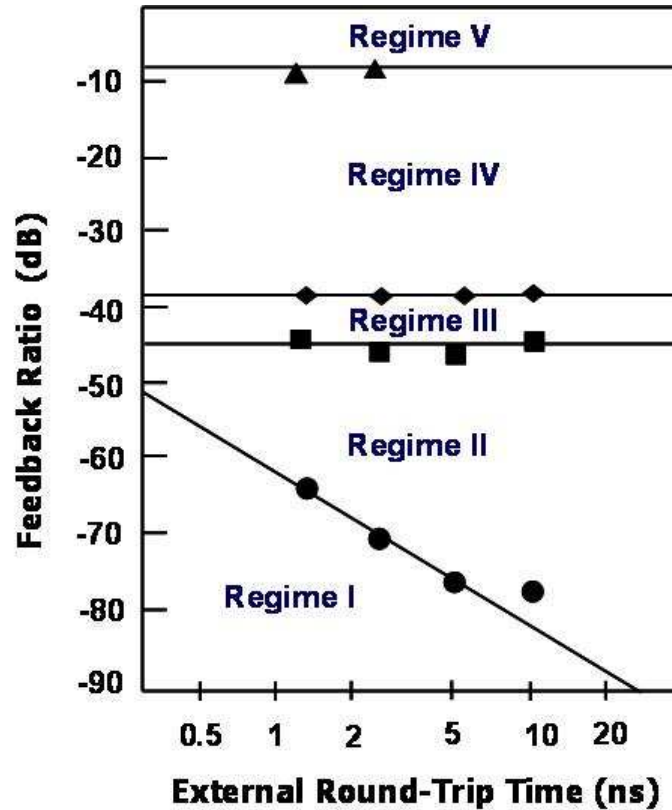
Figure (1.4) Regimes of optical feedback for a DFB laser indicating the feedback power ratio at which the transition between regimes occur as a function of external round-trip time [79].

Regimes of Optical Feedback

It has been experimentally and theoretically shown that the effects of external optical feedback on laser dynamics or spectral properties can be different depending on several factors including the laser bias condition, strength and phase of optical feedback, and the distance between the external reflector and the laser cavity [78]. It was based on these observations that Tkach and Chaprlyvy first experimentally introduced "*the regimes of optical feedback*" in semiconductor lasers [79]. In that study, five identifying operating regimes of feedback were characterized by reference to either the dynamical or spectral properties of the laser and conventionally labeled as regimes I to V as shown in Figure

(1.4). In regime I, under weak feedback levels, the laser linewidth can be either narrowed or broadened depending upon the phase of the optical feedback. Regime II is characterized by the appearance of longitudinal mode hopping. In regime III the laser becomes stable and locks to the mode with minimum single-mode linewidth. In regime IV, with increasing feedback level, the linewidth of the laser dramatically broadens. This phenomenon is referred to as "*coherence collapse.*" Further increasing the feedback strength into regime V, the laser enters a stable external cavity mode operation. There have been extensive studies made of the five feedback regimes of semiconductor laser operation [74]. In particular, considerable effort has been given to determining the nature of the laser dynamics in the coherence collapse regime, or regime IV, as it was first reported by Lenstra *et al*. [80].

Advantages of Controlled Optical Feedback

As mentioned before, optical feedback has been shown to produce deleterious effects on semiconductor lasers including significant linewidth broadening and mode-hopping. However, based on the observed impacts on the dynamical and spectral properties, controlled external feedback is predicted to have much potential in stabilizing and improving laser performance. Recent advancements in modeling the nonlinear dynamics of semiconductor lasers subject to optical feedback have provided a path to understand the associated instabilities and develop methods for controlling the useful underlying dynamics for practical applications [76], [80].

Advantages of controlled feedback have been realized in earlier studies where it was showed that adjusting the feedback level and phase matching can result in a stable

17

operation with considerable spectral linewidth narrowing [81]. Coherent feedback control has also been found to be useful in enhancing the relaxation oscillations and reducing the signal distortion in the modulated laser output [82]. These effects are very important for the laser especially when it is implemented in coherent communication systems.

In another control method of optical feedback, a frequency filter is typically used to access a desired dynamical behavior in a specific region by restricting the phase space that is available to the feedback laser system [83]. Lately, the idea of controlling the nonlinear dynamical behavior in semiconductor lasers has been developed to utilize chaotic dynamics in applications such as chaos synchronization for secure communication systems [84]. The filtered optical feedback technique has become an interesting topic [85], since it can control the laser dynamics through two external parameters: the spectral width of the filter and frequency detuning of the free-running laser. The frequency filter method was shown to provide a mechanism for controlling the impact of relaxation oscillations on the dynamical response of the laser as well as permitting an external control over the nonlinearities of the device [83]. Using this approach, tunable and pure frequency oscillations in the solitary laser can be generated by detuning the frequency of the optical feedback through a Fabry-Perot resonator [86].

The external control through delayed optical feedback has recently found its way into the field of semiconductor passively mode-locked lasers. Recent studies have been both experimentally and theoretically shown that controlled external optical feedback is a simple and efficient method to improve the RF linewidth and timing stability via reducing the RF phase-noise in passively mode-locked lasers [87], [88].

Applications of Semiconductor Lasers with External Optical Feedback

Applications of semiconductor lasers with controlled external optical feedback are driving rapid developments in theoretical and experimental research. The very broad gain-bandwidth of semiconductor lasers combined with frequency-filtered, strong optical feedback create the tunable, single frequency laser systems utilized in telecommunications, environmental sensing, measurement and control [89]. Those with weak to moderate optical feedback levels lead to the chaotic semiconductor lasers which can be implemented in secure communication systems [90].

1.2.3 External Control through a Monolithic Multi-Section Design

In the early1960s, after the invention of DH semiconductor lasers, stabilizing the single-longitudinal mode operation in semiconductor lasers was one of the most important challenges in developing high bit rate and single mode fiber transmission systems [91]. For this reason, several optical integration approaches have been proposed including, but not limited to: external cavity lasers with spherical mirrors, distributed Bragg reflector (DBR) lasers, cleaved-coupled cavity (C^3) lasers, and monolithic two-section lasers. The idea of developing coupled-cavity lasers [92] was initially based on a simple method to improve the single-mode stability under high modulation frequencies and temperature fluctuations in semiconductor lasers [93]. A similar idea was later proposed to implement a coupled-cavity design for controlling the laser output, such as wavelength tuning, by separately pumping the individual cavity [94].

The 1980s saw rapid development of new designs and theoretical studies for coupled-cavity lasers [95]-[97]. With further developments in device fabrication

techniques, monolithic multi-section lasers, a cousin of the C^3 laser, have become readily available for new research topics and developing applications including direct modulation, passive mode-locking, and wavelength tuning [98]-[101]. Samples of the interesting applications for multi-section laser devices are presented below.

Optical Gain-Lever

The optical gain-lever was first realized by K. J. Vahala, *et al*. in 1989 by demonstrating the enhancement in modulation efficiency produced by either optical or electrical modulation of laser cavity [102]. Before that, the idea of producing parasitic-free modulation in semiconductor lasers was developed using a technique called "active layer photo-mixing" [103]. In this method, the light produced by two single mode laser sources was mixed and optically pumped the active layer of another laser diode, producing a carrier density modulation. In 1989, N. Moore and K. Y. Lau [104] suggested that a two-segment configuration in a laser diode could be used to produce a net gain in the conventional carrier modulation of semiconductor lasers. Specifically, Lau studied the optical gain-lever effect to enhance the efficiency of direct intensity modulation and optical frequency modulation of a two-section QW laser [105].

Figure (1.5) shows the schematic view of the two-section gain-lever configuration with a typical gain versus carrier density characteristic of a semiconductor laser. In the two-section laser, each section is biased at different pump levels, where the net bias results in a lasing condition. As shown in Figure (1.5), under asymmetric current injection, the short section (a) referred to as the modulation section, is DC biased at a lower gain level than the long section (b) termed the gain section. This Bias scheme
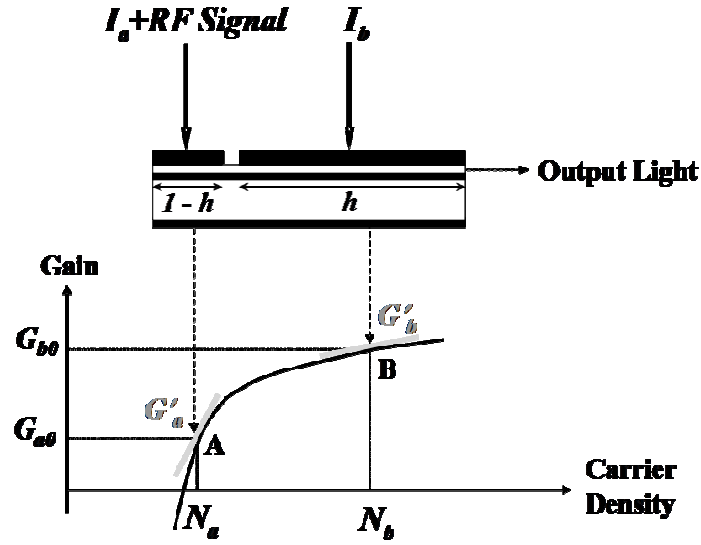
Figure (1.5) Schematic diagram of a two-section gain-lever semiconductor laser with the evolution of gain versus carrier density [106].

provides a high differential gain under small-signal RF modulation. The gain section is only DC biased and provides most of the optical amplification, but at a relatively smaller differential gain. Since the total gain is clamped above the threshold and due to the non-linear dependence of gain with carrier density, any small change in carrier density in the modulation section produces a much larger variation in carrier density in the gain section and consequently in the total photon density. In such a case an RF optical gain will result when the differential gain in the modulation section, G'_a, is greater than the differential gain in the gain section, G'_b.

Recently, much research work based on the gain-lever effect has been conducted to improve modulation characteristics of QD nanostructure lasers. 8 dB and 20 dB intensity modulation efficiency enhancements were demonstrated using p-doped and un-doped QD lasers respectively [106], [107]. It was also theoretically and experimentally demonstrated that under an extreme asymmetric bias configuration, a QD laser

21

employing the gain-lever can exhibit a two-fold enhancement in the 3-dB bandwidth compared to a regular single-section QD laser [108].

Multi-Section DFB/DBR Lasers

Tuning the laser frequency is very important for a variety of applications in coherent optical communication, such as wavelength division multiplexing (WDM), heterodyne detection systems, frequency modulation, and optical switching in local area networks [98], [100], [109]. Depending on the application, the tuning mode, range, and speed requirements are different. Usually for WDM applications, large and continuous frequency tuning is desired (>1 THz), while the frequency modulation requires small but fast frequency shifts (<1 GHz) [110].

Monolithic multi-section DFB lasers were shown to have potential for stable single-mode operation and fast tuning performance [110]. The simplest design was a two-section DFB laser which had a simple tuning mechanism [111]. Controlling the pump current through the tuning section can change the emission frequency as a result of shift in the effective index and the Bragg wavelength.

A new generation of tunable lasers, include the two [100], and three-section [112] DBR lasers which are typically constructed of a DBR section for frequency tuning, a gain section for amplification and in the case of the three-section DBR, a phase control part that provides smaller wavelength tuning steps and mode stability. Today, DBR lasers are widely used in several applications since they offer larger tuning range (> 40 nm), and narrow linewidth performance [113].

In addition to frequency tuning features, advanced DBR lasers have been widely studied for various applications such as optical communication systems. In recent studies, the optical injection locking technique has been combined with gain-lever modulation in multi-section DBR lasers to further improve the RF performance, including the modulation efficiency enhancement, bandwidth improvement and nonlinear distortion reduction. Using this technique, a 10-dB enhancement in the intensity modulation efficiency, a 3x improvement in the modulation bandwidth, and a 15-dB suppression of the third-order inter-modulation distortion has been reported in a multi-section QW DBR laser [114].

1.3   Organization of Dissertation

This work studies the manipulation of intrinsic characteristics of nanostructure QD and QDash lasers using external control techniques of optical injection-locking, optical feedback, and asymmetric bias configuration.

Chapter 2 studies the impact of optical injection-locking on the direct modulation characteristics of QD and QDash nanostructure lasers. This chapter recasts a predictive response model to investigate the modulation characteristics of QD and QDash lasers under stable injection-locking conditions. The presented response function accounts for the unique carrier dynamics in these lasers by implicitly incorporating the nonlinear gain compression through known free-running parameters. Using this model, the key operating parameters of injection-locked QDash and QD lasers were extracted directly from measured data in the microwave domain and the results are compared for each laser structure. Chapter 2 gives a detailed characterization of the slave QDash and QD devices

under investigation and highlights the key free-running parameters that make these types of active regions suitable for implementation in an injection-locked laser system. The validity of the response model then is examined based on the extracted value's correlation with theoretical predictions. It is also shown that comprehensive analysis of the extracted parameters can be further used in optimizing the overall modulation performance of the coupled system.

In chapter 3, the impact of optical injection-locking on the linewidth enhancement factor of a QDash slave laser is investigated. In this chapter, manipulation of the linewidth enhancement factor of an injection-locked QDash laser under zero detuning and strong optical injection is studied. The experimental findings are validated by comparing the extracted linewidth enhancement values from the measured microwave response to the directly measured results.

Chapter 4 describes methods of external control in the generation and stabilization of dual-mode emission in a single frequency QD laser diode. In this chapter, a dual-mode emission mechanism is realized for the first time by asymmetrically pumping a two-section QD DFB laser operating in the excited state mode. The detailed design and fabrication of the two-section QD DFB laser diode is presented. This chapter also demonstrates how combining the unique QD carrier dynamics along with excited state coupled mode operation allows for the manipulation of QD states through external optical feedback stabilization.

Lastly, chapter 5 gives a summary of the work and highlights proposed future research related to the impact of external control techniques on overall characteristics and performance of QD and QDash semiconductor lasers.

1.4 Chapter 1 References

[1]   R. N. Hall, G. E. Fenner, J. D. Kingsley, T. J. Soltys, and R. O. Carlson, "Coherent Light emission from GaAs junctions," *Physics Review Letters*, Vol. 9, No. (9), pp. 366-368, (1962).

[2]   Zh. I. Alferov, V. M. Andreev, E. L. Portnoi, M. K. Trukan, "AlAs-GaAs heterojunction injection lasers with a low room-temperature threshold," *Soviet Physics -Semiconductors,* Vol. 3, pp. 1107-1110, (1970).

[3]   Zh. I. Alferov, V. M. Andreev, D. Z. Garbuzov, Yu. V. Zhilyaev, E. P. Morozov, E. L. Portnoi, and V. G. Trofim, "Effect of heterostructure parameters on the laser threshold current and the realization of continuous generation at room temperature," *Soviet Physics -Semiconductors,* Vol. 4, pp. 1573-1575, (1970).

[4]   I. Hayashi, M. B. Panish, P. W. Foy and S. Sumski, "Junction lasers which operate continuously at room temperature," *Applied Physics Letters,* Vol. 17, No. (3), pp. 109-111, (1970).

[5]   R. D. Dupuis, and P. D. Dapkus, "Very low threshold $Ga_{1-x}Al_xAs$-GaAs double-heterostructure lasers grown by metalorganic chemical vapor deposition," *Applied Physics Letters,* Vol. 32, No. (8), pp. 473-475, (1978).

[6]   C. Gmachl, F. Capasso, D. L. Sivco, and A. Y. Cho, "Recent progress in quantum cascade lasers and applications," *Reports On Progress In Physics,* Vol. 64, No. (11), pp. 1533-1601, (2001).

[7]   Z. I. Alferov, V. M. Andreev, V. I. Korol'kov, E. L. Portnoi, and D.N. Tret'yakov, "Injection properties of n-Al Ga As-p-GaAs hetero-junctions," *Soviet Physics -Semiconductors,* Vol. 2, pp. 843-844, (1969).

[8]   I. Hayashi, M. B. Panish, P. W. Foy, and S. Sumski, "Junction lasers which operate continuously at room temperature," *Applied Physics Letters,* Vol. 17, No. (3), pp. 109-111, (1970).

[9]   R. D. Dupuis, P. D. Dapkus, N. Holonyak Jr., E. A. Rezek, R. Chin, "Room temperature operation of quantum-well Ga1-xAlxAs-GaAs laser diodes grown by metalorganic chemical vapor deposition," *Applied Physics Letters,* Vol. 32, No. (5), pp. 295-297, (1978).

[10]   W. T. Tsang, "Extremely low threshold (AlGa)As modified multi-quantum well heterostructure lasers grown by molecular-beam epitaxy," *Applied Physics Letters,* Vol. 39, No. (10), pp. 786-788, (1981).

[11]   W. T. Tsang, "Extremely low threshold (AlGa)As graded-index waveguide separate-confinement heterostructure lasers grown by molecular-beam epitaxy," *Applied Physics Letters,* Vol. 40, No. (3), pp. 217-219, (1982).

[12]   N. Chand, E. E. Becker, J. P. Van der Zeil, S. N. G. Chu, and N. K. Dutta, "Excellent uniformity and very low (less-than-50A/cm2) threshold current density strained InGaAs quantum-well diode-lasers on GaAs substrate," *Applied Physics Letters,* Vol. 58, No. (16), pp. 1704-1706, (1991).

[13]   J. L. Pan, "Intraband Auger processes and simple models of the ionization balance in semiconductor quantum-dot lasers," *Physical Review B-Condensed Matter,* Vol. 49, No.(16), pp. 11272-11287, (1994).

[14]   N. N. Ledentsov, V. M. Ustinov, A. Yu. Egorov, A. E. Zhukov, M. V. Maksimov, L. G. Tabatadze, and P. S. Kopev, "Optical properties of heterostructures with

InGaAs–GaAs quantum clusters," *Semiconductors,* Vol. 28, No. (8), pp. 832-834, (1994).

[15] N. Kirstaedter, N. N. Ledentsov, M. Grundmann, D. Bimberg, V. M. Ustinov, S. S. Ruvimov, M. V. Maximov, P. S. Kopev, Z. I. Alferov, U. Richter, P. Werner, U. Gosele, and J. Heydenreich, "Low threshold, large T_o injection laser emission from (InGa)As quantum dots," *Electronics Letters,* Vol. 30, No. (17), pp. 1416-1417, (1994).

[16] Y. Arakawa, and H. Sakaki, "Multidimensional quantum well laser and temperature dependence of its threshold current," *Applied Physics Letters,* Vol. 40 No. (11), pp. 939-941, (1982).

[17] M. Asada, Y. Miyamoto, Y. Suematsu, "Gain and The Threshold of 3-Dimensional Quantum-Box Lasers," *IEEE Journal of Quantum Electronics*, Vol. 22, No. (9), pp.1915-1921, (1986).

[18] G. T. Liu, A. Stintz, H. Li, K. J. Malloy, and L. F. Lester, "Extremely low room-temperature threshold current density diode lasers using InAs dots in In0.15Ga0.85As quantum well," *Electronics Letters,* Vol. (35), No. (14), pp. 1163-1165, (1999).

[19] O. B. Shchekin and D. G. Deppe, "1.3 μm InAs quantum dot laser with T_0 =161 K from 0 to 80 degrees C," *Applied Physics Letters,* Vol. 80, No. (18), pp. 3277-3279, (2002).

[20] T. C. Newell, D. Bossert, A. Stintz, B. Fuchs, K. J. Malloy, and L. F. Lester, "Gain And Linewidth Enhancement Factor In InAs Quantum Dot Laser Diodes," *IEEE Photonics Technology Letters,* Vol. 11, No. (12), pp. 1527-1529, (1999).

[21]   K. Y Lau and A. Yariv, "Ultrahigh speed semiconductor lasers," *IEEE Journal of Quantum Electronics*, Vol. 21, No. (2), pp. 121-138, (1985).

[22]   H. Su, L. F. Lester, "Dynamic properties of quantum dot distributed feed back lasers: high speed, linewidth and chirp," *Journal of Physics D: Applied Physics*, Vol. 38, No. (13), pp. 2112-2118, (2005).

[23]   F. Grillot, N. A. Naderi, M. Pochet, C.-Y. Lin, and L. F. Lester, "Variation of the feedback sensitivity in a 1.55-μm InAs/InP quantum dash Fabry-Perot semiconductor laser," *Applied Physics Letters,* Vol. 93, No. (19), pp. 191108, (2008).

[24]   M. Tani, O. Morikawa, S. Matsuura, and M. Hangyo, "Generation of terahertz radiation by photomixing with dual- and multiple-mode lasers," *Semiconductor Science and Technology*, Vol. 20, No. (7), pp. S151–S163, (2005).

[25]   A. Pikovsky, M. Rosenblum, and J. Kurths, *Synchronization: A Universal Concept in Nonlinear Science*: Cambridge University Press, (2001).

[26]   R. Lang, "Injection locking properties of a semiconductor laser," *IEEE Journal of Quantum Electronics*, Vol. 18, No. (6), pp. 976-83, (1982).

[27]   S. Kobayashi and T. Kimura, "Coherence on injection phase-locked AlGaAs semiconductor laser," *Electronics Letters*, Vol. 16, No. (17), pp. 668-670, (1980).

[28]   F. Mogensen, H. Olesen, and G. Jacobsen, "Locking conditions and stability properties for a semiconductor laser with external light injection," *IEEE Journal of Quantum Electronics*, Vol. 21, No. (7), pp. 784-93, (1985).

[29] O. Lidoyne, P. Gallion, C. Chabran, and G. Debarge, "Locking range, phase noise and power spectrum of an injection- locked semiconductor laser," *in Proceedings of IEE Journal of Optoelectronics*, Vol. 137, No. (3), pp. 147-154, (1990).

[30] I. Petitbon, P. Gallion, G. Debarge, and C. Chabran, "Locking bandwidth and relaxation oscillations of an injection- locked semiconductor laser," *IEEE Journal of Quantum Electronics*, Vol. 24, No. (2), pp. 148-154, (1988).

[31] T. Erneux, V. Kovanis, A. Gavrielides, and P. M. Alsing, "Mechanism for period-doubling bifurcation in a semiconductor laser subject to optical injection," *Physical Rev. A*, Vol. 53, No. (6), pp. 4372-4380, (1996).

[32] M. Pochet, N. A. Naderi, N. Terry, V. Kovanis, and L. F. Lester, "Dynamic behavior of an injection-locked quantum-dash Fabry-Perot laser at zero-detuning," *Optics Express*, Vol. 17, No. (23), pp. 20623-20630, (2009).

[33] P. Gallion, H. Nakajima, G. Debarge, and C. Chabran, "Contribution of spontaneous emission to the linewidth of an injection-locked semiconductor laser," *Electronics Letters*, Vol. 21, No. (14), pp. 626-628, (1985).

[34] K. Iwashita and K. Nakagawa, "Suppression of mode partition noise by laser diode light injection," *IEEE Journal of Quantum Electronics*, Vol. 18, No. (10), pp. 1669-1674, (1982).

[35] N. A. Olsson, H. Temkin, R. A. Logan, L. F. Johnson, G. J. Dolan, J. P. van der Ziel, and J. C. Campbell, "Chirp- free transmission over 82.5 km of single mode fibers at 2 Gbit/s with injection locked DFB semiconductor lasers," *Journal of Lightwave Technology*, Vol. 3, No. (1), pp. 63-67, (1985).

[36] Y. Yamamoto and T. Kimura, "Coherent optical fiber transmission systems," *IEEE Journal of Quantum Electronics*, Vol. 17, No. (6), pp. 919-935, (1981).

[37] S. Piazzolla, P. Spano, and M. Tamburrini, "Small signal analysis of frequency chirping in injection- locked semiconductor lasers," *IEEE Journal of Quantum Electronics*, Vol. 22, No. (12), pp. 2219-2223, (1986).

[38] S. Mohrdiek, H. Burkhard, and H. Walter, "Chirp reduction of directly modulated semiconductor lasers at 10 Gb/s by strong CW light injection," *Journal of Lightwave Technology*, Vol. 12, No. (3), pp. 418-424, (1994).

[39] X. J. Meng, T. Chau, and M. C. Wu, "Experimental demonstration of modulation bandwidth enhancement in distributed feedback lasers with external light injection," *Electronics Letters*, Vol. 34, No. (21), pp. 2031-2032, (1998).

[40] X. J. Meng, C. Tai, and M. C. Wu, "Improved intrinsic dynamic distortions in directly modulated semiconductor lasers by optical injection locking," *IEEE Transactions on Microwave Theory & Techniques*, Vol. 47, No. (7), pp. 1172-1176, (1999).

[41] L. Chrostowski, C. H. Chang, and C. Chang-Hasnain, "Reduction of relative intensity noise and improvement of spur-free dynamic range of an injection locked VCSEL," *in Proceedings of IEEE Lasers and Electro-Optics Society Meeting*, Vol. 2, pp.706-707, (2003).

[42] M. C. Espana-Boquera and A. Puerta-Notario, "Noise effects in injection locked laser simulation: phase jumps and associated spectral components," *Electronics Letters*, Vol. 32, No. (9), pp. 818-19, (1996).

[43]   J. M. Liu, H. F. Chen, X. J. Meng, and T. B. Simpson, "Modulation bandwidth, noise, and stability of a semiconductor laser subject to strong injection locking," *IEEE Photonics Technology Letters*, Vol. 9, No. (10), pp. 1325-1327, (1997).

[44]   G. Yabre, H. De Waardt, H. P. A. van den Boom, and G. D. Khoe, "Noise characteristics of single-mode semiconductor lasers under external light injection," *IEEE Journal of Quantum Electronics*, Vol. 36, No. (3), pp. 385-393, (2000).

[45]   X. Jin and S. L. Chuang, "Relative intensity noise characteristics of injection-locked semiconductor lasers," *Applied Physics Letters*, Vol. 77, No. (9), pp. 1250-2, (2000).

[46]   K. Schunk, G. Grosskopf, L. Kuller, and K. Petermann, "Noise characteristics of injection locked semiconductor lasers," *in proceedings of International Conference on Integrated Optics and Optical Fiber Communication*, Vol. 1, pp. 717-720, (1985).

[47]   R. Olshansky, P. Hill, V. Lanzisera, W. Powazinik, "Frequency response of 1.3μm InGaAsP high speed semiconductor laser," *IEEE Journal of Quantum Electronics*, Vol. 23, No. (9), pp. 1410-1418, (1987).

[48]   H. K. Sung, T. Jung, M. C. Wu, D. Tishinin, T. Tanbun-Ek, K. Y. Liou, and W. T. Tsang, "Modulation bandwidth enhancement and nonlinear distortion suppression in directly modulated monolithic injection-locked DFB lasers," *in proceedings of International Topical Meeting on Microwave Photonics*, pp. 27-30, (2003).

[49] L. Chrostowski, X. Zhao, C. J. Chang-Hasnain, R. Shau, M. Ortsiefer, and M. Amann, "50 GHz directly-modulated injection-locked 1.55 μm VCSELs," *in proceedings of Optical Fiber Communication Conference*, Vol. 4, (2005).

[50] E. K. Lau, H.-K. Sung, and M. C. Wu, "Ultra-high, 72 GHz resonance frequency and 44 GHz bandwidth of injection-locked 1.55-μm DFB lasers," *in Proceedings of Optical Fiber Communication Conference*, (2006).

[51] H. L. T. Lee, R. J. Ram, O. Kjebon, and R. Schatz, "Bandwidth enhancement and chirp reduction in DBR lasers by strong optical injection," *in Proceedings of Conference on Lasers and Electro-Optics*, Vol. 39, pp. 99-100, (2000).

[52] S. K. Hwang, J. M. Liu, and J. K. White, "35-GHz intrinsic bandwidth for direct modulation in 1.3μm semiconductor lasers subject to strong injection-locking semiconductor lasers," *IEEE Photonics Technology Letters*, Vol. 16, No. (4), pp. 972-974, (2003).

[53] E. K. Lau, X. Zhao, H. K. Sung, D. Parekh, C. Chang-Hasnain, M. C. Wu, "Strong optical injection-locked semiconductor lasers demonstrating >100-GHz resonance frequencies and 80-GHz intrinsic bandwidths," *Optics Express*, Vol. 16, No. (9), pp. 6609-6618, (2008).

[54] M. Al-Mumin, X. H. Wang, W. M. Mao, S. A. Pappert, and G. F. Li, "Optical generation and sideband injection locking of tunable 11-120GHz microwave/millimeter signals," *Electronics Letters*; Vol. 36, No. (18), pp. 1547-1548, (2000).

[55] Y. Onishi, and F. Koyama, "All-optical regeneration using a vertical-cavity surface-emitting laser with external light injection," *IEICA Transactions on Electronics*, Vol. E87C, No. (3), pp. 409-415, (2004).

[56] A. Kaszubowska, P. Anandarajah, and L. P. Barry, "Improved performance of a hybrid radio/fiber system using directly modulated laser transmitter with external injection," *IEEE Photonics Technology Letters*, vol. 14, No. (2), pp 233-235, (2002).

[57] H. Lu, H. Huang, H. Su, and M. Wang, "Fiber optical CATV system-performance improvement by using external light-injection technique," *Photonics Technology Letters, IEEE*, Vol. 15, No. (7), pp. 1017-1019, (2003).

[58] L. Goldberg, H. F. Taylor, J. F. Weller, and D. M. Bloom, "Microwave signal generation with injection-locked laser diodes," *Electronics Letters*, Vol. 19, No. (13), pp. 491-493, (1983).

[59] L. Goldberg, A. M. Yurek, H. F. Taylor, and J. F. Weller, "35 GHz microwave signal generation with an injection-locked laser diode," *Electronics Letters*, Vol. 21, No. (18), pp. 814-815, (1985).

[60] R. P. Braun, G. Grosskopf, R. Meschenmoser, D. Rohde, F. Schmidt, and G. Villino, "Microwave generation for bidirectional broadband mobile communications using optical sideband injection locking," *Electronics Letters*, Vol. 33, No. (16), pp. 1395-1396, (1997).

[61] R. P. Braun, G. Grosskopf, D. Rohde, and F. Schmidt, "Low-phase-noise millimeter-wave generation at 64 GHz and data transmission using optical

sideband injection locking," *IEEE Photonics Technology Letters*, Vol. 10, No. (5), pp. 728-730, (1998).

[62]   L. Noel, D. Marcenac, and D. Wake, "Optical millimeter-wave generation technique with high efficiency, purity and stability," *Electronics Letters*, Vol. 32, No. (21), pp. 1997-1998, (1996).

[63]   H. Jin, and H. Rongqing, "Tunable millimeter-wave generation with subharmonic injection locking in two-section strongly gain-coupled DFB lasers," *IEEE Photonics Technology Letters*, Vol. 12, No. (5), pp. 543-545, (2000).

[64]   A. Kuramoto and S. Yamashita, "All-optical regeneration using a side-mode injection-locked semiconductor laser," *IEEE Journal of Selected Topics in Quantum Electronics*, Vol. 9, No. (5), pp. 1283-1287, (2003).

[65]   S. Yamashita and J. Suzuki, "All-optical 2R regeneration using a two-mode injection-locked Fabry-Perot laser diode," *IEEE Photonics Technology Letters*, Vol. 16, No. (4), pp. 1176-1178, (2004).

[66]   R. F. Broom, E. Mohn, C. Risch, and R. Salathe, "Microwave self-modulation of a diode laser coupled to an external cavity," *IEEE Journal of Quantum Electronics,* Vol. 6, No. (6), pp. 328-334, (1970).

[67]   N. Chinone, K. Aiki, and R. Ito, "Stabilization of semiconductor laser outputs by a mirror close to a laser facet," *Applies Physics Letters*, Vol. 33, No. (12), pp. 990-992, (1978).

[68]   R. Lang, and K. Kobayashi, "External optical feedback effects on semiconductor injection laser properties," *IEEE Journal of Quantum Electronics,* Vol. 16, No. (3), pp. 347-355, (1980).

[69] R. O. Miles, A. Dandridge, A. B. Tveten, H. F. Taylor, and T. G. Giallorenzi, "Feedback-induced line broadening in cw channel-substrate planar laser diodes," *Applies Physics Letters*, Vol. 37, No. (11), pp. 990-992, (1980).

[70] K. Kikuchi and T. Okoshi, "Simple formula giving spectrum-narrowing ratio of semiconductor laser output obtained by optical feedback," *Electronics Letters*, Vol. 18, No. (1), pp. 10-12, (1982).

[71] Y. Cho, and M. Umeda, "Chaos in laser oscillations with delayed feedback; numerical analysis and observation using semiconductor laser," *Journal of Optical Society of America B.*, Vol. 1, pp. 497-498, (1984).

[72] L. Goldberg, H. F. Taylor, A. Dandridge, I. F. Weller, and R. O. Miles, "Spectral characteristics of semiconductor lasers with optical feedback," *IEEE Journal of Quantum Electronics*, Vol. 18, No. (4), pp. 555-564, (1982).

[73] J. Mørk, B. Tromborg, and P. L. Christiansen, "Bistability and low-frequency fluctuations in semiconductor lasers with optical feedback," *IEEE Journal of Quantum Electronics*, Vol. 24, No. (2), pp. 123-133, (1988).

[74] N. Schunk and K. Petermann, "Numerical analysis of the feedback regimes for a single-mode semiconductor laser with external feedback," *IEEE Journal of Quantum Electronics*, Vol. 24, No. (7), pp. 1242–1247 (1988).

[75] Z. Xing-Sha and Y. Peida, "Intensity noise of semiconductor lasers in the presence of arbitrary optical feedback," *Electronics Letters*, Vol. 25, No. (7), pp. 445–446 (1989).

[76]   B. Tromborg, J. H. Osmundsen and H. Olesen, "Stability analysis for a semiconductor laser in an external cavity," *IEEE Journal of Quantum Electronics*, Vol. 20, No. (9), pp. 1023–1032 (1984).

[77]   C. H. Henry and R.F. Kazarinov, "Instability of semiconductor lasers due to optical feedback from distant reflectors," *IEEE Journal of Quantum Electronics*, Vol. 22, No. (2), pp. 294–301 (1986).

[78]   F. Favre, D. Le Guen, and J. C. Simon, "Optical feedback effects upon laser diode oscillation field spectrum," *IEEE Journal of Quantum Electronics*, Vol. 18, No. (10), pp. 1712-1717, (1982).

[79]   R. Tkach and A. Chraplyvy, "Regimes of feedback effects in 1.5 _m distributed feedback lasers," *IEEE Journal of Lightwave Technology*, Vol. 4, No. (11), pp. 1655–1661, (1986).

[80]   D. Lenstra, B. H. Verbeek, and A. J. den Boef, "Coherence collapse in single mode semiconductor lasers due to optical feedback," *IEEE Journal of Quantum Electronics*, Vol. 21, No. (6), pp. 674–679, (1985).

[81]   G. P. Agrawal, "Line narrowing in a single-mode injection laser due to external optical feedback," *IEEE Journal of Quantum Electronics*, Vol. 20, No. (5), pp. 468–471, (1984).

[82]   K. Kobayashi, "Improvements in direct pulse code modulation of semiconductor lasers by optical feedback," *IEICE Transactions*, Vol. 59, No. (12), pp. 8–14 (1976).

[83] M. Yousefi, D. Lenstra, G. Vemuri, and A. Fischer, "Control of nonlinear dynamics of a semiconductor laser with filtered optical feedback," *in Proceedings of IEE Semiconductor Optoelectronics*, Vol. 148, No. (5), (2001).

[84] Y. Liu, H. F. Chen, J. M. Liu, P. Davis, and T. Aida, "Communication using synchronization of optical-feedback-induced chaos in semiconductor lasers," *IEEE Transactions on Circuits and Systems - Fundamental Theory and Applications*, Vol. 48, No. (12), pp. 1484-1490, (2001).

[85] A. P. Fischer, O. K. Andersen, M. Yousefi, and D. Lenstra, "experimental and theoretical study of filtered optical feedback in a semiconductor laser," *IEEE Journal of Quantum Electronics*, Vol. 36, No. (3), pp. 375-384, (2000).

[86] H. Erzgraber, D. Lenstra, and B. Krauskopf, "Pure frequency oscillations of semiconductor lasers with filtered optical feedback," *in Proceedings of IEEE Lasers and Electro-Optics Society Meeting*, pp. 47-50, (2005).

[87] K. Merghem, R. Rosales, S. Azouigui, A. Akrout, A. Martinez, F. Lelarge, G.-H. Duan, G. Aubin, and A. Ramdane, "Low noise performance of passively mode locked quantum-dash-based lasers under external optical feedback," *Applied Physics Letters*, Vol. 95, No. (13), pp. 131111 (2009).

[88] C. Y. Lin, F. Grillot, N. A. Naderi, Y. Li, and L. F. Lester, "rf linewidth reduction in a quantum dot passively mode-locked laser subject to external optical feedback," *Applied Physics Letters*, Vol. 96, No. (5), pp. 051118(1)-051118(3), (2010).

[89] M. Radziunas, A. Glitzky, U. Bandelow, M. Wolfrum, U. Troppenz, J. Kreissl, and W. Rehbein, "Improving the modulation bandwidth in semiconductor lasers

by passive feedback," *IEEE Journal of Selected Topics in Quantum Electronics*, Vol. 13, No. (1), pp. 136–142, (2007).

[90]   I. Fischer, Y. Liu, and P. Davis, "Synchronization of chaotic semiconductor laser dynamics on sub-nanosecond time scales and its potential for chaos communication," *Physics Review A.*, Vol. 62, No. (1), pp. 011801-011805, (2000).

[91]   N. Matsumoto, "The bent-guide structure AlGaAs-GaAs semiconductor laser," *IEEE Journal of Quantum Electronics*, Vol. 13, No. (8), pp. 560-564, (1977).

[92]   P. G. Eliseev, I. Ismailov, M. A. Manko, and **V.** P. Strakhov, "Injection semiconductor laser with compound resonator," *JETP Letters*, Vol. 9, No. (10), pp. 362-363, (1969).

[93]   L. A. Coldren, K. J. Ebeling, B. I. Miller, and J. A. Rentschler, "Single longitudinal mode operation of two-section GaInAsP/InP lasers under pulsed excitation," *IEEE Journal of Quantum Electronics*, Vol. 19, No. (6), pp. 1057-1062, (1983).

[94]   A. Antreasyan, and S. Wang, "Electronic wavelength tuning with semiconductor integrated etalon interference lasers," *Applied Physics Letters*, Vol. 43, No. (6), pp. 530-532, (1983).

[95]   L. A. Coldren, B. I. Miller, K. Iga, and J. A. Rentschler, "Monolithic two-section GaInAsP/InP active-optical resonator devices formed by reactive ion etching," *Applied Physics Letters*, Vol. 38, No. (5), pp. 315-317, (1981).

[96]   T. L. Koch and L. A. Coldren, "Optimum coupling junction and cavity lengths for coupled-cavity semiconductor lasers," *Journal of Applied Physics*, Vol. 57, No. (3), pp. 740-754, (1985).

[97]   H. K. Choi, K. L. Chen, and S. Wang, "Analysis of two-section coupled-cavity semiconductor lasers," *IEEE Journal of Quantum Electronics*, Vol. 20, No. (4), pp. 385-393, (1984).

[98]   W. T. Tsang, N. A. Olsson, and R. A. Logan, "High-speed direct single frequency modulation with large tuning rate and frequency excursion in cleaved-coupled-cavity semiconductor lasers," *Applied Physics Letters*, Vol. 42, No. (8), pp. 650-652, (1983).

[99]   M. Kitamura, M. Yamaguchi, K. Emura, I. Mito, and K. Kobayashi, "Lasing mode and spectral linewidth control by phase tunable distributed feedback laser diodes with double channel planar buried heterostructure," *IEEE Journal of Quantum Electronics*, Vol. 21, No. (5), pp. 415-417, (1985).

[100] T. L. Koch, U. Koren, and B. I. Miller, "High performance tunable 1.5μm InGaAs/InGaAsP multiple quantum well distributed feedback Bragg reflector lasers," *Applied Physics Letters*, Vol. 53, No. (12), 1036–1038, (1988).

[101] X. Huang, A. Stintz, H. Li, L. F. Lester, J. Cheng, and K. J. Malloy, "Passive mode-locking in 1.3μm two-section InAs quantum dot lasers," *Applied Physics Letters*, Vol. 78, No. (19), pp. 2825-2827, (2001).

[102] K. J. Vahala, M. A. Newkirik, and T. R. Chen, "The optical gain-lever: a novel gain mechanism in the direct modulation of QW semiconductor lasers," *Applied Physics Letters*, Vol. 54, No. (25), pp. 2506-2508, (1989).

[103] M. A. Newkirk, K. J. Vahala, "Equivalent circuit model for active-layer photo-mixing: parasitic-free modulation of semiconductor lasers," *Applied Physics Letters*, Vol. 53, No. (13), pp. 1141-1143, (1988).

[104] N. Moore and K. Y. Lau, "Ultrahigh efficiency microwave signal transmission using tandem-contact single QW GaAlAs lasers," *Applied Physics Letters*, Vol. 55, No. (10), pp. 936-938, (1989).

[105] K. Y. Lau, "The 'inverted' gain-levered semiconductor laser-direct modulation with enhanced frequency modulation and suppressed intensity modulation," *IEEE Photonics Technology Letters*, Vol. 3, No. (8), pp. 703-705, (1991).

[106] N. A. Naderi, Y. Li, C. Dziak, Y-C. Xin, V. Kovanis and L. F. Lester, "Quantum dot gain-lever laser diode," *in Proceedings of IEEE Lasers and Electro-Optics Society Meeting*, pp. 52-53, (2006).

[107] Y. Li, N. A. Naderi, Y.-C. Xin, C. Dziak, and L. F. Lester, "Multi-section gain-lever quantum dot lasers," *in Proceedings of SPIE Photonics West Conference,* Vol. 6468, pp. 646819-646826 (2007).

[108] Y. Li, N. A. Naderi, V. Kovanis, L. F. Lester, "Enhancing the 3-dB Bandwidth via the Gain-Lever Effect in Quantum-Dot Lasers," *IEEE Photonics Journal*, Vol. 2, No. (3), pp. 321-329, (2010).

[109] B. Broberg and S. Nilsson, "Widely tunable active Bragg reflector integrated lasers in InGaAsP-InP," *Applied Physics Letters*, Vol. 52, No. (16), pp. 1285-1288, (1988).

[110] M. Kuznetsov, "Theory of wavelength tuning in two-segment distributed feedback lasers," *IEEE Journal of Quantum Electronics*, Vol. 24, No. (9), pp. 1837-1844, (1988).

[111] N. K. Dutta, A. B. Piccirilli, T. Cella, and R. L. Brown, "Electronically tunable distributed feedback lasers," *Applied Physics Letters*, Vol. 48, No. (22), pp. 1501-1503, (1986).

[112] T. Numai, S. Murata, I. Mito, "1.5μm wavelength tunable phase-shift controlled distributed feedback laser diode with constant spectral linewidth in tuning operation," *Electronics Letters*, Vol. 24, No. (24), pp. 1526-1528, (1988).

[113] V. Jayaraman, D. A. Cohen, and L. A. Coldren, "Demonstration of broadband tunability in a semiconductor laser using sampled gratings," *Applied Physics Letters*, Vol. 60, No. (19), pp. 2321–2323, (1992).

[114] H. K. Sung, T. Jung, D. Tishinin, K. Y. Liou, W. T. Tsang, and M. C. Wu, "Optical injection-locked gain-lever distributed Bragg reflector lasers with enhanced RF performance," *in Proceedings of IEEE International Topical Meeting on Microwave Photonics,* pp. 225-228, (2004).

Chapter 2

Modeling the Injection-Locked Characteristics of Nanostructure Semiconductor Lasers

2.1 Introduction

As introduced in Chapter 1, injection-locking of semiconductor lasers is one of the most attractive research topics since this method induces superior improvement in the high-speed characteristics of directly modulated lasers such as increasing the modulation bandwidth, suppressing non-linear distortion, decreasing relative intensity noise, mode hopping and reducing chirp [1]-[7]. Previous studies have mostly investigated the impact of the injection-locking technique on the modulation properties of bulk and QW lasers, but very little is known about the impact of optical injection on the novel nanostructure lasers such as QD and QDash devices. As discussed in the previous chapter, compared to bulk and QW devices, 3-D confinement nanostructure lasers were expected to exhibit much better modulation performance under optical injection as a result of their unique carrier dynamics and superior intrinsic characteristics.

Most notably, previous works have focused on realizing high modulation bandwidths and associated design strategies, analyzed the modulation properties of the coupled system in the spectral domain, and numerically investigated the modulation response of the injection-locked system [4]-[11].

Noting the benefits of extracting relevant operating parameters from measured data in order to aid in future simulations, this chapter focuses on extracting the operating parameters from an injection-locking system by introducing a novel modulation response function and experimentally verifying the validity of the resultant model in the microwave domain using two types of nanostructure semiconductor lasers, QD and QDash Fabry-Perot (FP) devices as the slave laser. The extracted parameters of the coupled injection-locked system include the injection strength, linewidth enhancement factor, threshold gain shift, coupled phase offset between the master and slave laser, and the field enhancement factor which characterizes the deviation of the locked slave laser from its free running value. This chapter describes how the derived model incorporates nonlinear gain through the free-running damping rate and relaxation oscillation frequency, specifically nonlinear gain compression which arises from using nanostructure laser systems. The validity of the model and accuracy of the extracted terms are examined based on theoretically expected values for the fitting parameters at extreme detuning ranges. Also the derived model is used to perform theoretical simulations to analyze the impact of the linewidth enhancement factor on the characteristics of the modulation response function. This work shows when modeling injection-locked nanostructure lasers, the slave's linewidth enhancement factor plays an important role in the modulation response of the coupled system. The impact of the QDash slave laser bias current and temperature variations on the free-running relaxation oscillation frequency, damping rate, and linewidth enhancement factor, and the resultant effects on the observed pre-resonance dip in the modulation response of the coupled system is investigated. Furthermore, the modulation response of a QD FP laser under strong optical injection is

fully characterized. It is found that at particular injection strengths and detuning cases, a unique modulation response is observed that differs from the typical modulation response observed in injection-locked systems. The benefit of the observed response is that it takes advantage of the resonance frequency enhancement achieved through injection-locking without experiencing the low frequency dip that significantly limits the useful bandwidth in the conventional injection-locked response case. The second benefit of this unique response is that there is an improvement in the high frequency roll-off that extends the bandwidth.

2.2   Injection-Locking Theoretical Model

In order to characterize the high-speed modulation performance of an injection-locked laser system it is important to investigate the governing theory that can be obtained by modeling the characteristic parameters using a set of coupled rate equations [12]-[14]. Mathematical translation of the injection-locking system operating in the stable locking regime based on three fundamental rate equations was first demonstrated by Lang [12]. This section capitalizes on improvements to the rate equations governing the dynamic properties of an injection-locked system in order to investigate the modulation properties of such a system under strong optical injection [8]-[10].

2.2.1   Rate Equations

The differential equations describing the dynamics of an injection-locked system have been developed by introducing terms describing optical injection into the

conventional rate equations governing the free-running characteristics of the slave laser. The additional terms include a coupling value, k_c, the magnitude of the injected master field, A_{inj}, and the detuning frequency between master and slave, $\Delta\omega_{inj}$. The model assumes the slave laser is being directly modulated such that the small-signal approximation can be applied. Additionally, it is assumed that the laser has been exposed to a relatively strong external optical injection, such that the impact of the noise and the spontaneous emission rate coupled to the lasing mode are negligible [10]. The free-running slave laser is biased well above threshold. The injection-locking amplitude and phase rate equations arise from the fundamental complex field rate equation [8], [10]:

$$\frac{d\tilde{E}}{dt} = g\Delta N(1+j\alpha)\frac{\tilde{E}}{2} - j\Delta\omega_{inj}\tilde{E} + k_c A_{inj} \qquad (2.1)$$

where $\tilde{E}$ is the time-varying slave complex field, g is the differential gain, N is the carrier density and $\Delta N = N - N_{th}$ is the shift in carrier density from threshold, and α is the slave laser's linewidth enhancement factor. The complex electric field amplitude and phase in (2.1) can be separated as $\tilde{E} = A\exp(j\phi)$, where A is the amplitude of the slave's internal electric field, and ϕ is the phase offset between master and slave laser, which is defined as ϕ_{slave}-ϕ_{master}. The variation of the slave field magnitude, phase offset between the master and slave fields and carrier density with time can be written as [8], [10]:

$$\frac{dA}{dt} = \left(\frac{g}{2}\Delta N\right)A + (k_c\cos\phi)A_{inj} \qquad (2.2)$$

$$\frac{d\phi}{dt} = \alpha\left(\frac{g}{2}\Delta N\right) - \Delta\omega_{inj} - (k_c\sin\phi)\frac{A_{inj}}{A} \qquad (2.3)$$

$$\frac{dN}{dt} = J_{bias} - \gamma_N N - (\gamma_P + g\Delta N)A^2 \qquad (2.4)$$

45

where the amplitude of the electric field square, A^2, is proportional to the photon density, N_{ph}, and J_{bias}, γ_N and γ_P correspond to the applied bias current density, inverse differential carrier lifetime and cavity photon decay rates, respectively. It is important to note that the phase variation in time depends on detuning through $\Delta\omega_{inj}=\omega_{master}-\omega_{slaver}$. The linewidth enhancement factor, α, the injection strength which is proportional to A_{inj}/A, the phase offset ϕ, and the detuning term $\Delta\omega_{inj}$ are the key injection parameters that have a significant impact on the coupled oscillator system.

2.2.2 Steady-State Solutions

The equations described in (2.2) to (2.4) define the temporal and dynamic behavior of the system. The injection-locking phenomenon is investigated through the steady-state solutions arising from these three differential equations. Under steady-state, the right hand side of (2.2) to (2.4) is equal to zero as there will be no time variation in the slave's field amplitude, phase and carrier density. Using an approach presented by Murakami [8], the steady-state parameters of the injection-locked system can be defined as the steady-state phase offset, ϕ_0, steady-state carrier density, N_0, steady-state locked slave field, A_0, and the free-running slave field, A_{fr} [10]. Based on this strategy the first general condition for the system under injection-locking can be clearly found through (2.3) by introducing the steady-state parameters and setting the left hand side equal to zero:

$$\Delta\omega_{inj} = \frac{\alpha}{2}\left(g\Delta N_0\right) - \left(k_c\sin\phi_0\right)\frac{A_{inj}}{A_0} \qquad (2.5)$$

46

where the change in carrier density under the steady-state condition is expressed as $\Delta N_0 = N_0 - N_{th}$. Equation (2.5) describes the correlation between frequency detuning, threshold condition and the strength of the injected field. It can be clearly seen that depending on the detuning condition and the phase offset, the injected field can result in a threshold gain shift through $g\Delta N_0$. Note that the group velocity is implicit in the differential gain term, g.

Using this method and solving for the steady-state parameters of the coupled system, the relationship between the free-running and locked fields, an expression for the steady-state phase offset, and the change in the steady-state carrier density can be expressed as [8], [10]:

$$A_0^{\,2} = \left(A_{fr}^2 - \frac{\gamma_N}{\gamma_P} \Delta N_0 \right) \Big/ \left(1 + \frac{g\Delta N_0}{\gamma_P} \right) \qquad (2.6)$$

$$\phi_0 = \sin^{-1}\left\{ -\frac{\Delta\omega_{inj}}{k_c \sqrt{1+\alpha^2}} \frac{A_0}{A_{inj}} \right\} - \tan^{-1}\alpha \qquad (2.7)$$

$$\Delta N_0 = \frac{2}{g}\left(k_c \cos\phi_0 \right)\frac{A_{inj}}{A_0} \qquad (2.8)$$

The steady-state slave field and the phase offset between the slave and master laser and its boundary can be further used to find an expression for detuning, $\Delta\omega_{inj}$. However, computing the detuning value for a specific case is not possible unless the key parameters such as phase offset, linewidth enhancement factor, and injection strength can be extracted for that case. Rearranging (2.7) to solve for the detuning term, $\Delta\omega_{inj}$ becomes:

$$\Delta\omega_{inj} = -k_c \sqrt{1+\alpha^2}\, \frac{A_0}{A_{inj}} \sin^{-1}(\phi_0 + \tan^{-1}\alpha) \qquad (2.9)$$

47

The steady-state phase offset equation and the expression for the change in the carrier density can be used to indentify the injection locking stability condition that determines the locking boundaries which was first introduced by Mogensen *et al.* [13]. The initial constraint on the system can be found from equation (2.7). To find a real solution for the phase, the $\sin^{-1}$ term has to be less than or equal to 1, leading to the following expression:

$$-\tan^{-1}(\alpha) - \frac{\pi}{2} \leq \phi_0 \leq -\tan^{-1}(\alpha) + \frac{\pi}{2} = \cot^{-1}(\alpha) \qquad (2.10)$$

This constraint, which is known as the "locking half-width" [13], leads to the injection locking method of measuring the linewidth enhancement factor of the free running slave laser, which is later discussed in this chapter.

An additional constraint is found in equation (2.8). For stability, the carrier number, N, cannot exceed the threshold value, N_{th}. In simpler terms, the change in the steady-state carrier density must be less than zero, $\Delta N_0 < 0$. Applying this limitation to (2.8) and rearranging (2.10) yields the following expression for the phase constraint:

$$-\frac{\pi}{2} \leq \phi_0 \leq \cot^{-1}(\alpha) \qquad (2.11)$$

Equation (2.11) indicates that the phase is bounded across the locking range from $\cot^{-1}(\alpha)$ to $-\pi/2$, from the negative to positive frequency detuning edges, respectively. Using the phase constraint in (2.9) and rearranging (2.11), yields the important expression for the coupled system locking boundary condition [13]:

$$-k_c \sqrt{1 + \alpha^2}\, \frac{A_{inj}}{A_0} \leq \Delta\omega_{inj} \leq k_c \frac{A_{inj}}{A_0} \qquad (2.12)$$

Knowing the stable locking phase/detuning frequency constraints described above can further assist in modeling the modulation response of the coupled system at a given frequency detuning by reducing the range of the fitting parameters.

2.2.3 Small-Signal Analysis (Dynamic Solutions)

A detailed approach to find the small-signal solution of the rate equations expressed in (2.2) through (2.4) has been demonstrated in the literature [8], [10]. Based on this method the absolute modulation frequency response function can be expressed as:

$$|H(\omega)|^2 = \left|\frac{\Delta A}{\Delta J}\right|^2 = \frac{|M|^2(\omega^2 + Z^2)}{(C - A\omega^2)^2 + (B\omega - \omega^3)^2} \qquad (2.13)$$

where the parametric terms A, B, C, Z and M can be defined and simplified as [10]:

$$A = 2\eta\cos\phi_0 + \gamma_N + gA_0^2 \qquad (2.14)$$

$$B = \eta^2 + 2\eta\cos\phi_0\left(gA_0^2 + \gamma_N\right) + gA_0^2\left(\gamma_P - 2\eta\cos\phi_0\right) \qquad (2.15)$$

$$C = \eta^2\left(\gamma_N + gA_0^2\right) - gA_0^2\left(\gamma_P - 2\eta\cos\phi_0\right)Z \qquad (2.16)$$

$$Z = \eta\left(\alpha\sin\phi_0 - \cos\phi_0\right) \qquad (2.17)$$

$$M = \frac{g}{2}A_0 \qquad (2.18)$$

The injection strength is proportional to the coupling term and the field ratio as:

$$\eta = k_c\frac{A_{inj}}{A_0} = \eta_0/R_{FE} \qquad (2.19)$$

where η_0 is the maximum injection ratio and $R_{FE} = A_0/A_{fr}$ is the slave field enhancement factor due to injection. η_0 incorporates the external master to slave power ratio, the coupling efficiency between the slave and master laser, and the efficiency of the injected field entering the slave laser cavity due to the facet reflectivity. At this point, the enhancement of the slave field is introduced as an additional term denoted as the field enhancement factor, R_{FE}, which takes into account the deviation of the slave steady-state field magnitude compared to its free-running value at a high injection ratio and a specific frequency detuning.

2.2.4 Modulation Response Function

The modulation response model expressed in (2.13) through (2.18) can be used to simulate the modulation characteristics of an injection-locking system in the microwave domain. There are as many as 8 fitting parameters involved in this model, and this large number of potentially unconstrained parameters allows for many possible solutions that will reduce confidence in extracted results. One of the goals of this work is to reduce the number of fitting parameters through known free-running slave terms along with additional constraints on remaining injection-locking fitting terms. By doing so, the parametric terms *A*, *B*, *C*, and *Z* defined in (2.14) through (2.18) can be translated in terms of known free-running and injection-locked parameters. This reduces the number of fitting parameters and expresses the remaining parameters in terms of the injection-locking operating parameters which then will be projected in the targeted relative modulation response function. Since the $|M|^2$ term defined in (2.13) and (2.18) is

independent of frequency, it can be cancelled in the relative modulation response form. The "*A*" term in (2.14), is effectively a damping rate of the coupled oscillator as follows:

$$A = \gamma_{slave} + \gamma_{th} \tag{2.20}$$

The slave damping rate, γ_{slave}, is related to the free-running damping rate and scales with the field enhancement factor as:

$$\gamma_{slave} = gA_0^2 + \gamma_N = (\gamma_{fr} - \gamma_N)R_{FE}^2 + \gamma_N \tag{2.21}$$

where $\gamma_{fr} = gA_{fr}^2 + \gamma_N$ is the free-running slave damping rate and γ_N is assumed to be independent of optical injection. The explicit relationship between the locked and free-running damping rates is a key feature of the current model and allows us to implicitly include non-linear gain effects as explained below. γ_{th} is the threshold gain shift and appears as a damping component resulting from moving the slave from its free-running condition. It is also related to the phase offset and injection strength such that:

$$\gamma_{th} = 2\eta\cos\phi_0 = 2(\eta_0/R_{FE})\cos\phi_0 = -g\Delta N_0 \tag{2.22}$$

Again it is necessary to note that the group velocity is implicit in the differential gain term, "*g*", everywhere in this derivation. Using (2.21) to substitute for the slave damping rate in (2.20) and re-writing the expression for "*A*", we have:

$$A = (\gamma_{fr} - \gamma_N)R_{FE}^2 + \gamma_N + \gamma_{th} \tag{2.23}$$

The second and most important term located in the denominator of the response function is "*B*", which corresponds to the overall resonance frequency of the system. Substituting for the threshold gain shift, γ_{th}, in the "*B*" term defined in (2.15) and rearranging yields:

$$B = \eta^2 + \gamma_{th}\left(gA_0^2 + \gamma_N\right) + gA_0^2\left(\gamma_P - \gamma_{th}\right) \tag{2.24}$$

The second term in (2.24), which is related to the steady-state slave locked field and carrier lifetime as ($gA_0^2 + \gamma_N$), effectively appears as a damping rate which can be directly linked to the slave damping rate, γ_{slave}. Using the definition in (2.21), this term can be re-written as follows:

$$B = \eta^2 + \gamma_{th}\gamma_{slave} + gA_0^2\left(\gamma_P - \gamma_{th}\right) \qquad (2.25)$$

By multiplying both sides of the steady-state solution of the locked field found in (2.6) by the differential gain, g, and rearranging γ_P on the right hand side, yields:

$$gA_0^2 = \frac{gA_{fr}^2\gamma_P - \gamma_N g\Delta N_0}{\gamma_P + g\Delta N_0} \qquad (2.26)$$

The first term in the numerator, $gA_{fr}^2\gamma_p$, corresponds to the free-running relaxation frequency squared, ω_r^2. Substituting the threshold gain shift defined in (2.22) allows (2.26) to be rewritten as:

$$gA_0^2 = \frac{\omega_r^2 + \gamma_N\gamma_{th}}{\gamma_P - \gamma_{th}} \qquad (2.27)$$

Substituting (2.19), (2.21) and (2.27) into (2.25) and rearranging will give the following expression for the "B" term:

$$B = \left(\omega_r^2 + 2\gamma_N\gamma_{th}\right) + \left(\eta_0/R_{FE}\right)^2 + \gamma_{th}\left(\gamma_{fr} - \gamma_N\right)R_{FE}^2 \qquad (2.28)$$

For the case of zero injection, η_0 is zero and (2.28) is equal to the relaxation frequency squared of the slave laser, $B = \omega_r^2$, which simply represents the slave's free-running operating condition. Similarly, by applying (2.19), (2.21), (2.22) and (2.27) into (2.16) and rearranging, "C" can be simplified and expressed as:

$$C = \left(\eta_0 / R_{FE}\right)^2 \left[\left(\gamma_{fr} - \gamma_N\right) R_{FE}^2 + \gamma_N \right] - \left(\omega_r^2 + \gamma_N \gamma_{th}\right) Z \qquad (2.29)$$

The "Z" term defined in (2.17) is the zero of the frequency response solution in equation (2.13). This term corresponds to the correlation between the detuning phase offset and linewidth enhancement factor and can be expressed as:

$$Z = \left(\eta_0 / R_{FE}\right)\left(\alpha \sin \phi_0 - \cos \phi_0\right) \qquad (2.30)$$

By manipulating (2.13) and applying the parametric terms expressed in (2.23) and (2.28)-(2.30), the relative modulation response function of a stably locked system can be expressed as:

$$|H_R|^2 = \frac{|H(\omega)|^2}{|H(0)|^2} = \frac{\left(\dfrac{C}{Z}\right)^2 \left(\omega^2 + Z^2\right)}{\left(C - A\omega^2\right)^2 + \left(B\omega - \omega^3\right)^2} \frac{1}{\left(1 + \left(\omega / \gamma_c\right)^2\right)} \qquad (2.31)$$

The second term in the denominator accounts for the parasitic RC circuit in the laser diode and the carrier transport effects where γ_c is considered as a free-running characteristic constant that can be extracted. It is important to note that the response function expressed in (2.31) has a cubic frequency dependence. Depending on the detuning condition, either the *B*-containing or *C/A*-containing poles in the denominator may have a dominant impact on the overall resonance frequency.

Analyzing the parametric terms in (2.23) and (2.28)-(2.30), also indicates that the enhancement of the steady-state field through the injection strength has a significant impact on the modulation response of the coupled system. On one hand, the damping rate described in *A*, can be increased rapidly by the square of the field enhancement factor. On the other hand, the resonance of the coupled system given in *B* also depends on the

deviation of the steady-state field from its free-running value and the maximum injection strength. The *C* term defined in (2.29), balances the interaction between the damping and overall resonance through the zero of the response function, *Z* term, which depends on the steady-state phase offset, the linewidth enhancement factor and injection strength. Therefore, the frequency detuning, injection strength and slave's linewidth enhancement factor are the key operating parameters of the injection-locked system.

The impact of linewidth enhancement factor on the modulation response of an injection-locked nanostructure laser is separately investigated later in this chapter. The impact of increasing injection strength on the enhancement of resonance frequency has been theoretically and experimentally demonstrated by several research groups [8], [15]. However, it is important to note that the resonance frequency of the coupled system also changes dramatically across the locking boundary, from its free-running value (minimum) at the negative frequency detuning edge to its maximum achievable value at the positive frequency detuning edge.

2.2.5 Key Frequency Detuning Cases

The approach presented here is to simulate the modulation response for different values of injection strength and/or frequency detuning and briefly discuss the impact of each factor on the resonance frequency and overall response of the coupled system. Based on the small-signal modulation response derived in (2.31) and the detuning/phase-locking boundaries defined in (2.11) and (2.12), three modulation regimes with unique
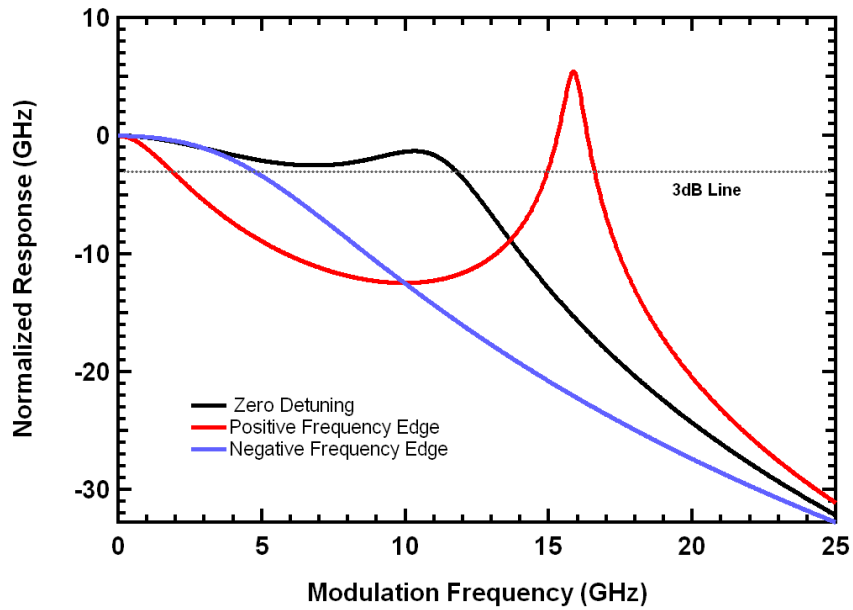
Figure (2.1a) Simulation of the modulation response function under zero, extreme positive and extreme negative frequency detuning at constant injection strength.
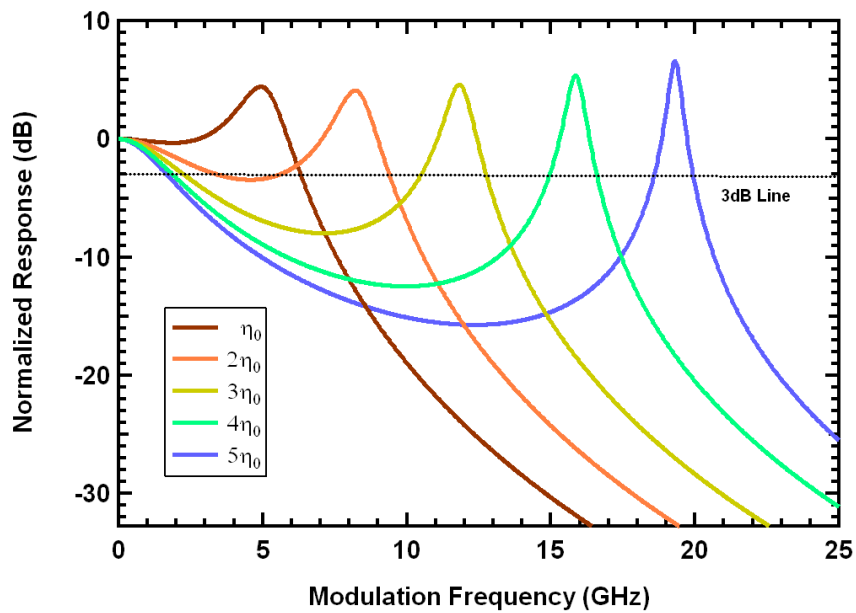
Figure (2.1b) Simulation of modulation response function under positive frequency detuning edge, for various values of injection strength.

characteristics can be observed and are illustrated in Figure (2.1a). All the responses are normalized to a zero DC value. In this simulation, the numerical values for the free-running parameters were chosen from the QDash FP laser studied in this work. In Figure (2.1a), the modulation responses at the negative frequency edge, at zero detuning, and at the positive frequency edge were simulated using a fixed maximum injection strength. At the negative frequency detuning edge, the steady-state phase boundary is defined by the slave laser's linewidth enhancement factor as $\cot^{-1}(\alpha)$. The modulation response in this case is heavily damped and there is no evidence of a resonance peak, making the 3-dB bandwidth relatively small.

The positive frequency detuning edge is characterized by a sharp and high resonance peak. The resonance peak is proportional to the injection strength and is now enhanced in comparison to the free running case. The maximum resonance peak is defined when the locking boundary phase is approximately $-\pi/2$. The resonance peak being proportional to injection strength makes the positive detuning edge very attractive for high-speed applications. However, the 3-dB bandwidth does not scale with the resonance frequency. To understand this better, the progression of the resonance frequency enhancement at positive frequency detuning edge with increased injection strength is simulated in Figure (2.1.b). As the injection strength is increased, a pre-resonance dip between the DC value and the resonance causes the response to fall below the 3-dB value and limits the corresponding usable frequencies for broadband applications. Based on real and imaginary pole analysis of the coupled system's response function, the origin of the undesired dip at positive frequency detuning has been previously investigated and detailed results can be found in the literature [10]. The

occurrence of the pre-resonance dip and its impact on the modulation response is briefly summarized here.

Most notably, the pre-resonance dip has not been observed in the two pole system (free-running case). Thus, the pre-resonance dip being presented in the injection-locked system is related to the cubic frequency dependence of the response function given in (2.31). Generally, two of the three competing poles of the response function control the damping and resonance effects in the response which is similar to the case of a two pole system. The pre-resonance dip is basically caused by the third pole of the response function which scales by the injection strength and produces a steep 20 dB/decade roll-off as the modulation frequency exceeds the frequency of the pole [10]. The third real pole, P_{3rd}, of the response function given in (2.31) can be found from the determinant of the frequency response as given in [10]: $P_{3rd} = C/(4B^2+A^2)$. Parametric terms A, B, and C are given by (2.23), (2.28) and (2.29). The size of the dip is inversely proportional to the frequency of the third pole. At low injection ratios the roll-off is weakened by the zero of the function, reducing the dip depth. As the injection strength is increased, P_{3rd} reduces due to the enhancement of resonance (B) which pulls the third pole toward the DC value and causes the dip to become more significant. Based on the relationship between P_{3rd} and parametric terms, increasing the value of C, by increasing the slave laser's bias current (or power), will increase P_{3rd} and reduce the dip. The impact of free-running parameters on the undesired dip are experimentally investigated and presented later in this chapter. Despite the fact that the observed dip generally has an undesired effect on the modulation response, the positive frequency edge case is still useful for narrowband applications.

57
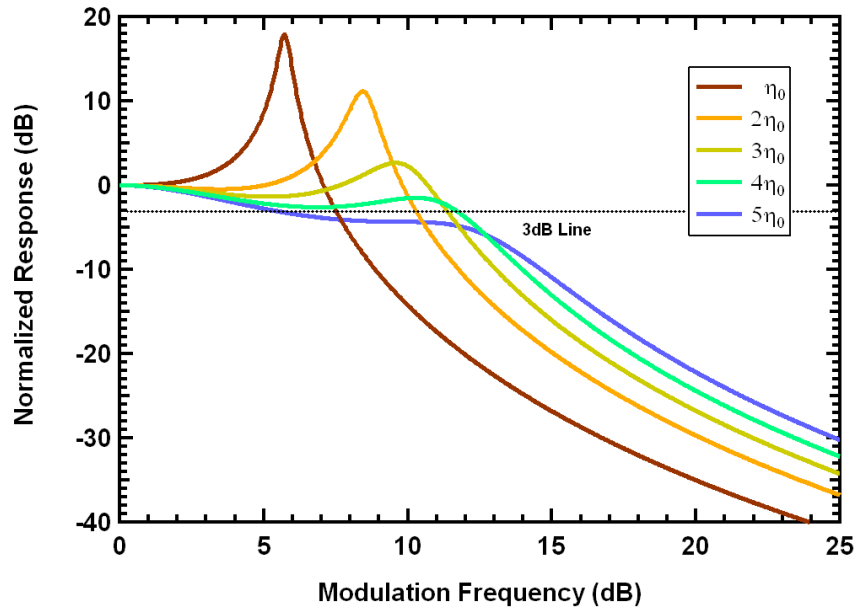
Figure (2.1c) Simulation of modulation response function under zero detuning, for various values of injection strength.

Using this approach, resonance frequencies up to 100 GHz have been reported in injection-locked QW DFB and VCSEL devices [11]. However, there are still various methods to take advantage of the enhanced resonance of the system at the positive frequency detuning case by optimizing the free-running device parameters. This topic is separately investigated in detail in section (2.5.6) of this chapter.

Another interesting detuning scenario is the zero detuning case. Figure (2.1.c) shows the evolution of the zero-detuned modulation responses as a function of injection strength, η_0. Similar to the positive frequency edge case, increasing the injection strength enhances the resonance frequency at the expense of higher damping that reduces the height of the resonance peak under strong optical injections. Most notably, the zero detuning condition has a relatively flat response under strong injection. This flat response can be useful for broadband applications.

58

Chapter 3, studies the impact of strong optical-injection on the slave linewidth enhancement factor under zero-detuning conditions. Choosing a zero-detuning condition for this study is motivated by the following reason. At zero detuning, since $\Delta\omega_{inj}=0$, the steady-state solution of the phase offset given in (2.7) reduces to: $\phi_0 = -\tan^{-1}(\alpha)$. This relationship, simplifies the parametric terms given in (2.23) and (2.28)-(2.30) as well as the relative modulation response function expressed in (2.31). Based on the zero-detuning phase condition expressed above, the γ_{th} and Z parameters given in (2.22) and (2.30) can be simplified using trigonometric identities: $\sin\{-\tan^{-1}(\alpha)\}=\alpha/[1+\alpha^2]^{1/2}$, and $\cos\{-\tan^{-1}(\alpha)\}=1/[1+\alpha^2]^{1/2}$, resulting in the following expressions:

$$\gamma_{th} = 2\left(\frac{\eta_0}{R_{FE}}\right)\cos\phi_0 = \frac{2\eta_0}{R_{FE}\sqrt{1+\alpha^2}} \tag{2.32}$$

$$Z = (\eta_0/R_{FE})(\alpha\sin\phi_0 - \cos\phi_0) = -\left(\frac{\eta_0}{R_{FE}}\right)\sqrt{1+\alpha^2} \tag{2.33}$$

The importance of this simplification is that it eliminates the phase dependence of the threshold gain shift, and the zero pole term (Z) of the response function, makes it easier to model the measured modulation responses and extract the key operating parameters of the injection-locked laser system. Chapter 3 uses the simplified expressions given in (2.32) and (2.33) to extract the resultant shift in the threshold gain and slave's linewidth enhancement factor under strong optical injection strengths.

With the relative modulation response function described in (2.31), along with the parametric terms A, B, C, and Z defined in (2.23), (2.28)-(2.30), the modulation response of the injection-locked laser can be accurately modeled. Furthermore, the validity of the

59

presented model can be verified by least-squares fitting of the measured modulation response data and the key operating parameters of the coupled system can be directly extracted in the microwave domain. The curve-fitting process begins with identifying the key operating parameters of the coupled system included in the modulation response function. The terms A, B, C, and Z, consist of a combination of terms associated with free-running characteristics of the slave laser that remain fixed and the rest of the terms that are linked to the optical injection. These many fitting parameters can be problematic when modeling the experimental data with a least squares fitting method. The following section is focused on a novel approach to solve this problem.

2.2.6 Identifying the Known Free-Running Operating Parameters

By taking into the account all the terms in (2.31) one finds that eight fitting parameters including ω_r, γ_{fr}, γ_N, γ_{th}, η_0, R_{FE}, Z and γ_c are needed for the simulation. All of the terms are expressed as angular frequencies except R_{FE}. Compared to previous research, this method represents a novel experimental approach that allows an easy comparison of the relative magnitudes of the fitting parameters [8]. Since the model is comprised of multiple fitting parameters, there will be many solutions available that can fit the experimental data. Most of these possible solutions can be eliminated by introducing proper restrictions to the operating parameters during least-squares-fitting, such that they can vary only in an acceptable physical range. However, restrictions are not enough to reach a reasonable level of accuracy of the model unless it is combined with a reduction of the freely varying fitting parameters. Fortunately, some of these parameters can be extracted from the intrinsic free-running parameters which can be determined from the slave laser operating characteristics.

The operating parameters of an uncoupled system (free-running slave) can be extracted from the conventional 2-pole modulation response model [16]:

$$|H_R|^2 = \frac{\omega_r^4}{(\omega_r^2 - \omega^2)^2 + \gamma_{fr}^2 \omega^2} \cdot \frac{1}{1 + (\omega/\gamma_c)^2} \qquad (2.34)$$

This expression is used to fit the free-running modulation response and extract three of the fitting parameters: the free-running relaxation oscillation frequency, ω_r, the free-running damping rate, γ_{fr}, and the parasitic roll-off induced by γ_c. These parameters are intrinsic characteristics of the slave laser and remain unchanged when the system is injection-locked. The other fitting parameter found in the free-running characteristics is

the inverse differential carrier lifetime, γ_N. This term can be directly extracted by plotting the known free-running damping rates as a function of the corresponding relaxation oscillation frequencies through the conventional expression $\gamma_{fr} = K f_r^2 + \gamma_N$ [17]. Knowing the value of γ_N is beneficial since it may have a significant impact on the high frequency behavior of the system under modulation. Consequently, the number of fitting parameters can be reduced from 8 to 4 by keeping the free-running terms constant during the simulation. Further constraints on the remaining fitting parameters are found by considering the theoretical limits of coupled system physics. In the following sections (2.3) and (2.4), the experimental setup and required tools needed to characterize the free-running and injection-locked parameters of the slave laser and coupled system are described.

2.3   Free-Running Characterization - Experimental Setup

The experimental setup used to characterize the free-running device is schematically shown in Figure (2.2a). The setup consists of a test laser mount and heat sink, a high-speed probe station, and diagnostics tools such as an optical spectrum analyzer and network analyzer. To prepare for high-speed testing, each device was mounted on a gold-plated C-mount using either indium or silver epoxy. Because the ground contact of the device is located at the bottom of the laser, a ground pad with the same thickness as the laser chip is mounted adjacent to the laser device to bring both the signal and ground contacts to the same level. As illustrated in Figure (2.2b), this configuration is necessary for high-speed testing since it helps to eliminate the parasitic

62
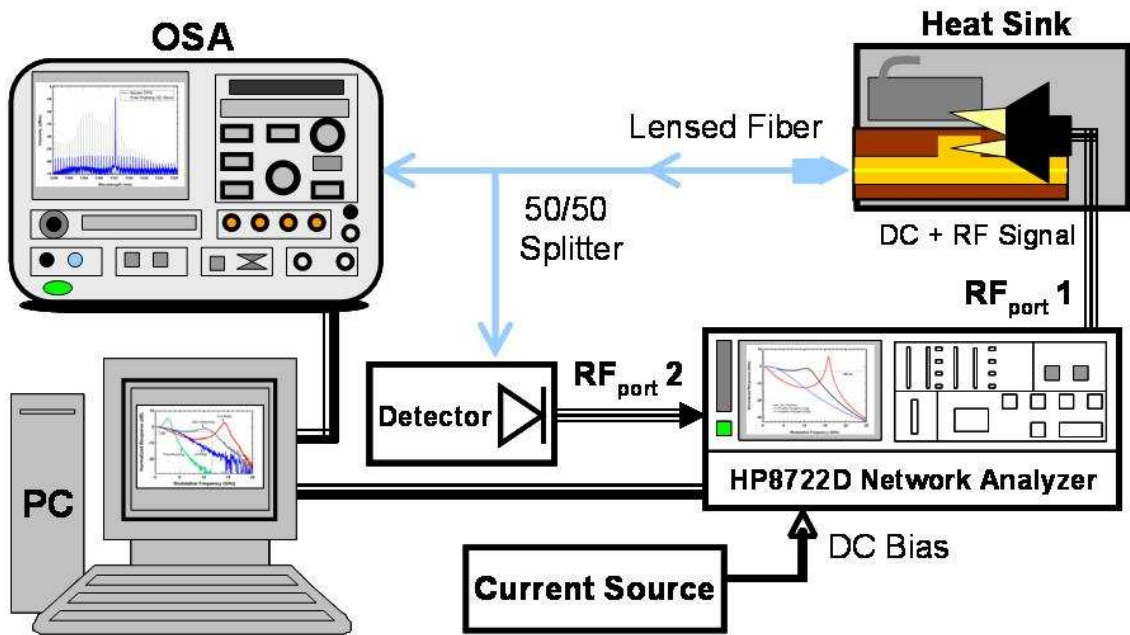
Figure (2.2a) Schematic of the free-running device characterization experimental setup (Not to scale).
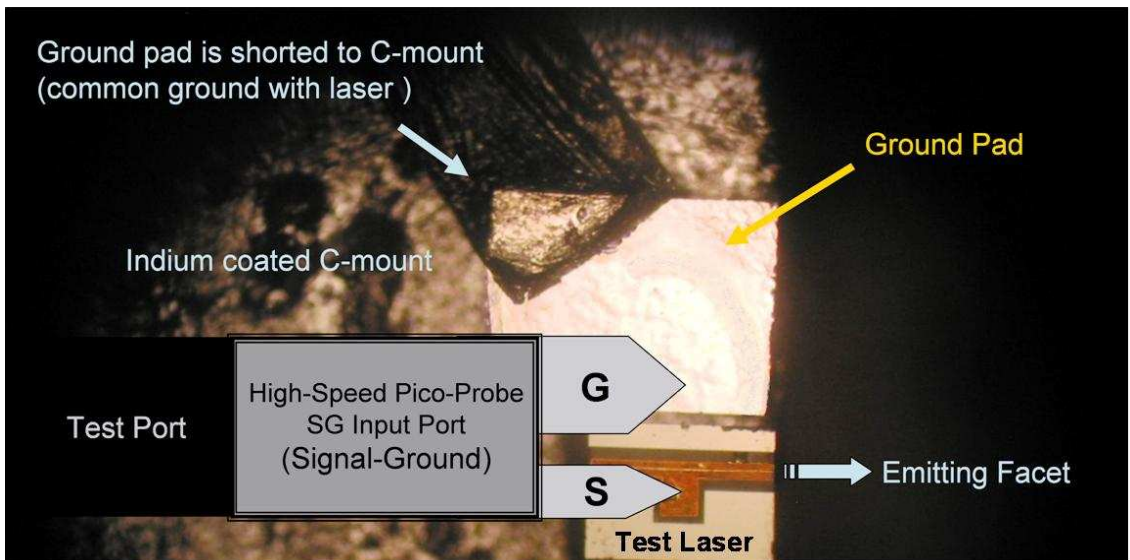
Figure (2.2b) Picture of the high-speed configuration showing the test laser, ground pad and schematic of 40GHz signal-ground Pico-Probe^{TM}.

capacitance and inductance generated from the device under the test. Furthermore, this configuration also enables use of a high-speed signal/ground 40 GHz Pico-Probe^{TM} to minimize high frequency parasitic effects. The C-mount then is clamped on a copper heat sink block, and the desired temperature is maintained by a thermoelectric controller (TEC) unit. DC bias and microwave modulation signals were provided through port 1 of an HP8722D vector network analyzer connected to an ILX continuous-wave current source. Prior to the measurement, a full two-port calibration was performed on the network analyzer to eliminate the parasitic and RF losses in the microwave cables and probes. The laser output was coupled into a lensed fiber mounted on a piezoelectric controlled stage with submicron alignment accuracy, and coupling efficiencies of up to 60% were achieved. Once collected by the lensed fiber, the laser output was sent to the diagnostics parts of the experimental setup. The 50/50 beam splitter allows one to measure the modulation response of the laser while simultaneously monitoring the optical spectra of the test laser. To measure the modulation response ($|S_{21}|^2$), the laser output was collected by a 25 GHz high-speed Discovery semiconductor photodetector (Lab Buddy), which was connected to port 2 of the network analyzer. A high resolution (1.25-1.75 GHz at telecom frequencies) Ando/Yokogawa AQ6319 optical spectrum analyzer (OSA) was used to monitor the optical spectra of the test laser. The light-current characteristics of the slave lasers under test were also measured using a Labsphere integrating sphere.

2.4   Injection-Locking Characterization – Experimental Setup

Figure (2.3) shows the block diagram of the experimental setup used to characterize the injection-locking laser system. In addition to the equipment used for the free-running setup, a tunable master laser, optical circulator, polarization controller, band-pass filter and erbium-doped fiber amplifier (EDFA) are added. Similar to the free-running experimental characterization procedure, the output power of the slave laser was carefully coupled into a single-mode polarization maintaining (PM) lensed fiber using the piezoelectric stage controller. The anti-reflection (AR) coated PM lensed fiber was connected to port 1 of a 3-port PM circulator. The optical circulator serves as the core of the injection-locking setup such that it provides the desired propagation path for the optical signal and blocks undesired light from coupling into the slave and master laser. Depending on the operating wavelength of the slave laser under test, the tunable master laser's wavelength was adjusted appropriately.
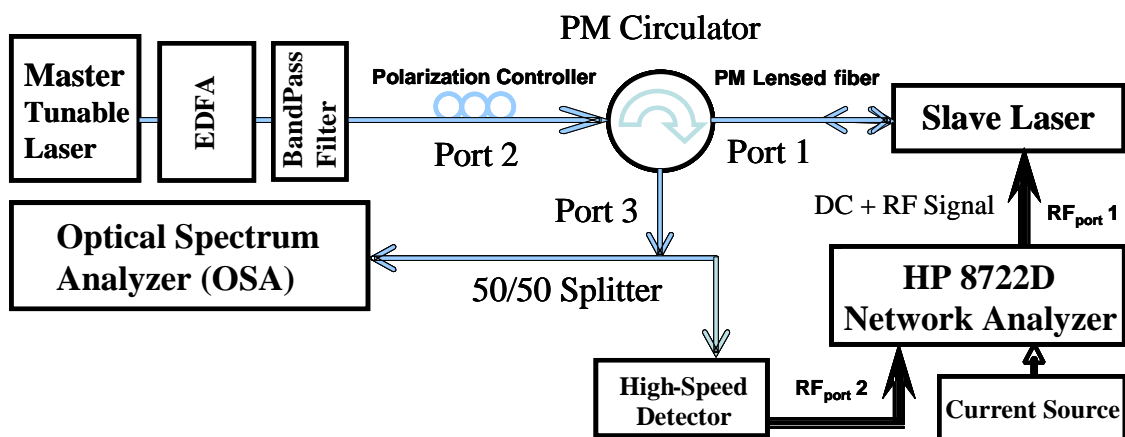
Figure (2.3) Block diagram of the injection-locking experimental setup.

The master laser used for the QDash injection-locking experimental setup was a tunable external cavity laser (New Focus 6200) with a single-mode PM fiber pigtail connected to port 2 of the circulator. The tunable laser operates at wavelength range from 1530 nm-1580 nm with a 10 pm tuning resolution. At port 2, the master laser was connected to a Keopsys EDFA capable of outputting a maximum power of 100 mW to boost the optical signal from the master laser. The amplifier noise is reduced by using a Santec band-pass filter. After the band-pass filter, a free-space polarization controller was used to ensure that the injection field polarization was controlled from the master laser. Port 3 of the circulator was connected to the high-speed Lab Buddy detector through which the relative modulation response ($|S_{21}|^2$) was measured using the HP 8722D network analyzer. The 50/50 beam splitter at port 3 of the circulator was used to measure the modulation response of the injection-locked laser while simultaneously monitoring the frequency detuning between the master and slave lasers. The high resolution OSA (Ando/Yokogawa AQ6319) was used to measure the optical spectra to determine the frequency offset between the master and slave lasers, as well as to identify stably-locked conditions.

2.5 Modeling the Injection-Locked Characteristics of QDash FP Laser

As mentioned in the previous section, reducing the number of fitting parameters and applying reasonable constraints to the remaining fitting parameters improves the confidence in the least-squares-fitting results by decreasing the number of possible solutions. In section (2.2.6), the known free-running parameters required for modeling the coupled system have been indentified. In this section, the free-running operation of the QDash FP device is studied and the key free-running parameters are extracted from measured data. Using (2.34), the free-running relaxation oscillation frequency, free-running damping rate, inverse differential carrier lifetime, and the parasitic RC time constant can be extracted.

2.5.1 Description of the QDash Fabry-Perot Laser

Figures (2.4a) and (2.4b) show the schematic epitaxial layer structure and atomic force microscope (AFM) image of the QDash nanostructure laser device. The QDash laser wafer #258H is a multi-mode FP grown by Molecular-Beam Epitaxy (MBE) on an n^+-InP (001) substrate. The active region is a Dash-in-a-Well (DWELL) consisting of five stacks of InAs quantum dashes embedded in compressively-strained $Al_{0.20}Ga_{0.16}In_{0.64}As$ quantum wells. Each quantum well is separated by 30 nm wide undoped, tensile-strained $Al_{0.28}Ga_{0.22}In_{0.50}As$ spacers on both sides of the DWELL active region. Lattice-matched $Al_{0.30}Ga_{0.18}In_{0.52}As$ waveguide layers of 105 nm are added on each side of the active region. The 1.5-μm thick AlInAs p-cladding layer is beryllium (Be) step-doped to reduce the free-carrier losses. The n-cladding layer is 500-nm thick
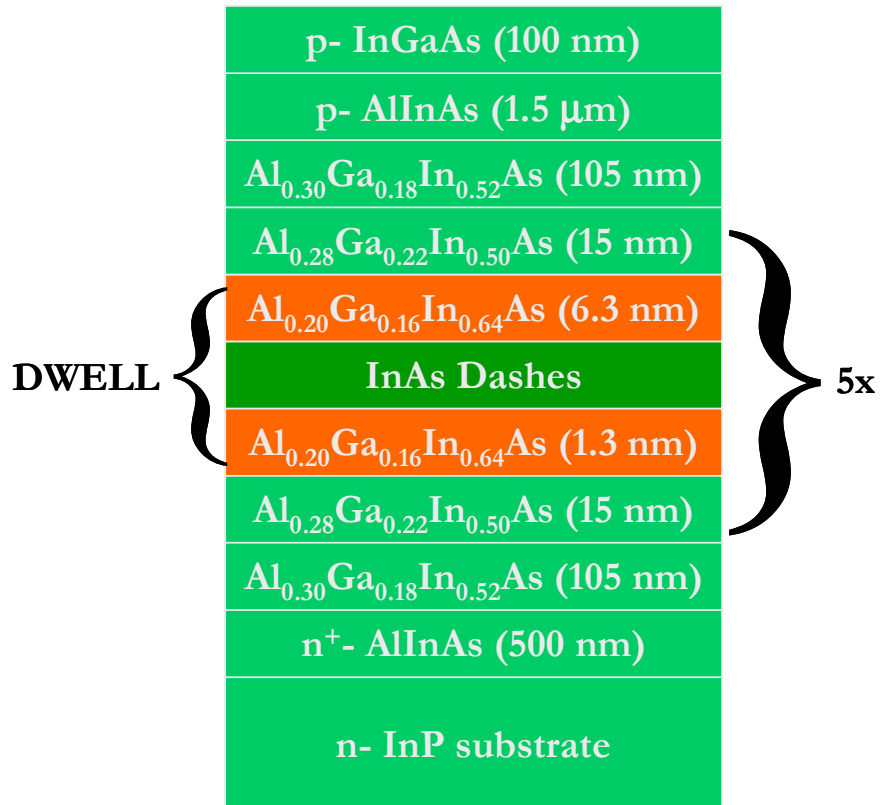
Figure (2.4a) Epitaxial layer structure of the InAs QDash laser.
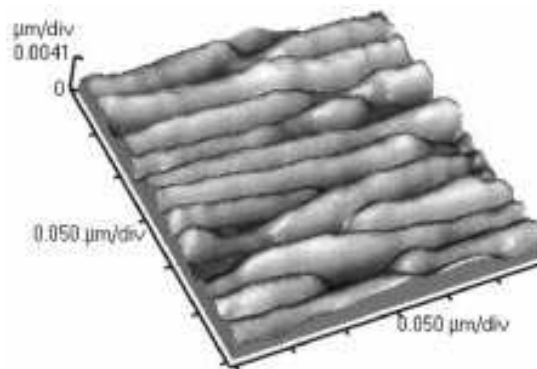
Figure (2.4b) AFM image of the InAs QDash laser material [18].
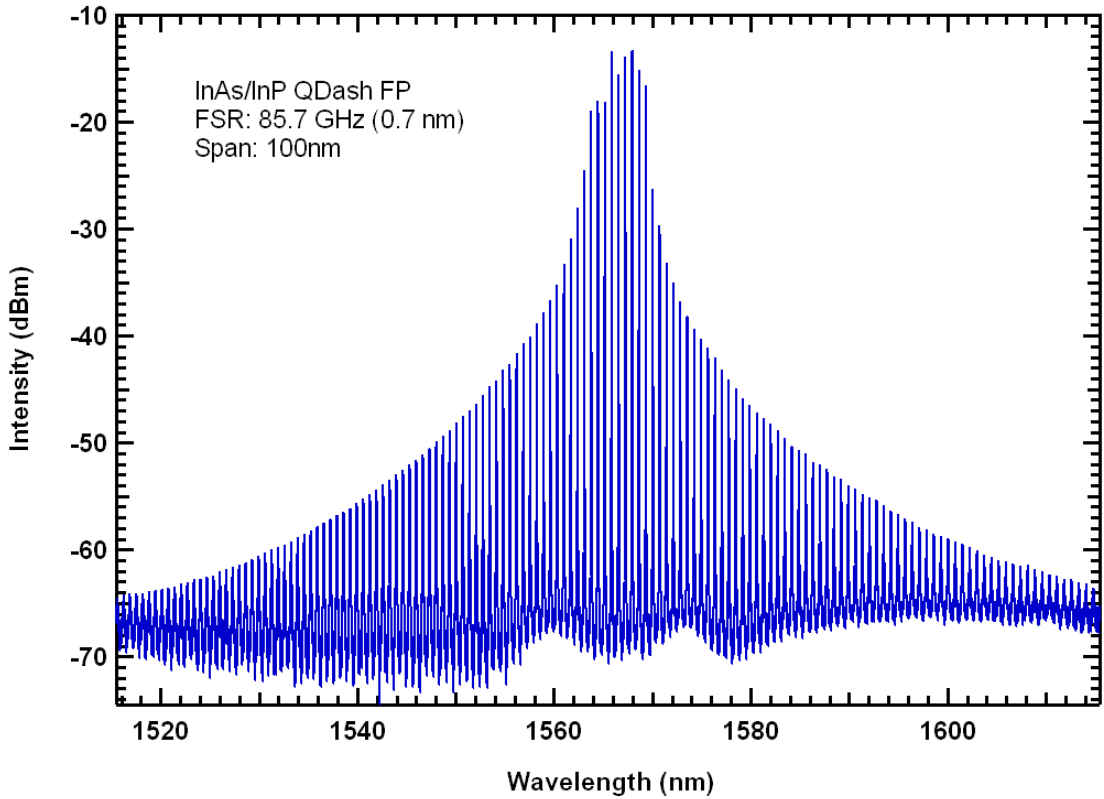
Figure (2.5) Wide-span spectra of the QDash FP laser at bias current of 60mA.

AlInAs [18]. The laser structure is capped with a 100-nm thick p^{++}-InGaAs layer. Four-micron wide ridge waveguide laser bars were fabricated using standard processing techniques and cleaved into 500-µm long cavity lengths. The free-running operation of the QDash laser was characterized using the experimental setup described in section (2.3). The nominal emission wavelength of this FP device is around 1567 nm, the threshold current was measured to be 54 mA (J_{th} ~ 2700 A/cm^2) with a slope efficiency of 0.2 W/A at room temperature. Using the long-wavelength limit of the measured total cavity loss, the internal loss of the QDash material was estimated to be 14 cm^{-1} [19]. The FP modes have an average free-spectral range (FSR) of 0.71 nm (85.7 GHz) across the 100 nm span shown in Figure (2.5). The average FSR yields an average group index, n_g,

69

of 3.5 for the QDash active material. Given the cleaved facet reflectivity of $R_1=R_2=0.32$, cavity length of $L=0.05$ cm, internal loss of $\alpha_i=14$ cm^{-1}, and an average group index of $n_g=3.5$, the threshold gain was calculated to be 36.8 cm^{-1} which yields a photon lifetime, τ_p, of 3.2 psec.

2.5.2 Determining the QDash Laser Free-Running Parameters and the Nonlinear Effects

The free-running microwave parameters were obtained by fitting the free-running response curves measured for the QDash FP device to the conventional modulation response function expressed in (2.34). Figure (2.6a) shows the measured free-running modulation response of the QDash device along with the curve-fitting results. This examination of the free-running laser operating yielded a free-running relaxation oscillation frequency of $f_r=$ 2.7 $\pm$0.02 GHz, a free-running damping rate of $\gamma_{fr}=$ 7.4 $\pm$0.32 GHz and a parasitic RC rate of $\chi_c=$67 $\pm$0.4 GHz. The error for the free-running values were measured based on a one standard deviation confidence interval, and are observed to be less than 5% of their extracted values. In addition to these three values, the inverse differential carrier lifetime, γ_N, was found by plotting the free-running damping rate as a function of the relaxation oscillation frequency squared, f_r^2, as shown in Figure (2.6b). The corresponding value for γ_N is determined at the intersection of the plotted data with the y-axis and was found to be approximately 4.8 $\pm$0.3 GHz. The K-factor, which is found from the slope of the curve in Figure (2.6b), is 0.45 ns and includes the effects of non-linear gain compression in the usual manner [17], [20].
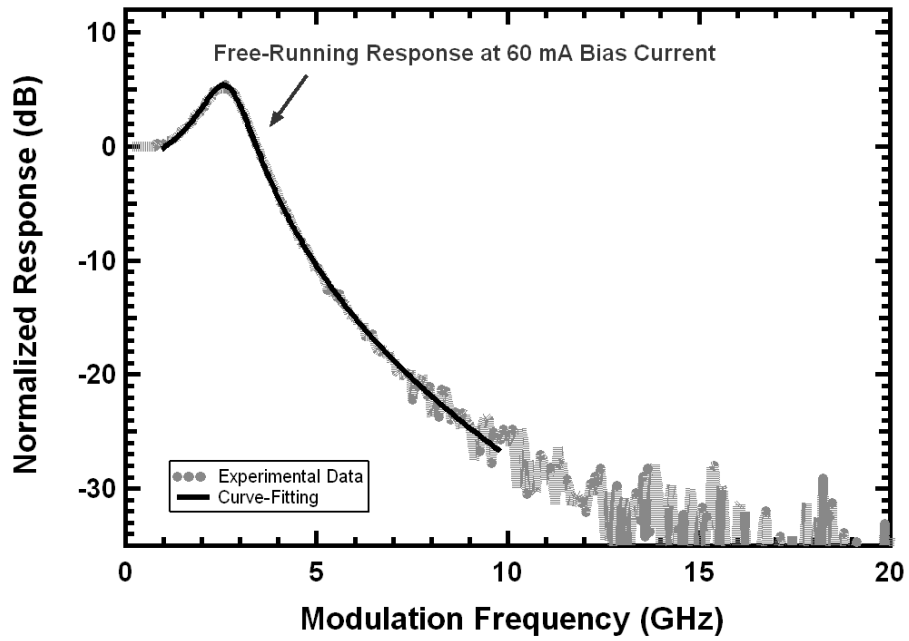
Figure (2.6a) Measured free-running modulation response of the QDash FP device biased at 60 mA and the least-squares fitting results using (2.34).
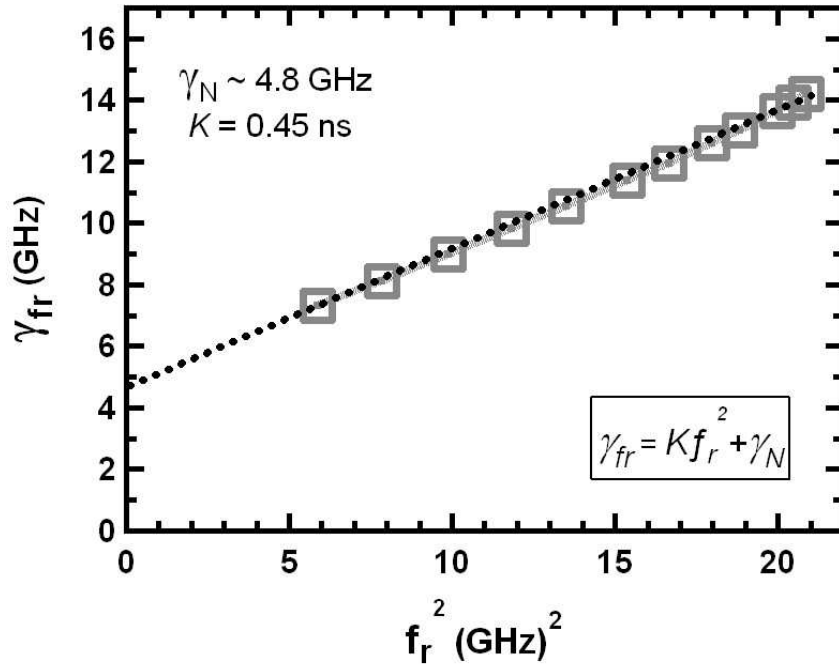
Figure (2.6b) Free-running damping factor as a function of the square of the relaxation oscillation frequency.
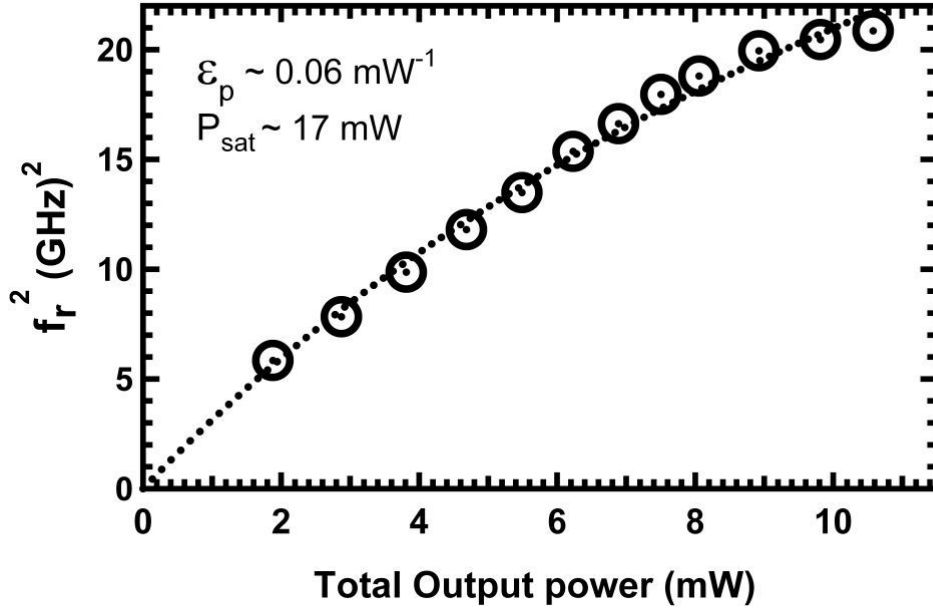
Figure (2.7) Square of the relaxation oscillation frequency versus the free-running output power.

The impact of non-linear gain on the free-running relaxation oscillation frequency can be studied through the following relation [21], [22]:

$$f_r^2 = \frac{C_f P_{out}}{1 + \varepsilon_p P_{out}} = \frac{C_f P_{out}}{1 + \dfrac{P_{out}}{P_{sat}}} \qquad (2.35)$$

where, ε_p, is the gain compression factor related to the output power P_{out} and C_f is a fitting constant. The ratio of P_{out} / P_{sat}, estimates the impact of gain compression at a given output power through the introduction of the saturation power, P_{sat}. Based on the relation described in (2.35), the impact of non-linear gain compression is incorporated, in part, into the injection-locking model through the free-running relaxation oscillation frequency which will be kept constant during simulation. Figure (2.7) shows the variation of the relaxation oscillation frequency squared as a function of the output power for the

QDash device. Using (2.35) to fit the experimental data illustrated in Figure (2.7) results in a saturation power of P_{sat} ~17 mW, a gain compression factor of ε_p ~ 6×10^{-2} mW^{-1} and a maximum free-running relaxation oscillation frequency of 7.6 GHz [22].

2.5.3 Modulation Response of the Injection-Locked QDash FP Device: Experimental Findings

In this section, using the experimental setup described in section (2.4), the modulation response of the stably injection-locked QDash FP device is examined at different detuning cases using the modulation response function derived in (2.31).

Figure (2.8) shows the free-running and injection-locked QDash modulation responses measured under zero and extreme detuning scenarios. The slave laser was injection-locked at the mode closest to 1565 nm. The injected power provided by the master laser at the slave arm (port 1 of the circulator) and the total slave power from both facets were measured to be 3.5 dBm and 4.7 dBm, respectively. The Side-Mode Suppression Ratio (SMSR) for stable locking was taken to be 30 dB; using this criterion, stable locking was observed for detuning frequencies from 13.5 GHz to -17.1 GHz. At the zero frequency detuning condition, a 3-dB modulation bandwidth of 11.7 GHz was observed which corresponds to a three-fold improvement relative to the free-running case. At the positive frequency detuning edge, the measured response exhibits a large dip as well as a high resonance peak. Due to significant damping, only a slight improvement in the bandwidth is observed for the negative frequency cases.
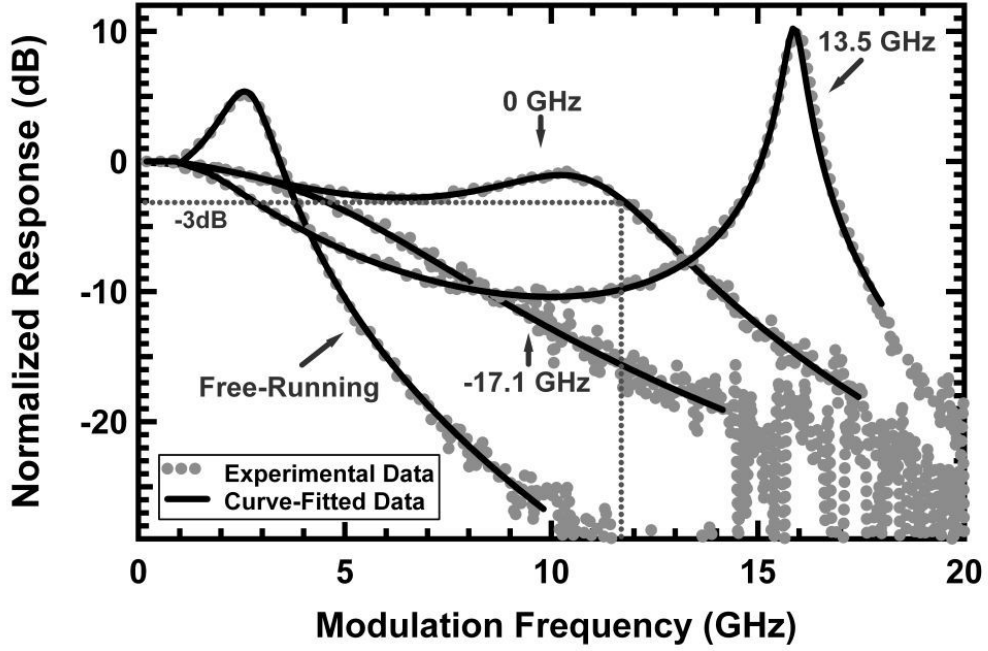
Figure (2.8) Modulation responses of the free-running and the injection-locked QDash laser under zero, positive and negative frequency detuning conditions.

As described in the previous section, reducing the number of fitting parameters and applying reasonable constraints to the remaining fitting parameters improves the confidence in least-squares-fitting results by decreasing the number of possible solutions. The following section discusses the fitting parameter constraints on the remaining terms.

2.5.4 Fitting Parameter Constraints

In order to reduce the number of possible solutions in this curve-fitting, it is necessary to put additional constraints on the four remaining fitting parameters, γ_{th}, R_{FE}, η_0 and Z, which are introduced by the injection-locking state. Due to the interrelationship between these four parameters, constraining them reduces to restricting ϕ_0, η_0, R_{FE}, and

74

the linewidth enhancement factor. This transformation is important because the linewidth enhancement factor of the investigated QDash FP laser has been found to change from ~1.0 to 11 above threshold [23]. This order of magnitude change in the linewidth enhancement factor is unique to this nanostructure laser.

The constraints on the phase offset, ϕ_0, are based on the allowed locking range through the threshold condition and considering (2.11). The result is that the phase offset varies between $-\pi/2$ for positive frequency detuning up to $\cot^{-1}\alpha$ for negative frequency detuning. At the extreme positive frequency detuning case, the phase offset between the master and slave should be $-\pi/2$. According to the phase condition at the positive frequency detuning edge, the value of the field enhancement factor, R_{FE}, should be 1, since the slave's steady-state field matches the free-running field due to the 90 degree phase offset between the master and slave. For all other possible values of detuning, R_{FE} is greater than 1.

The maximum injection ratio, η_0, can be extracted directly from known device characteristics and controllable parameters in the experimental setup. Using the fiber coupling efficiency, η_c, the external power ratio, R_{ext}, (ratio of the master to the slave power measured outside of the slave's front facet), cavity length, L, and front facet reflectance, r, of the FP slave laser, the maximum injection ratio is given as [24]:

$$\eta_0 = \frac{c}{2n_g L}\frac{\left(1-r^2\right)}{r}\sqrt{\eta_c R_{ext}} \qquad (2.36)$$

where c is speed of light in free space and n_g is the optical group index. Using (2.36) and given a slave laser cavity length of 0.05 cm, group index of 3.5, a mirror reflectivity of $r^2 = 32\%$ for the cleaved facet, a coupling efficiency of 0.6 and an external power ratio of

1.5, the maximum injection ratio, η_0, was found to be 98 GHz. As the coupling efficiency was carefully maintained during these experiments, the maximum injection ratio was kept constant throughout the experiment. Since physically the threshold gain shift, γ_{th}, cannot exceed the photon decay rate γ_P, it is also important to verify that the calculated $2\eta_0$ is less than γ_P, which in this case is 313 GHz.

The linewidth enhancement factor, α, of semiconductor lasers can be separately measured using several techniques each with different advantages and limitations, which are summarized in chapter 3. In this work, the free-running value of the above-threshold linewidth enhancement factor for each nanostructure device was measured by using the injection-locking technique [22], [25]. The advantage of this method over other α-measurement techniques is that no fitting-parameters are required, which reduces the uncertainty of the measurement. This method takes advantage of the asymmetry in the stable locking region over a range of detuning on both the positive and negative side of the locked mode. Based on this technique, the linewidth enhancement factor can be found using the following expression [25]:

$$\alpha = \sqrt{\left(\frac{\Delta f_{neg}}{\Delta f_{pos}}\right)^2 - 1} \qquad (2.37)$$

where, Δf_{neg} and Δf_{pos} correspond to the negative and positive frequency detuning ranges which are determined by a SMSR limit of 30 dB. It is important to note that the value of the SMSR is judiciously chosen depending on the limitations of the experiment. In this case the SMSR is chosen large enough such that the weak side modes of the slave laser that are next to the injection-locked mode are always observable above the noise floor. Furthermore, for cases when the SMSR is chosen below 30 dB, these side modes may
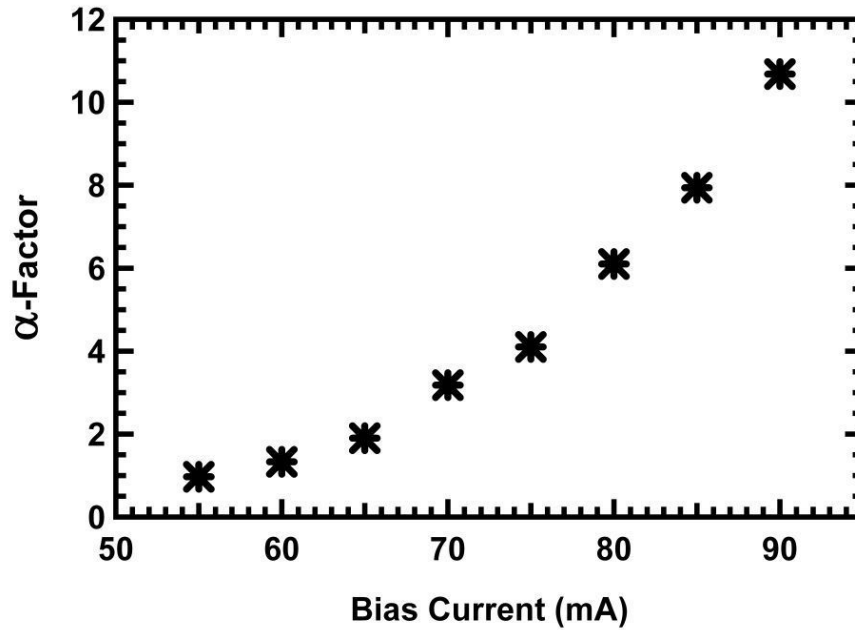
Figure (2.9) Variation of linewidth enhancement factor as a function of applied bias current in the QDash FP laser.

have a significant influence on the injection-locking stability boundary, causing an unreliable measurement for linewidth enhancement factor [26]. Using this method the value of the linewidth enhancement factor can be measured through injection-locking boundaries for a specific applied bias current.

Figure (2.9) shows the variation of linewidth enhancement factor as a function of applied bias current for this device, which increases from ~1.0 to 11 as the applied bias current is increased from its threshold value to 90 mA. According to the results obtained from this measurement, the value of the linewidth enhancement factor is allowed to fluctuate as the detuning is adjusted based on the observation of large variations in linewidth enhancement factor for this device, and attributed to the carrier density not

being clearly clamped at threshold in the QDash FP laser under test [23]. This is one of the major differences in modeling the injection-locking behavior of the QDash laser.

2.5.5 Curve-Fitting Results

The parameters that were allowed to vary in the curve-fitting included the linewidth enhancement factor, α, phase offset between the master and slave laser, ϕ_0, and field enhancement factor, R_{FE}. All other fitting parameters are fixed and the curve-fitting constraints are summarized in Table (2.1). The error for the parameters given in Table (2.1) was not carried forward into the least-squares-fitting of the coupled system as they were less than 5% and thus considered to be negligible. Least-squares curve-fits of the experimental data using the modulation response function presented in (2.31) and the parametric terms described in (2.23), (2.28)-(2.30) are shown in Figure (2.8).

TABLE (2.1)

Fixed fitting parameters and summary of constraints used in the least-squares-fitting under a bias current of 60 mA.

Fixed Fitting Parameters				
f_r (GHz)	γ_{fr} (GHz)	γ_N (GHz)	γ_c (GHz)	η_0 (GHz)
2.7 ±0.02	7.4 ±0.32	4.8 ±0.3	67 ±0.4	98
Fitting Parameter Constraints				
$\alpha \geq 0$		$R_{FE} \geq 1$		$-\pi/2 \leq \phi_0 \leq \cot^{-1}\alpha$

The free-running device parameters were held constant in the modulation response function expressed in (2.31). The maximum injection ratio was constrained to be 98 GHz, as the coupling efficiency was carefully maintained during the measurements. The extracted phase shift was constrained between $-\pi/2$ and $\cot^{-1}\alpha$. The field enhancement factor, phase offset, and linewidth enhancement factor were directly extracted through curve-fitting using (2.31) and the threshold gain shift was calculated for each detuning case by using (2.22). The operating parameters extracted through least-squares-fitting data collected for various measured detuning cases are presented in Table (2.2). The error based on a one standard deviation confidence interval is also shown in Table (2.2). The error associated with α, R_{FE}, γ_{th}, and ϕ_0 are observed to be negligible for all detuning values away from the negative frequency detuning boundary. As the negative frequency detuning boundary is approached, the error increases for the extracted parameters. This is because, as shown in Figure (2.8), the response becomes over-damped, which decreases the amount of information that can be extracted from a least-squares-fit of the corresponding modulation responses. Simulations using (2.31) show that as ϕ_0 approaches zero, changes to the values of α, R_{FE}, and γ_{th} result in only minor changes to the modulation response.

The calculated values for the threshold gain shift, γ_{th}, show an increase as the detuning goes from positive to negative values. This trend is consistent with the induced threshold shift increasing as the injected and slave fields become more and more in phase from positive to negative frequency detuning.

79

TABLE (2.2)

Extracted injection-locking operating parameters from least-squares-fitting of experimental data with response model in (2.31).

Δf (GHz)	α	ϕ_0 (rad)	R_{FE}	γ_{th} (GHz)
13.5	1.59 ±0.07	-1.57 ±0.001	1.00 ±5×10^{-4}	0.16 ±0.2
11.0	2.47 ±0.08	-1.48 ±0.002	1.06 ±8×10^{-4}	16.8 ±0.4
9.9	2.46 ±0.08	-1.45 ±0.003	1.09 ±1×10^{-3}	21.7 ±0.5
6.1	2.50 ±0.04	-1.37 ±0.003	1.24 ±1×10^{-3}	31.5 ±0.4
4.9	2.55 ±0.04	-1.35 ±0.003	1.27 ±1×10^{-3}	33.8 ±0.4
0	2.66 ±0.04	-1.21 ±0.006	1.40 ±2×10^{-3}	49.4 ±0.7
-3.7	2.67 ±0.05	-1.09 ±0.01	1.48 ±5×10^{-3}	61.2 ±1.3
-8.6	2.55 ±0.09	-0.95 ±0.03	1.52 ±1×10^{-2}	75.0 ±2.9
-13.5	2.33 ±0.2	-0.58 ±0.2	1.60 ±5×10^{-2}	102.5 ±8.4
-15.9	2.06 ±1.7	-0.17 ±0.2	1.79 ±2×10^{-1}	107.4 ±21
-17.1	2.00 ±1.8	-0.03 ±0.2	1.80 ±2×10^{-1}	108.8 ±23

The fitting results also show that the value of the field enhancement factor, R_{FE}, increases as the frequency detuning is changes from the positive edge to the negative edge. This trend corresponds to theory describing an increase in the slave laser steady-state power under negative detuning conditions [24]. The extracted phase shift results are consistent with the theory stating that stable locking occurs for phase ranges from $-\pi/2$ to $\cot^{-1}\alpha$. The extracted values of the linewidth enhancement factor for different detuning

cases vary consistently within the expected range which was measured separately for this device as reported in Figure (2.9).

As also shown in Table (2.2), the extracted values of the linewidth enhancement factor vary with detuning within the experimental error range. This leads to the conclusion that linewidth enhancement factor can be manipulated by adjusting the detuning condition. This is a potentially useful result for future low-chirp applications.

2.5.6   Model-Based Analysis

With the validity of the modulation response model verified based on experimental data, it can be used to predict injection- locking behaviors for any FP slave laser once its free-running parameters are known.

By knowing the operating parameters of the system, it is then possible to predict the optimum operating limits of the device such as particular detuning frequencies and the maximum possible bandwidth. One key parameter having a prominent effect on the modulation response is the linewidth enhancement factor. The undesirable dip observed in the modulation response for the extreme positive frequency detuning, as shown experimentally in Figure (2.8), can be removed by increasing the linewidth enhancement factor and keeping the same injection ratio. This situation occurs because an increased α-factor raises Z which increases C which raises P_{3rd} as was described in Section (2.2.5).

In Figure (2.10a) the change in the modulation response under extreme positive frequency detuning due to a change in the linewidth enhancement factor is illustrated theoretically. At the positive frequency detuning edge, the phase offset is roughly $-\pi/2$
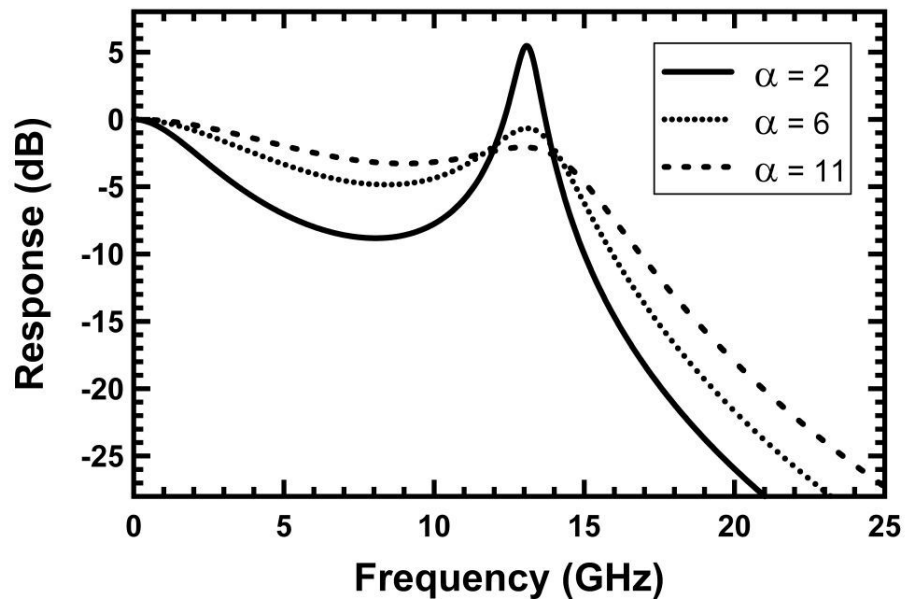
Figure (2.10a) Simulations of the modulation response function for various values of the linewidth enhancement factor.
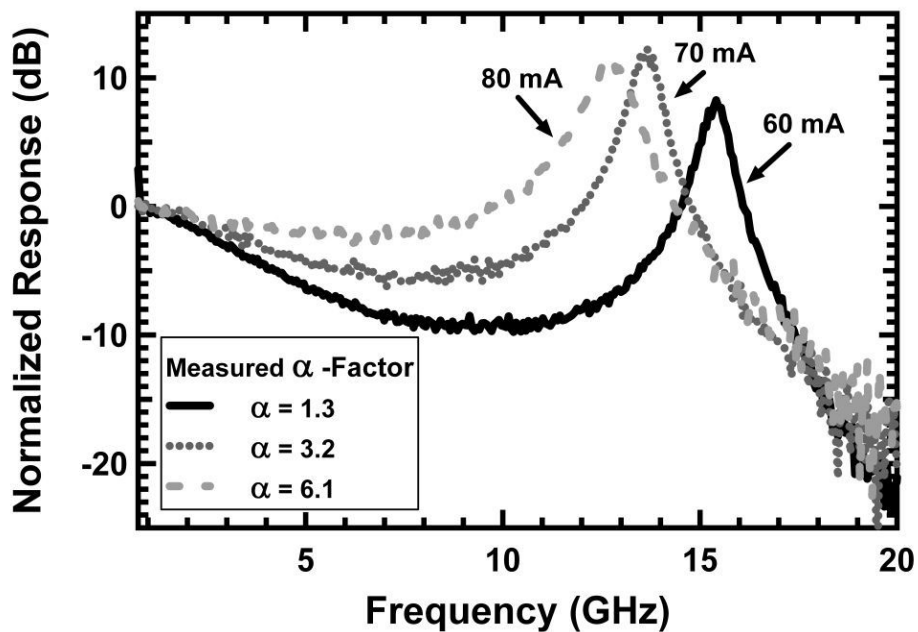
Figure (2.10b) Experimental observation of the varied dip as the linewidth enhancement factor is increased.

82

causing the threshold gain shift to approach zero, $\gamma_{th} \rightarrow 0$, and the field enhancement to become unity, $R_{FE}=1$. The maximum injection ratio and the free-running fitting parameters are kept constant for all three cases. Values used in Figure (2.10a) were based on the extracted physical parameters for the injection-locked QDash FP device under test at extreme positive frequency detuning. The phase offset of, $\phi_0 \approx -\pi/2$ (-1.57 rad), threshold gain shift of, $\gamma_{th}=0.16$ GHz, and the field enhancement factor of, $R_{FE}=1$ were kept constant for all three cases. Ideally, since the linewidth enhancement factor increases significantly in this device (1.0 to 11) larger bias current and slave power, the dip in the modulation response should be removable assuming a high enough injection power is available to maintain a constant injection ratio. The significance of this observation is that because the highest relaxation oscillation frequency and hence the highest possible modulation bandwidth occur at the positive frequency detuning edge, removing the dip will achieve the highest possible modulation bandwidth for the injection-locked system. Figure (2.10b) experimentally demonstrates this trend, showing modulation response curves at the extreme positive frequency detuning edge for bias currents of 60 mA, 70 mA, and 80 mA and linewidth enhancement factor of 1.3, 3.2, 6.1, respectively, as shown in Figure (2.9). The dip is shown to be reduced as the bias current, and correspondingly the linewidth enhancement factor, is increased. Based on the theoretical model expressed in (2.31) and depending on how the B-containing and C/A-containing terms in the denominator interact, the dip reduces as their resonances detune from each other due to the change in the linewidth enhancement factor at different bias levels. As described in Section (2.2.5), an alternative explanation is that the P_{3rd} pole is increasing as the α-factor goes up. The maximum injection ratio for the 60 mA, 70 mA, and 80 mA cases

was calculated by (2.36) to be 103 GHz, 116 GHz, and 107 GHz, respectively. Note that although the peak frequency decreases as the bias current is increased, the magnitude of the peak remains relatively constant. The decrease in the observed relaxation oscillation frequency is likely due to increased device heating as the bias current is increased, along with an increased cavity mode shift [10] which is driven by the linewidth enhancement factor as given in (2.5).

2.5.7 Temperature Effect on the Injection-Locked QDash Laser Modulation Response

In section (2.2), the modulation response function modeling the injection-locked behavior of nanostructure laser systems in the microwave domain was derived and discussed. This function analytically and experimentally (in QDash FP laser) showed that the undesirable dip observed in the modulation response for extreme positive frequency detuning is altered by the linewidth enhancement factor and other free-running parameters of the device under a constant injection ratio. Due to the distinct carrier dynamics in this QDash device, the free-running parameters, including the linewidth enhancement factor, need to be considered in order to optimize the modulation response. This section investigates the impact of QDash slave laser temperature variations on the free-running relaxation oscillation frequency, damping rate, and linewidth enhancement factor, and the resultant effects on the modulation response of the injection-locked system. Figure (2.11) shows the light-current characteristics of the QDash FP device for various temperatures, indicating a   >2 mW increase in the output power as the
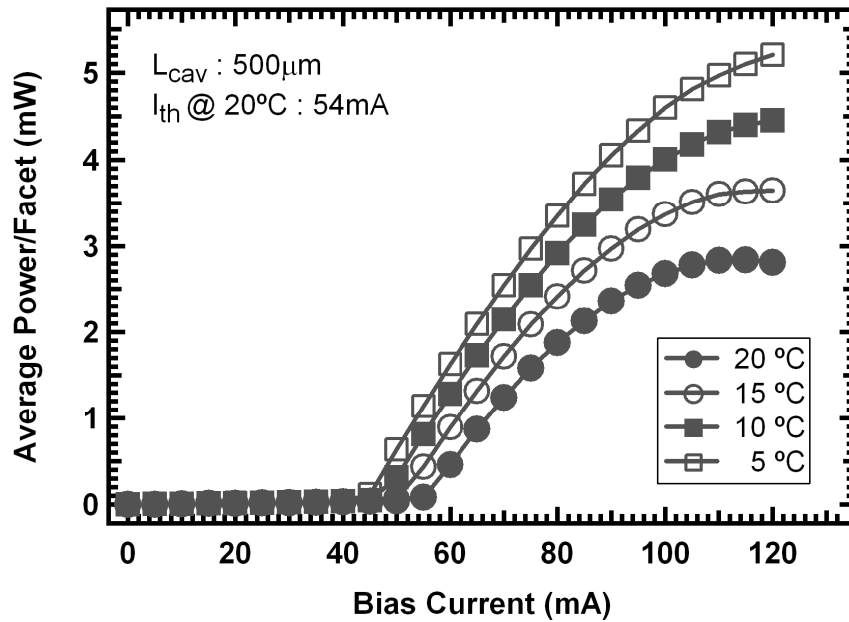
Figure (2.11) Light-current characteristics of the QDash FP device for various temperatures.

temperature decreases from 20°C to 5°C. It is important to note that the strong saturation around 100mA at room temperature is mainly due to the device heating effect.

The slave relaxation oscillation frequency and damping rates are extracted from the free-running responses using (2.34) and their variation with device temperature is illustrated in Figure (2.12) for a constant bias current of 75 mA. Results in Figure (2.12) show an increase in both the relaxation frequency and damping rate of the slave laser as the temperature decreases from 20°C to 5°C. This trend is also consistent with theory which says the slave laser's damping rate and relaxation frequency increase with power.

The variation of the linewidth enhancement factor of the QDash device with device temperature was measured using the injection-locking technique described in section (2.5.4). The unique property of QDash physics, which induces different carrier
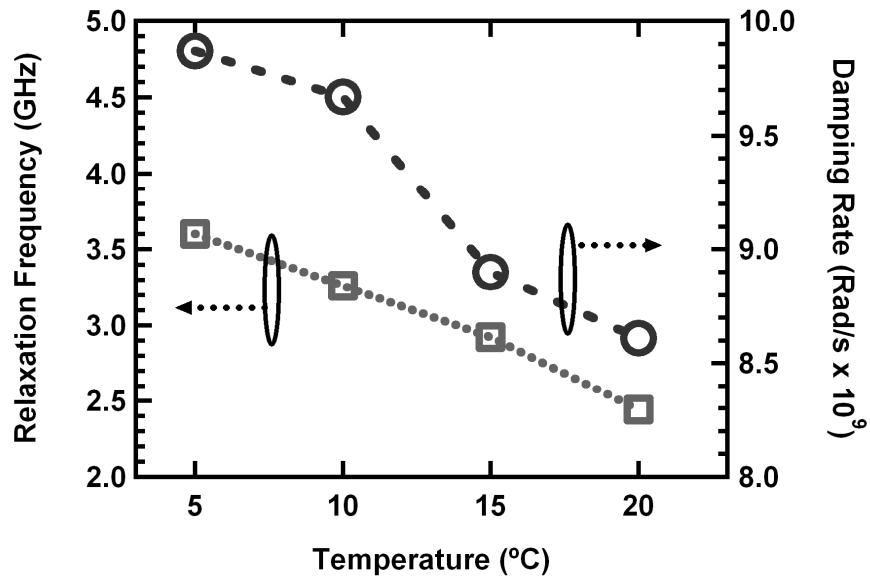
Figure (2.12) Variation in the QDash free-running relaxation frequency and damping rate vs. temperature at a bias current of 75mA.
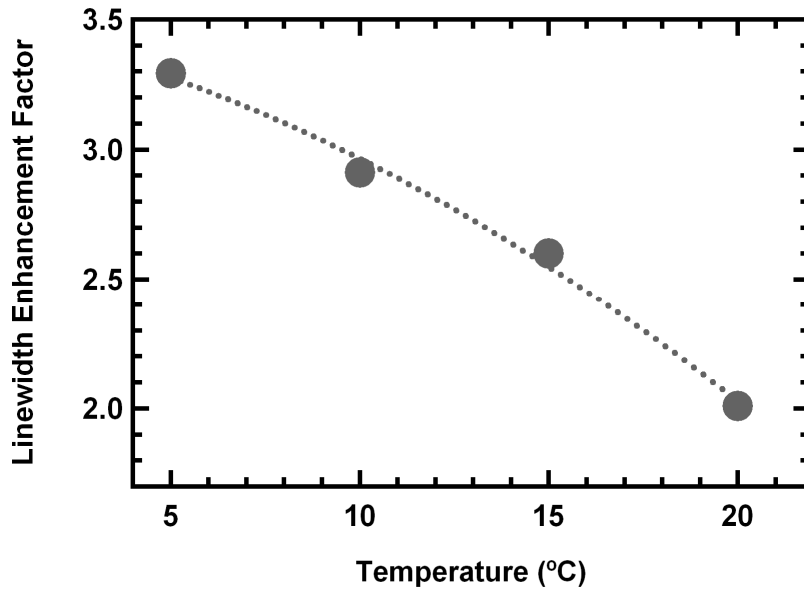
Figure (2.13) Variation in the QDash FP linewidth enhancement factor as a function of temperature.

86

dynamics, makes the above threshold linewidth enhancement factor change with power, P. As the temperature decreases and the bias current is held constant, the product of the gain compression coefficient and power, $\varepsilon_p P$, rises, which increases the linewidth enhancement factor as $\alpha = \alpha_o(1 + \varepsilon_p P)$ [27]. The linewidth enhancement factor value at threshold is given by α_o. The variation in linewidth enhancement factor with temperature is illustrated in Figure (2.13), showing an increase from 2 to 3.3 as the temperature is decreased from 20°C to 5°C.

Using the injection-locking system experimental setup presented in section (2.4), the frequency responses at the positive frequency detuning edge were measured for different slave laser operating temperatures varying from 5 to 20°C (while keeping the injection strength constant).
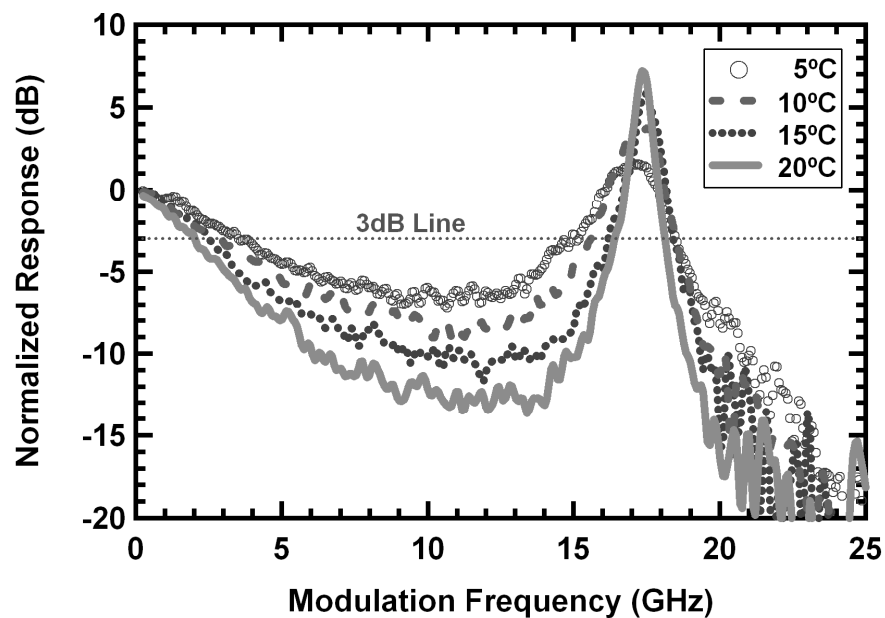
Figure (2.14) Improvement in the injection-locked modulation responses at positive frequency detuning vs. temperature variation.

Since the slave power increases with reduced device temperature, the master laser's power is increased such that the external injected power ratio (master to slave's power ratio at the slave's emitting facet) was kept constant at 5 dB for all the cases. In addition, the coupling efficiency was carefully monitored and kept unchanged to ensure that the injection strength stays the same throughout the measurement. Under stable locking conditions (SMSR $\geq$ 30dB), the positive frequency detuning edges are located around 19GHz. Figure (2.14) shows modulation responses at this extreme positive frequency detuning edge for various temperatures.

This trend shows a significant reduction in the undesired dip by as much as 7dB and is attributed to the increase in the damping rate and relaxation frequency of the slave laser as well as a small increase in the linewidth enhancement factor. Section (2.2.4) theoretically discussed the impact of the third pole of the response function in (2.31) on the sensitivity of the undesired dip. It was found that maximizing the C term reduces the dip. Increasing the slave bias current and/or reducing the device temperature, increases the damping and relaxation oscillation as well as the linewidth enhancement factor due to the increased photon density in the laser cavity. Each of these increases serves in maximizing the C term. As a result, the free-running slave parameters are the key factors in optimizing the injection-locked performance of the nanostructure device.

2.6   Modeling the Injection-Locked Characteristics of a QD FP Laser

This section experimentally investigates the high-speed modulation characteristics of an injection-locked QD FP laser operating at 1310-nm under strong optical injection with a focus on the enhancement of the modulation bandwidth. The coupled system consists of a directly-modulated QD slave injected-locked by a distributed feedback (DFB) laser as the master. At particular injection strengths and frequency detuning cases, a unique modulation response is observed that differs from the typical modulation response observed in injection-locked systems. This unique response is characterized by a rapid low-frequency rise along with a slow high-frequency roll-off that enhances the 3-dB bandwidth of the injection-locked system at the expense of losing modulation efficiency of about 22 dB at frequencies below 1 GHz.

There are two benefits in having this unique response. One benefit is that the resonance frequency enhancement doesn't experience the low frequency dip that was seen in the QDash laser case that limited the amount of useful bandwidth for the high-speed injection-locked response. The second benefit is the improvement in the high frequency roll-off that extends the bandwidth. Also, a 3-dB bandwidth improvement of greater than 8 times compared to the free-running slave laser is achieved.

2.6.1   Description of the QD Fabry-Perot Laser

The epitaxial layer structure of the QD slave laser under investigation is illustrated in Figure (2.15a). The QD slave laser was grown on an n^+-GaAs substrate using molecular beam epitaxy. The Dots-in-a-Well (DWELL) active region consists of 6 layers of InAs QDs embedded in compressively-strained $In_{0.15}Ga_{0.85}As$ QWs each

separated by 30-nm undoped GaAs barrier layers. Each side of the active region was surrounded by a 45-nm waveguide layer of undoped GaAs. The p- and n-cladding were 1.5-µm layers of lattice-matched $Al_{0.7}Ga_{0.3}As$. The laser structure was capped with a 100-nm layer of GaAs. Three-micron wide ridge waveguides laser bars were fabricated using standard processing techniques and cleaved into 300-µm long cavity lengths with front and back facets HR/HR coated at 80% and 95%, respectively, to increase the ground-state gain. The light-current characteristics and the emission spectra of the slave laser under investigation are shown in Figure (2.15b). The QD laser was found to have a threshold current density of 211 A/cm^2 (1.9 mA) with a slope efficiency of 0.23 W/A, and a nominal emission wavelength of approximately 1305 nm at room temperature. The average FSR of the FP modes was found to be ~ 0.806 nm (142 GHz) across the 100 nm span. Using the average FSR of 0.806 nm, yields the average group index of 3.52 for the QD gain media. Given HR/HR facet reflectivities of R_1=0.8, and R_2=0.95, a cavity length of L=0.03 cm, an internal loss of α_i=4 cm^{-1}, and a group index of n_g=3.52, the threshold gain was calculated to be 8.6 cm^{-1} which yields a photon lifetime, τ_p, of 13.7 ps.

The injection-locking experimental setup used to measure the high-speed characteristics of the injection-locked QD laser is similar to the one described in section (2.4). In this case, the master laser was a Fujitsu temperature-tunable QW DFB laser with a nominal emission wavelength of 1315 nm. An ILX temperature controller unit was used to tune the master laser's operating wavelength at a rate of 0.1-nm/°C. The master laser's output was fiber-pigtailed into a single-mode PM fiber that was coupled into the second port of a 3-port PM circulator. The PM circulator is designed to operate around 1310 nm

a)

p-GaAs (100 nm)
p-Al$_{0.7}$Ga$_{0.3}$As (1.5 μm)
Undoped GaAs (45 nm)
Undoped GaAs (30 nm)
In$_{0.15}$Ga$_{0.85}$As (8.1 nm)
InAs QDs
In$_{0.15}$Ga$_{0.85}$As (1.0 nm)
GaAs (45 nm)
n-Al$_{0.7}$Ga$_{0.3}$As (1.5 μm)
n-GaAs Substrate

DWELL

6x

b)

InAs/GaAs FP QD Laser
L$_{cav}$: 0.3mm
I$_{th}$: 1.9mA @20°C

FSR : 142 GHz
λ$_{peak}$: 1305nm @20°C
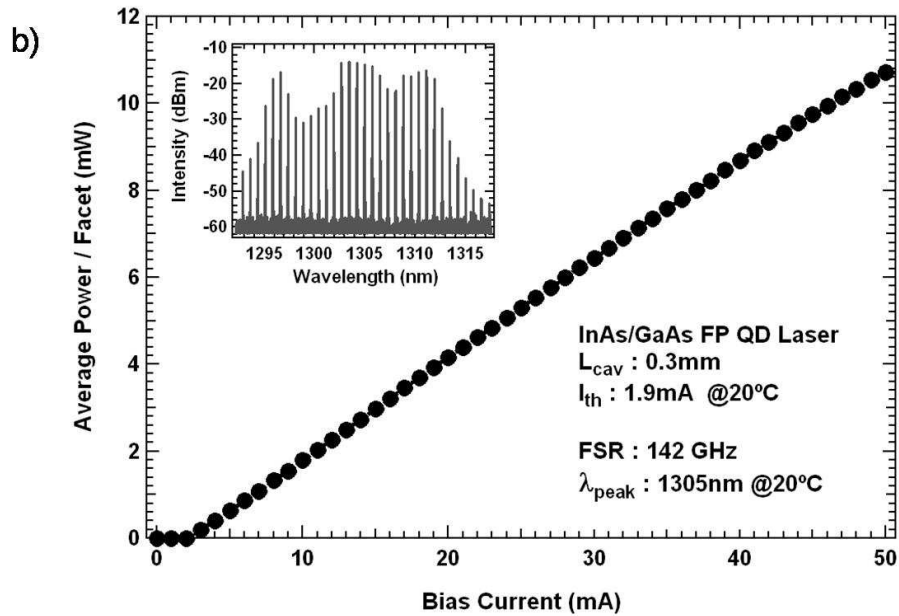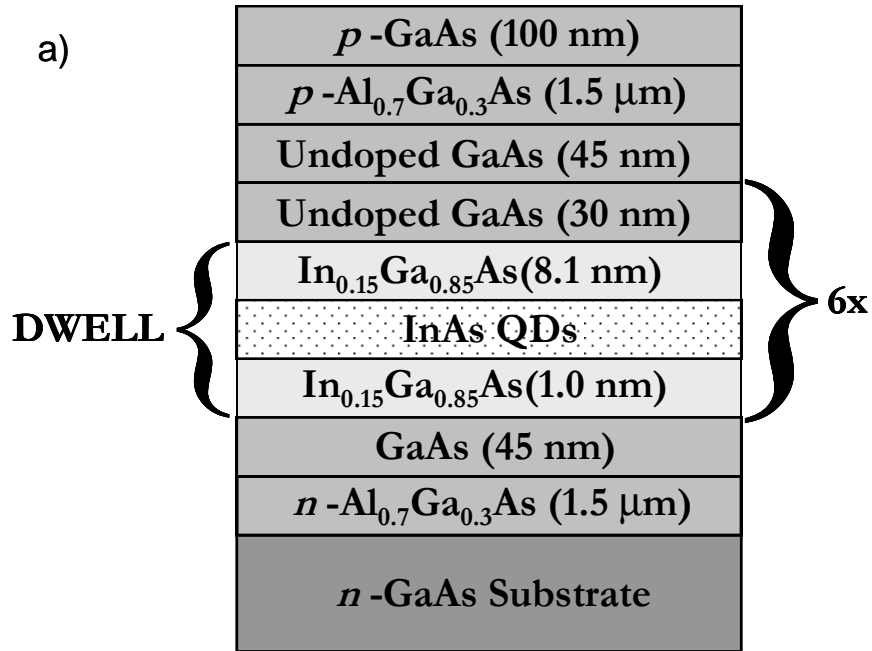
Figure (2.15) a) Epitaxial layer structure of the InAs/GaAs QD slave laser, b) Light-current characteristics and emission spectra of the QD slave laser under investigation.

91

and has an isolation level of >20dB. The biased slave laser was kept at 20°C using a thermo-electric heat sink controlled by a separate temperature controller unit. A precise piezoelectric stage controller with micrometer accuracy was used to obtain a coupling efficiency of 44%. The modulation response ($|S_{21}|^2$) was measured using the HP8722D network analyzer and the 25 GHz Lab Buddy high-speed detector. The slave bias current was supplied by an ILX 3811 current source connected to the network analyzer where the DC current was mixed with a small-signal (-10dBm power level) RF modulation input signal using a bias-Tee integrated inside the network analyzer. Prior to the high-speed measurement, a full two port calibration was performed on the network analyzer to eliminate the transmission loss induced by the high-speed cables and the Pico-probe. A Yokogawa AQ6319 optical spectrum analyzer, with a resolution of 1.75 GHz at 1310nm and a large dynamic range (60dB at maximum resolution), was used to characterize the master and slave lasers frequency detuning and to assure that the stable-locking condition was always satisfied as the detuning and injected power was varied.

2.6.2 Determining the QD Laser Free-Running Parameters and the Nonlinear Effects

The slave free-running relaxation oscillation frequency, damping rate, and parasitic roll-off are determined by least-squares fitting the free-running modulation responses using the conventional response function given in (2.34).

The free-running modulation responses for various applied bias currents (from 5-25 mA) along with the corresponding least-squares curve-fitting results are given in
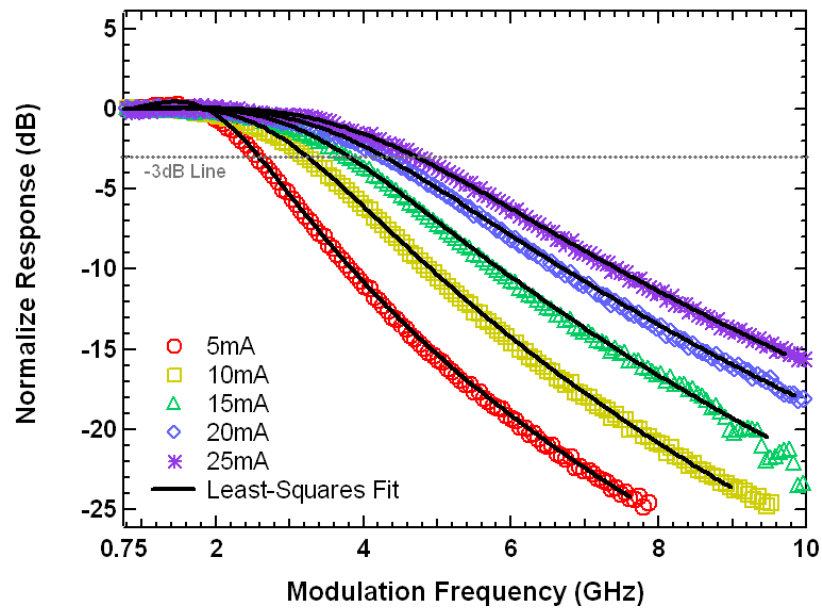
Figure (2.16) Normalized modulation response of the free-running slave laser for various pump currents. The slave modulation responses are curve-fitted with the standard modulation response function given in (2.32).
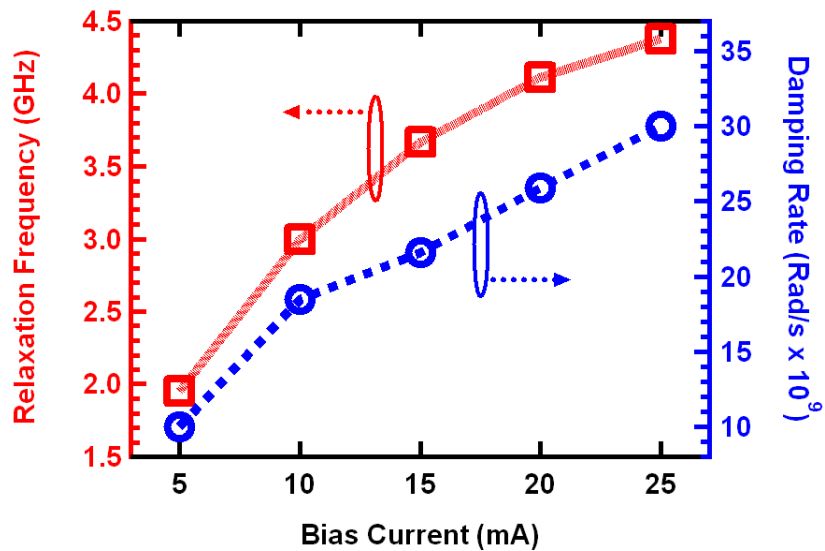
Figure (2.17) Variation of the slave free-running relaxation oscillation and damping rate as a function of bias current.

Figure (2.16). Note the damped response in this free-running QD laser. The slave relaxation oscillation frequency and damping rates are extracted from the free-running modulation responses using (2.34) and their variation with bias current are illustrated in Figure (2.17). Results in Figure (2.17) show an increase in both relaxation frequency and damping rate of the slave laser as the bias current is increased. This trend is consistent with theory, where the damping rate and relaxation frequency increase with photon density.

Using a similar approach described as that used in section (2.5.2) for the QDash device, the differential carrier life time τ_N, was found through the measured QD laser's free-running damping rates as a function of the corresponding relaxation frequencies squared using the conventional expression [17], $\gamma_{fr}=Kf_r^2+1/\tau_N$. As shown in Figure (2.18), the corresponding value for the inverse differential carrier lifetime γ_N, is determined at the intersection of the plotted γ_{fr} vs. f_r^2 data with the y-axis and was found to be approximately 9 GHz. From the slope of the same plot, the K-factor was found to be 1.51 ns.

It is important to note that the injection-locked modulation response function expressed in (2.31) incorporates the contribution of the inverse differential carrier lifetime, which proved to be relatively large for the QD FP slave compared to the QDash device.

The impact of non-linear gain on the free-running relaxation oscillation frequency was studied through the relationship given in (2.35). Similar to the case of modeling the QDash laser, here it was assumed that the impact of non-linear gain compression is implicitly incorporated into the injection-locking model through the free-running

94
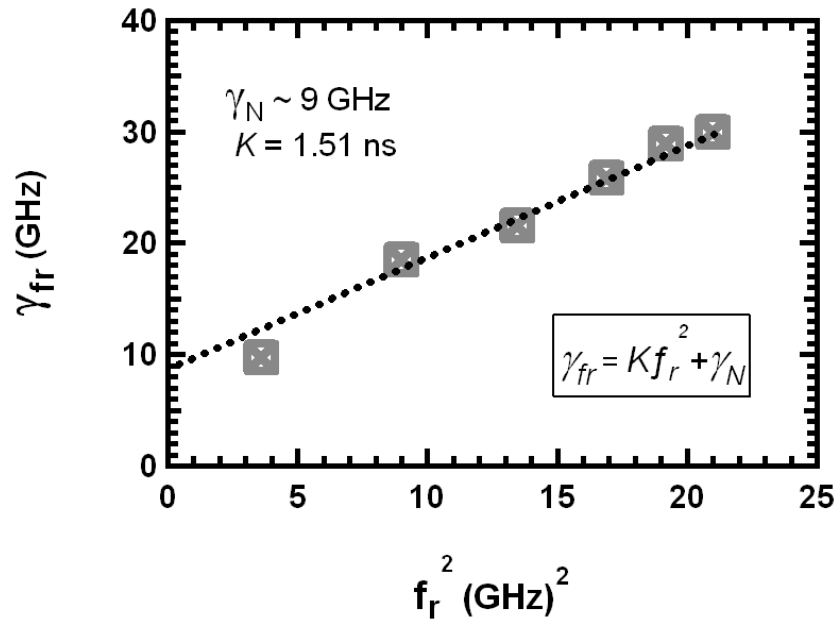
Figure (2.18) QD free-running damping factor as a function of the relaxation oscillation frequency squared.
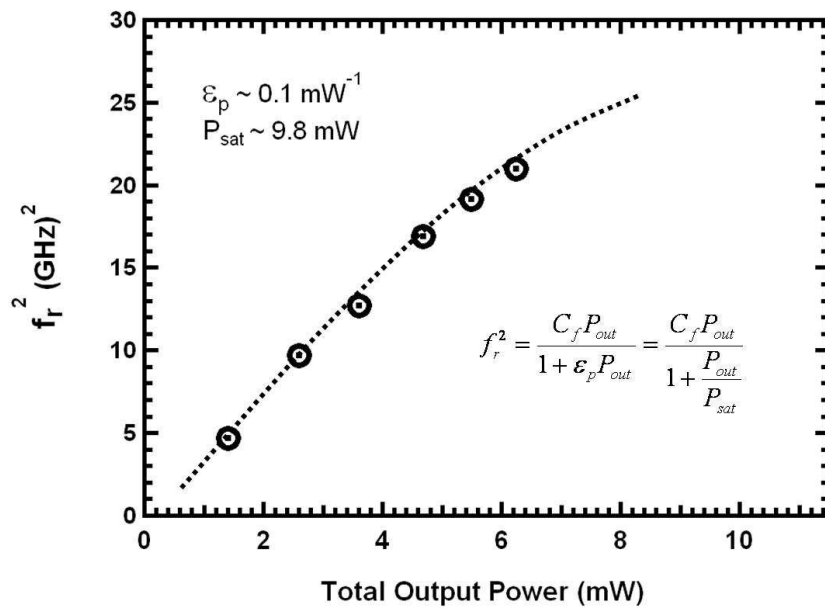
Figure (2.19) QD free-running relaxation oscillation frequency squared as a function of total output power. Inset is the fitting function given in (2.36).

relaxation oscillation and damping rate which were kept constant during simulation. Figure (2.19) shows the variation of the relaxation oscillation frequency squared as a function of total output power for the QD device. Using (2.35) to fit the experimental data illustrated in Figure (2.19), a saturation power of P_{sat} ~9.8 mW and a gain compression factor of ε_p ~ 0.1 mW^{-1} was calculated. These results show that QD FP laser has a stronger gain compression compared to the QDash FP device.

Previous sections studied the impact of the slave's linewidth enhancement factor, α, on the modulation characteristics of the coupled laser system, finding that the linewidth enhancement factor is one of the key operating parameters that has a significant impact on the modulation response of the coupled system. This parameter is separately
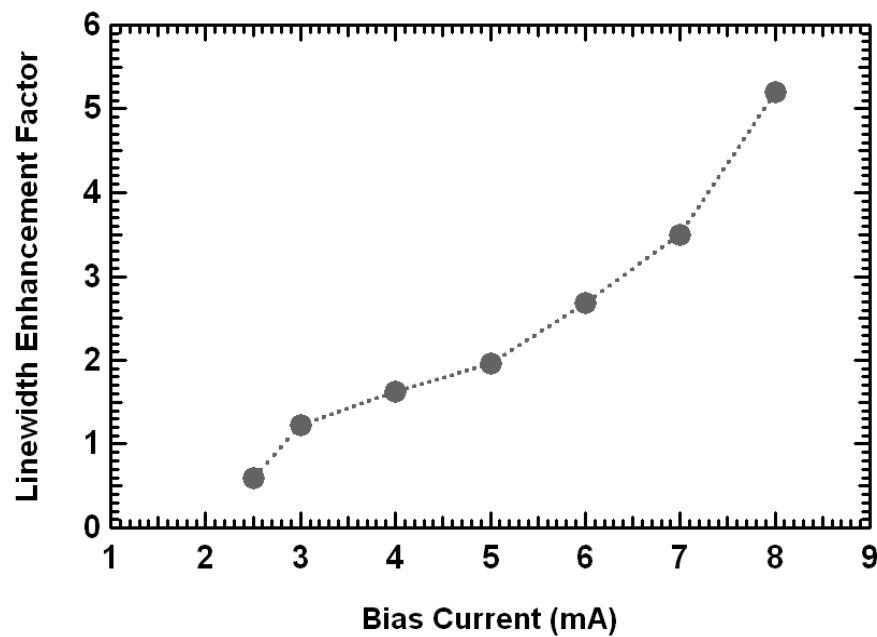
Figure (2.20) Variation of the slave linewidth enhancement factor as a function of applied bias current for a 1310 nm QD FP laser. The linewidth enhancement factor varied from ~0.6 to 5 as the applied bias current is increased from slightly above the threshold value to 8 mA.

96

measured through the injection-locking technique described in section (2.5.4). Using this method, the linewidth enhancement factor is measured at the injection-locking positive and negative frequency detuning boundaries for a given bias current.

In Figure (2.20), the variation of the linewidth enhancement factor for various applied bias currents is shown for the QD device. According to the experimental findings obtained from this measurement, the value of the linewidth enhancement factor was allowed to fluctuate in the injection-locked QD laser simulations as the optical injection is increased or when the frequency detuning between the master and slave lasers is adjusted. The large variation in the linewidth enhancement factor fluctuation for this device is mainly attributed to the strong gain compression at the ground state and the fact that the carrier density is not clearly clamped at threshold in these devices. As in the QDash laser, a variation in the α-factor of nearly an order of magnitude is possible.

The small linewidth enhancement factor of 0.6 at slightly above threshold in the QD FP laser under investigation promises unique modulation characteristics under optical injection compared to QDash devices which were shown to have a higher linewidth enhancement factor (~2) at a similar operating point. The strong dependence of the linewidth enhancement factor on the photon density is due to the enhancement of the gain saturation with carrier density, which is related to the occurrence of inhomogeneous broadening and spectral hole burning in QDs [21].

2.6.3 Modulation Response of the Injection-Locked QD FP Device: Experimental Findings

Once the free-running operating parameters of the slave laser are fully characterized, the extracted free-running values can be used to aid the injection-locked simulations as similarly described in section (2.5.3). Figure (2.21) illustrates the spectral responses of the free-running and injection-locked case at zero detuning. The free-running spectra indicate a FP mode separation of ~135 GHz. The slave laser was DC biased at 5 mA and maintained at room temperature throughout the measurement. The master laser was pumped at 18.2 mA and thermally-tuned to 21.6°C where it is peak locked to the FP mode centered at 1312.33 nm. The SMSR was measured to range between 30 to 55dB for the investigated injection strengths at different detuning conditions. Note that choosing an appropriate value for the SMSR is critical as it defines the locking boundary and assures the stable-locking condition throughout the experiment.

Figures (2.22) through (2.27) show a complete experimental modulation response characterization of the injection-locked QD laser for various frequency detuning conditions and injection strengths. Each graph includes the same free-running modulation response along with different injection-locked responses for specific positive and negative frequency detuning cases. Choosing the specific cases was based on the highest available modulation bandwidth on each positive and negative frequency detuning side for a given injection strength scenario. For all of these cases, the slave laser bias current was kept constant at 5 mA and emits a total output power of 0.79 mW. The pump current on the DFB master laser was adjusted to obtain the desired external power ratios, P_{ext}, of 7, 12, and 15dB which respectively correspond to 3.9, 11.5, and 24.4 mW available
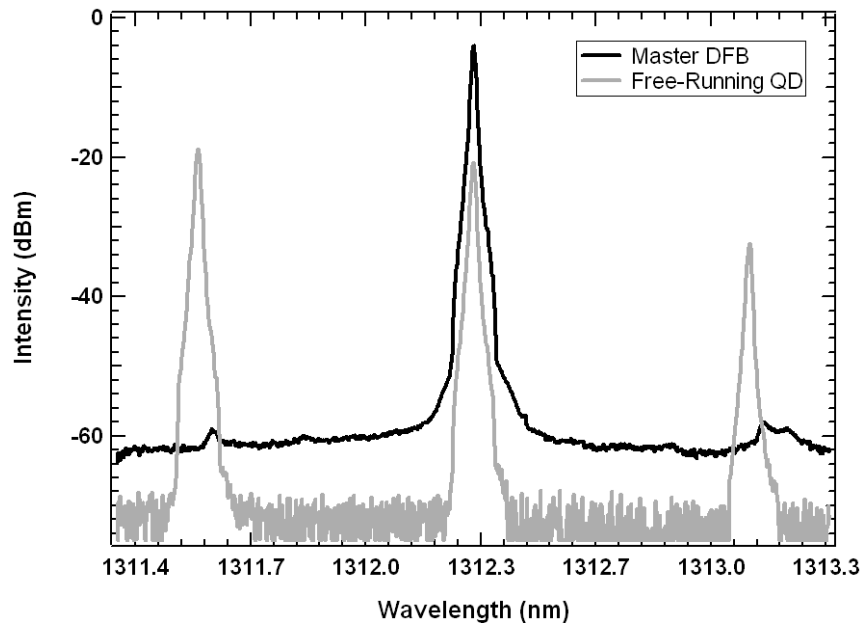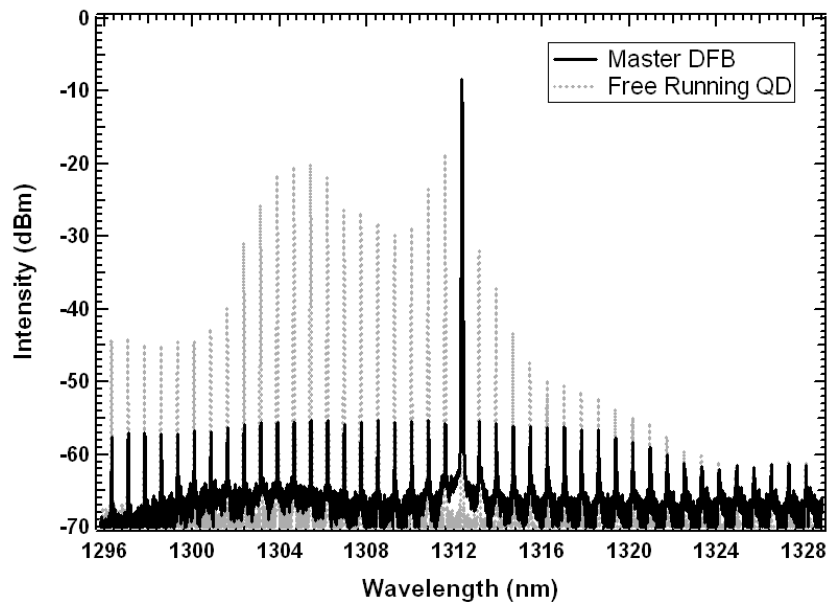
Figure (2.21) Free-running and injection-locked spectra of the QD FP laser under zero detuning condition at 1312.33 nm, indicating a >30dB SMSR between the locked mode and side FP modes. Top and bottom figures illustrate a 30 nm and 2 nm span of the optical spectra, respectively.
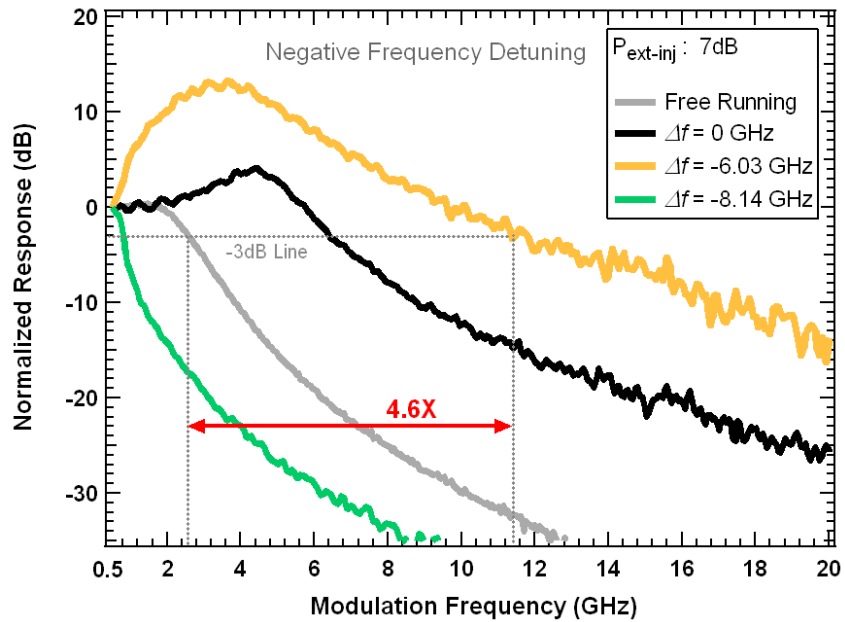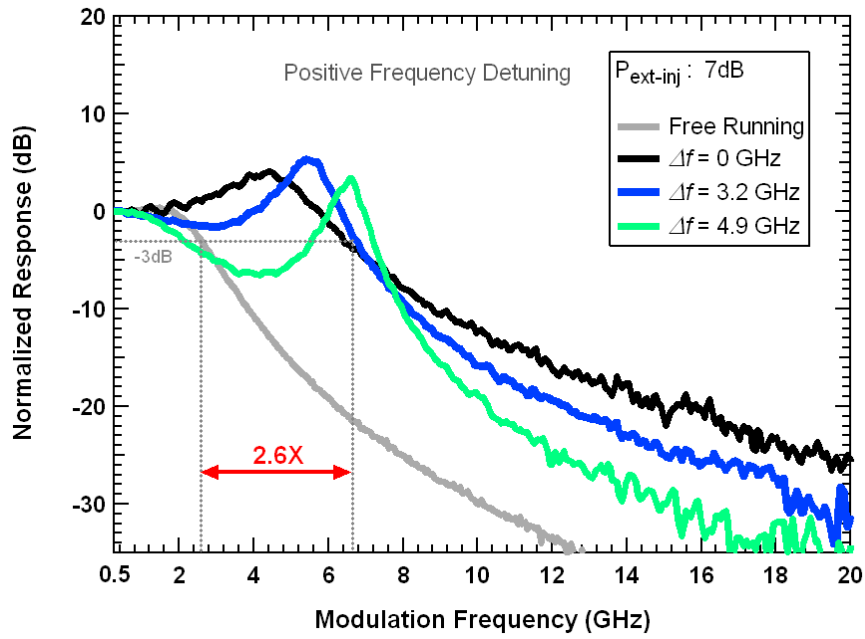
Figure (2.22) Normalized modulation responses under positive (top) and negative (bottom) frequency detuning conditions for $P_{ext-inj}$=7dB, indicating 2.6X and 4.6X improvement in 3-dB bandwidth compared to the free-running case.
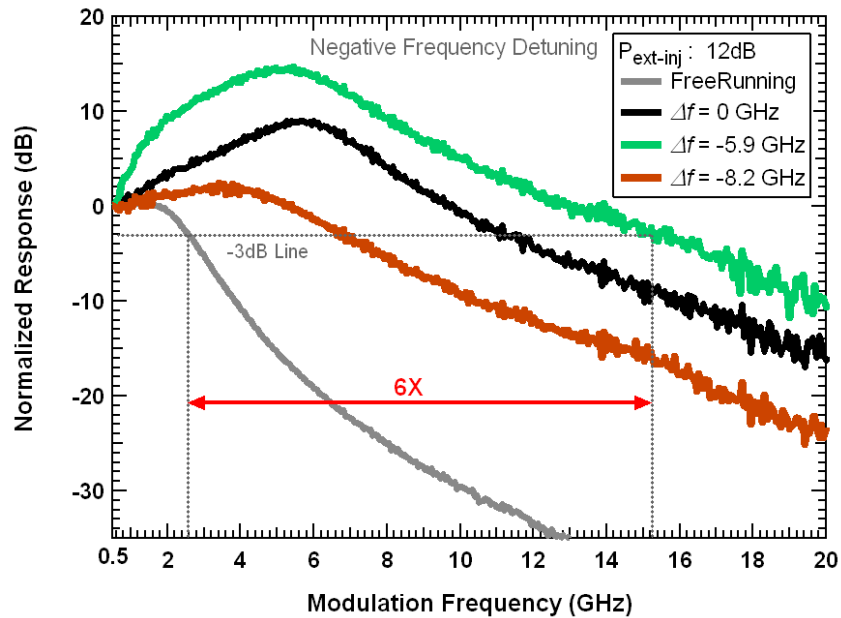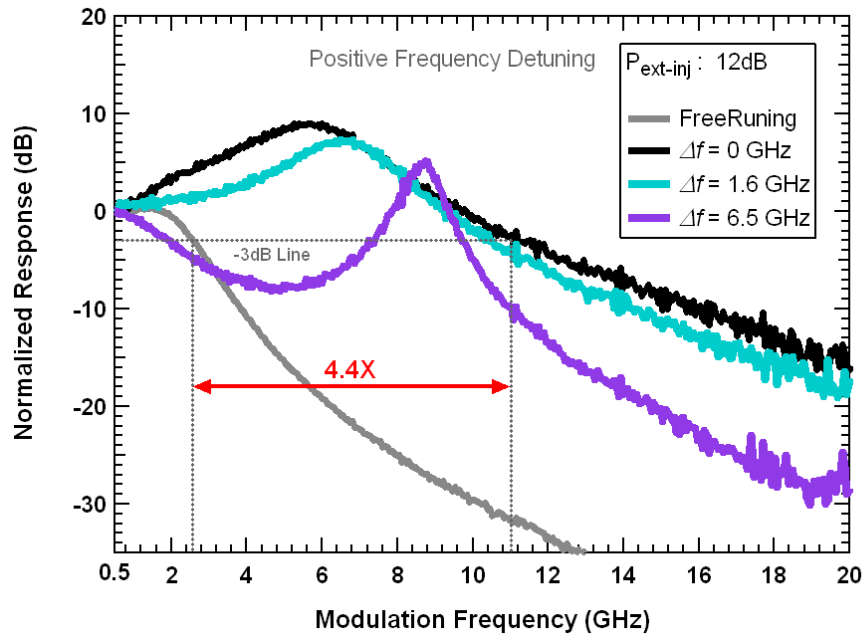
Figure (2.23) Normalized modulation responses under positive (top) and negative (bottom) frequency detuning conditions for $P_{ext-inj}=12dB$, indicating 4.4X and 6X improvement in 3-dB bandwidth compared to the free-running case.
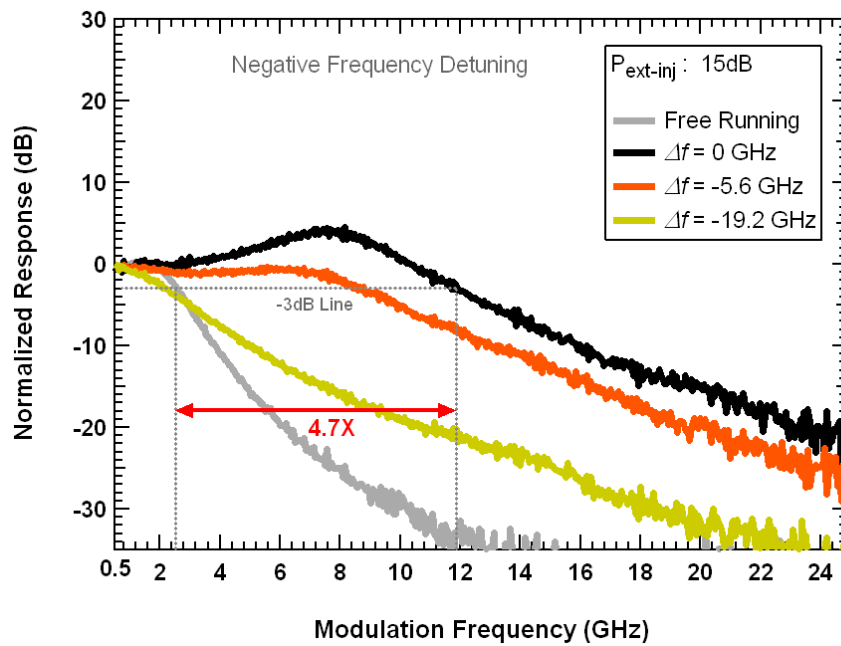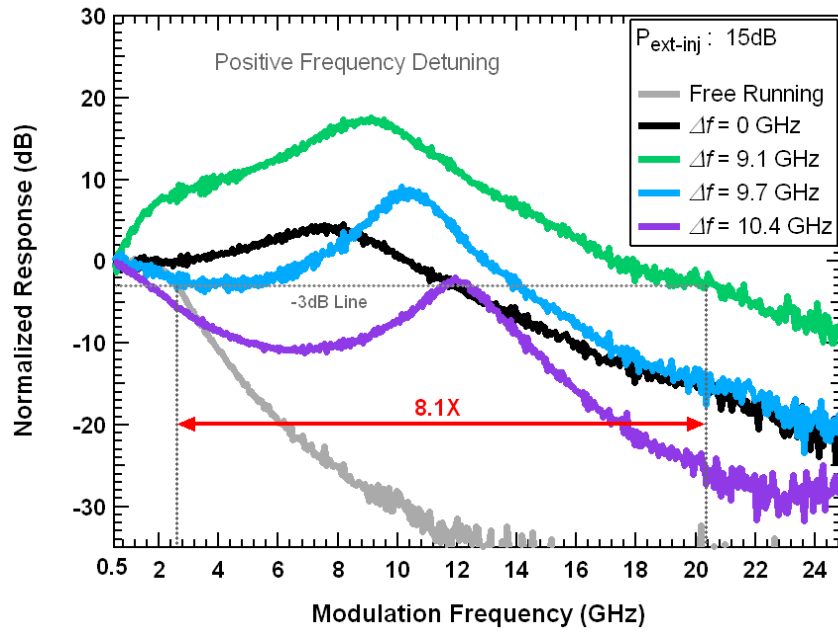
Figure (2.24) Normalized modulation responses under positive (top) and negative (bottom) frequency detuning conditions for $P_{ext-inj}$=15dB, indicating 8.1X and 4.7X improvement in 3-dB bandwidth, respectively, compared to the free-running case.

injected powers at the slave facet. Constant bias on the slave laser while varying the injected power provides a clear comparison for each individual case to examine the effect of increased injection strengths on the overall resonance frequency and consequently maximum available bandwidth.

Figures (2.22) to (2.24) represent the normalized modulation responses for the free-running laser along with zero, positive and negative detuning injection-locked responses for external power ratios of 7dB, 12dB, and 15dB. For each value of injection strength, the maximum achievable bandwidth enhancement is measured compare to the free-running case.

The positive frequency detuning cases (top graphs) indicate a bandwidth enhancement of 2.6, 4.4, and 8.1 times, and the negative frequency detuning cases (bottom graphs) indicate a 3-dB bandwidth enhancement of 4.6, 6, and 4.7 times compared to the free-running case. In Figures (2.22) through (2.24), the external power ratio is set to increase from 7dB to 15dB. The maximum 3-dB bandwidth was observed at the positive frequency detuning side with an 8.1X improvement compared to the free-running case. It is important to note that on the positive detuning side, the maximum bandwidth occurs at detuning cases that have a unique shape in the modulation response that were not seen for the QDash laser. This novel shape is characteristic of situations that have a small zero, Z, in the numerator of the modulation response function (2.31). This small Z is enabled by the relatively small linewidth enhancement factor in the QD laser. Further positive frequency detuning cases suffer from the undesired pre-resonance dip between the DC value and the enhanced resonance. The maximum bandwidth for the P_{ext}= 7 and 12dB cases occurred at negative frequency detuning side where the responses

103
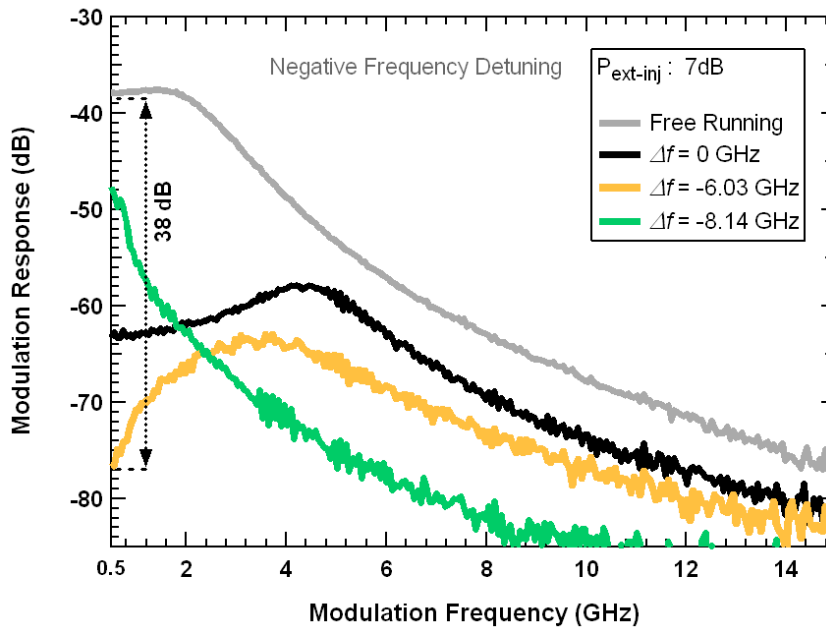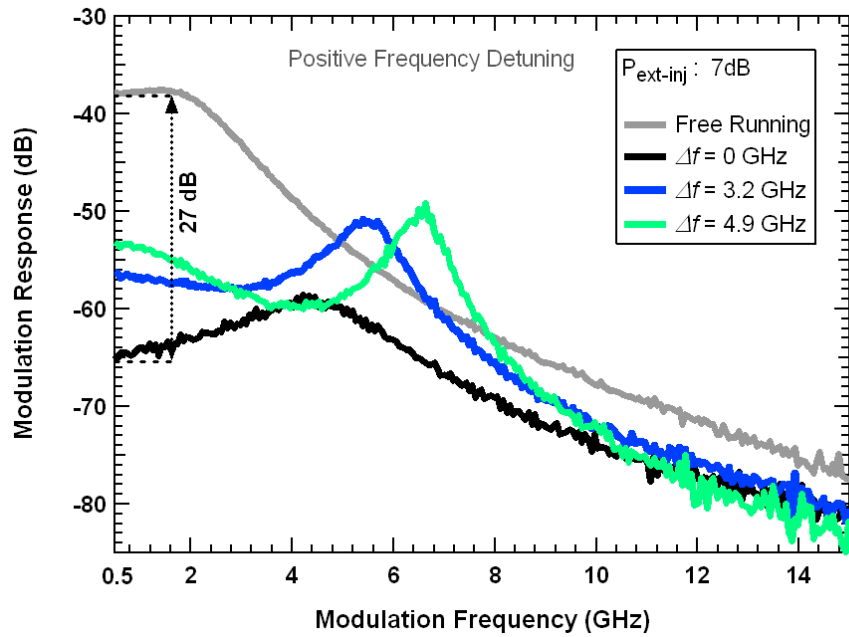
Figure (2.25) Modulation responses under positive and negative frequency detuning conditions for $P_{ext-inj}$=7dB, indicating the modulation efficiency decreases by 27dB and 38dB, respectively, compared to the free-running case.
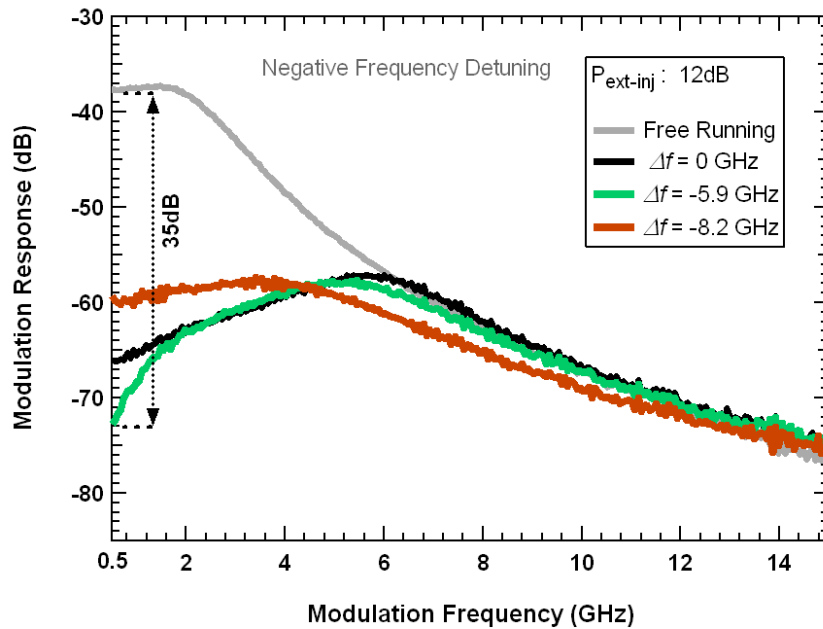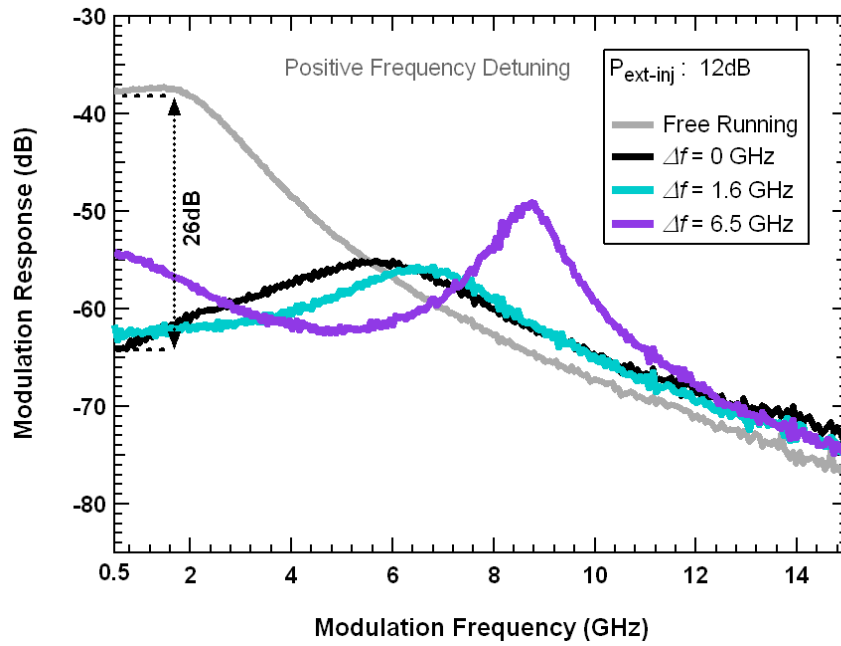
Figure (2.26) Modulation responses under positive and negative frequency detuning conditions for $P_{ext-inj}=12dB$, indicating the modulation efficiency decreases by 26dB and 35dB, respectively, compared to the free-running case.
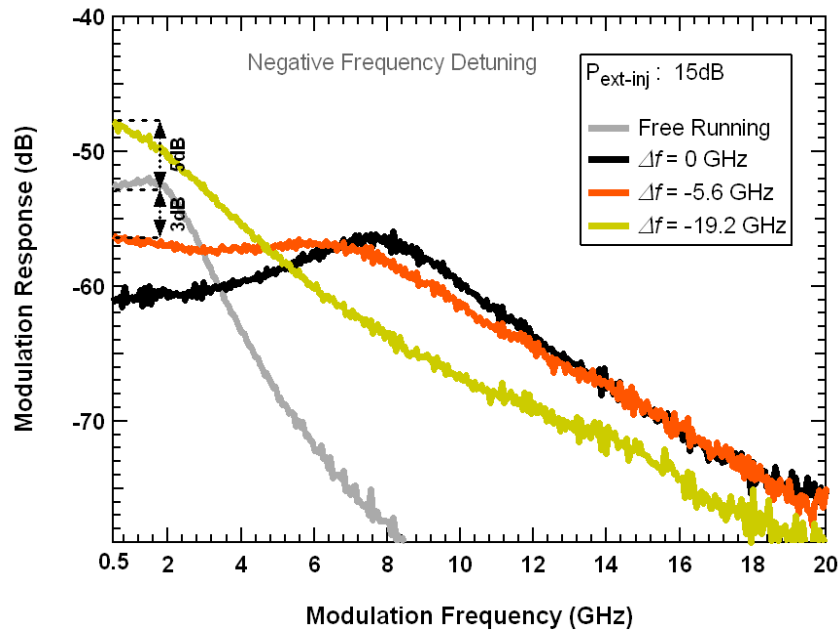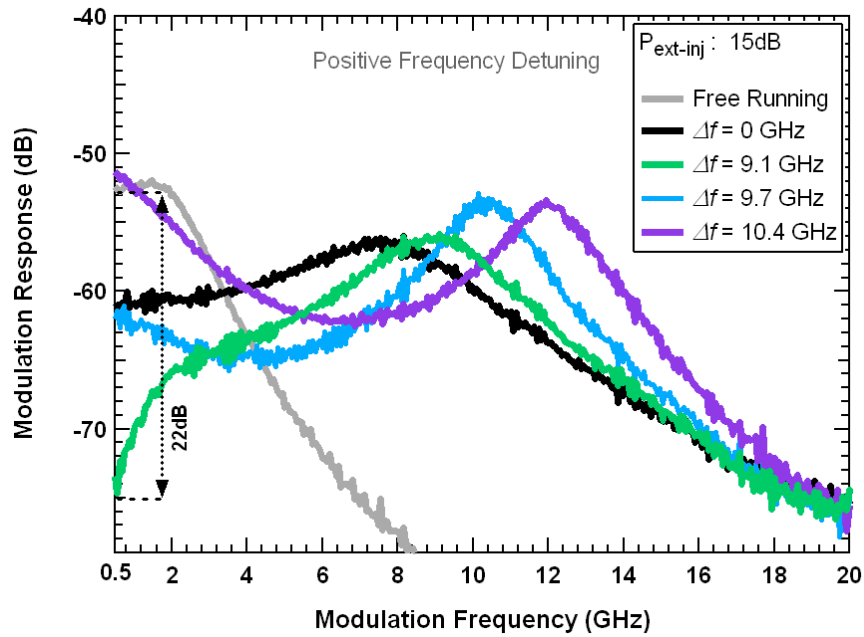
Figure (2.27) Modulation responses under positive (top) and negative (bottom) frequency detuning conditions for $P_{ext-inj}$=15dB, indicating the modulation efficiency decreases by 3dB, and slight increase by 5dB, respectively, compare to the free-running case.

are usually more damped due to an increase in the slave's field enhancement with optical injection.

The specific responses yielding the highest bandwidths at each external power ratio are uniquely characterized by a rapid low frequency rise (corresponding to the normalized cases) and a slower high frequency roll-off compared to the free-running and other detuning cases. These responses are shown in Figures (2.22) through (2.24) and correspond to Δf = -6.03 GHz with P_{ext}= 7dB, Δf = -5.9 GHz with P_{ext}= 12dB, and at Δf = 9.1 GHz detuning cases with P_{ext}= 15dB.

Figures (2.25) through (2.27) illustrate the corresponding un-normalized modulation responses for the same cases shown in Figures (2.22) through (2.24). These figures analyze the decrease in the modulation efficiency of the injection-locked responses with the highest bandwidth improvement compared to the free-running case. As shown in these figures, the highest modulation efficiency drops are for the detuning cases with maximum bandwidth in the normalized response. A 5dB improvement in the modulation efficiency compared to the free-running was observed in the QD laser's highly damped response when Δf = -19.2 GHz and P_{ext}= 15dB (Figure (2.27), bottom graph). This detuning case has relatively higher gain at the expense of very low bandwidth. Also, due to the lack of resonance peak for this case, this set of conditions would yield a linear response [10]. This specific case of detuning is usually suitable for low bandwidth applications that require higher gain (low link loss) and higher linearity [10]. As shown in both positive and negative frequency detuning cases, the low frequency roll-off decreases for the cases with higher injection strength. In Figure (2.27), the Δf = 9.1 GHz detuning case with 8.1X improvement in 3-dB bandwidth experiences a
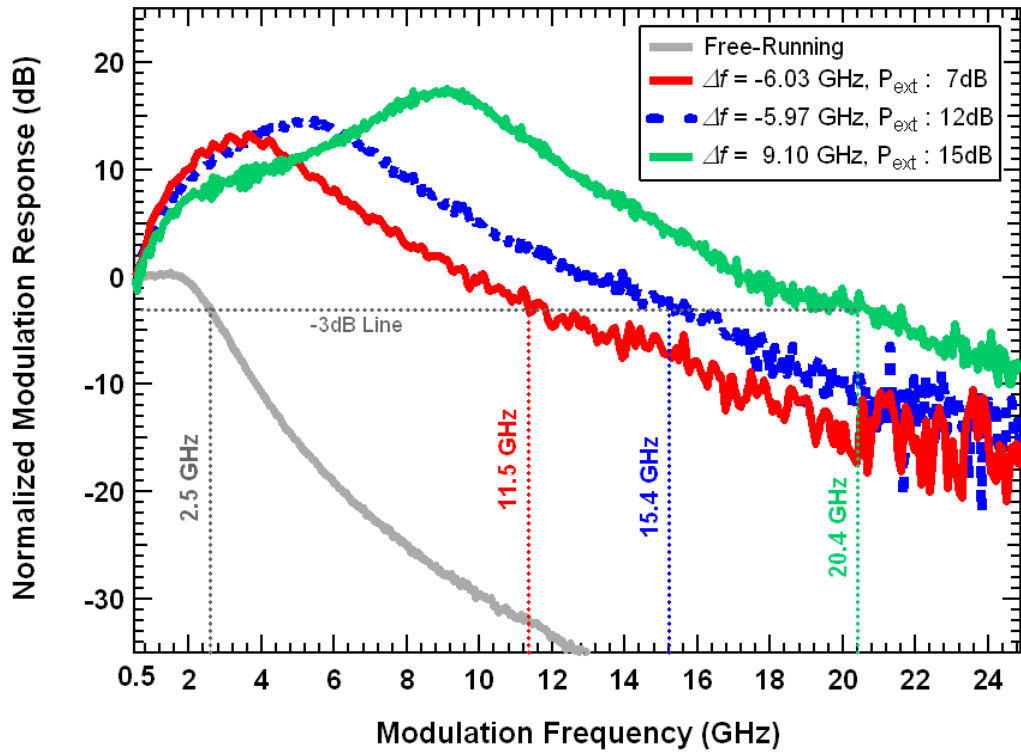
Figure (2.28) Normalized modulation responses of the free-running and the injection-locked QD laser under various frequency detuning conditions and injection strengths. The slave 3-dB bandwidth was found to be 2.5 GHz when it is biased at 5mA, and the maximum injection-locked 3-dB bandwidth with the same slave bias current and external injected power ratios of P_{ext}= 7dB, 12dB and 15dB were found to be 11.5 GHz, 15.4GHz and 20.4GHz respectively.

22dB drop in modulation efficiency. However, this case is still 5dB better than the zero detuning case at P_{ext}= 7dB with only 2.6X improvement in 3-dB bandwidth. The physical origin of this modulation efficiency drop is described later in this chapter.

Figure (2.28) compares the normalized injection-locked modulation responses with maximum 3-dB bandwidth for different injection strengths. With a 22dB drop in modulation efficiency, the maximum 3-dB bandwidth of 20.4 GHz was observed at Δf = 9.1 GHz. This is an 8-fold increase in bandwidth compared to the free-running case. To

the best of our knowledge this is the highest modulation bandwidth ever reported for an edge emitting injection-locked QD FP laser operating at 1.31μm and room temperature.

2.6.4 Extracting the Operating Parameters of the Injection-Locked QD FP Device

For a better understanding of the origin of the unique modulation responses observed in this experiment, it is beneficial to characterize the injection-locked cases with the highest modulation bandwidth by extracting the key operating parameters associated with each case. Knowing these parameters can be further used to predict the ideal operating conditions in order to optimize the modulation characteristics of a nanostructure semiconductor laser under optical injection.

Similar to the simulations performed for the QDash FP device, the theoretical modulation response model described in section (2.2.4) can be used to lease-squares fit the experimental data collected from the injection-locked QD FP laser system in order to extract the key parameters of the coupled system. By reducing the number of fitting parameters through known free-running fitting terms and applying a proper constraint on the remaining injection-locking terms, the operating parameters of the coupled system can be measured. These parameters include the linewidth enhancement factor, α, the slave-master phase offset ϕ_0, the maximum injection strength η_0, and the field enhancement factor R_{FE}. The slave free-running terms including the free-running relaxation oscillation frequency f_r, free-running damping rate γ_{fr}, and inverse differential carrier lifetime γ_N were extracted in section (2.6.2) by performing a least-squares fit on the free-running modulation responses using (2.34). At a slave bias level of 5mA, these free-running parameters were found to be f_r= 1.9 GHz, γ_{fr}= 10 GHz and γ_N= 9 GHz, as

shown in Figure (2.17), (2.18). The value of the parasitic roll-off for the free-running case at 5 mA was measured to be γ_c=67 GHz. These parameters were kept constant during the simulations except for the parasitic roll-off γ_c which was allowed to vary in an acceptable range to explain the slow roll-off observed in the injection-locked responses. As described in section (2.5.4), since there are many possible solutions that can fit the experimental data, appropriate constraints are applied to the remaining fitting terms.

The constraints on ϕ_0 are based on the allowed locking range through the threshold condition according to the phase boundaries for the extreme detuning cases, which indicates that the phase offset can vary from $-\pi/2$ for the positive frequency detuning edge to $\cot^{-1}(\alpha)$ for the negative frequency detuning edge. The phase condition at the positive frequency detuning edge stipulates that the value of R_{FE} should be equal to 1 since the slave's steady-state field matches the free-running field due to the 90 degree phase offset between the master and slave. The field enhancement factor, R_{FE}, is allowed to increase beyond 1 as the detuning frequency is shifted from the positive edge.

The value for η_0 can be directly calculated using (2.36) for a given external power ratio and be constrained tightly during the simulations. Using (2.36) and knowing that the emitting facet reflectivity is 80%, the measured average group index of the active region is 3.52, and a coupling efficiency of 44%, η_0 was calculated to be 47.5 GHz, 81.3 GHz, and 116.5 GHz for the external power ratios of P_{ext} = 7dB, 12dB, and 15dB, respectively. Since the coupling efficiency was carefully maintained during the experiment, the maximum injection strength was held constant during the simulations for each case. One important constraint in the coupled system is that physically the threshold gain shift, γ_{th}, cannot exceed the photon decay rate (γ_P=$1/\tau_p$), which in this QD device is ~75 GHz.

Based on the variation of the linewidth enhancement factor with power in the QD device (shown in Figure (2.20)), this value is allowed to fluctuate with the variation of detuning and injection strengths. Using a bias current of 5mA under free-running conditions, the linewidth enhancement factor was measured to be ~2 by using the injection locking method. In the case of strong injection, the slave's linewidth enhancement factor is expected to vary significantly with both detuning and injected power due to the strong dependence on the power and carrier density seen in a QD device [21].

2.6.5 Curve-Fitting Results

Based on the least-squares curve-fitting strategy described above and using (2.23) through (2.31), the injection-locked modulation responses with the highest bandwidth at P_{ext} = 7dB, 12dB and 15dB were successfully simulated, and the fitting results are shown in Figure (2.29). The associated error analysis is summarized in Table (2.3). The error analysis was based on a one standard deviation confidence interval calculated for α, ϕ_0, R_{FE} , and γ_{th}. The error for the extracted free-running values was negligible ($< 7\%$).

The extracted values for α shown in Table (2.3) indicate that the linewidth enhancement factor varies with frequency detuning and injection strength within the experimental error range. These results showed that the slave's linewidth enhancement factor decreases significantly from a free-running value of ~2 to -0.16 for an increased power ratio up to P_{ext} = 15dB. This trend is consistent with the results shown in Figure (2.20), which indicates a variation of linewidth enhancement factor with power along

111
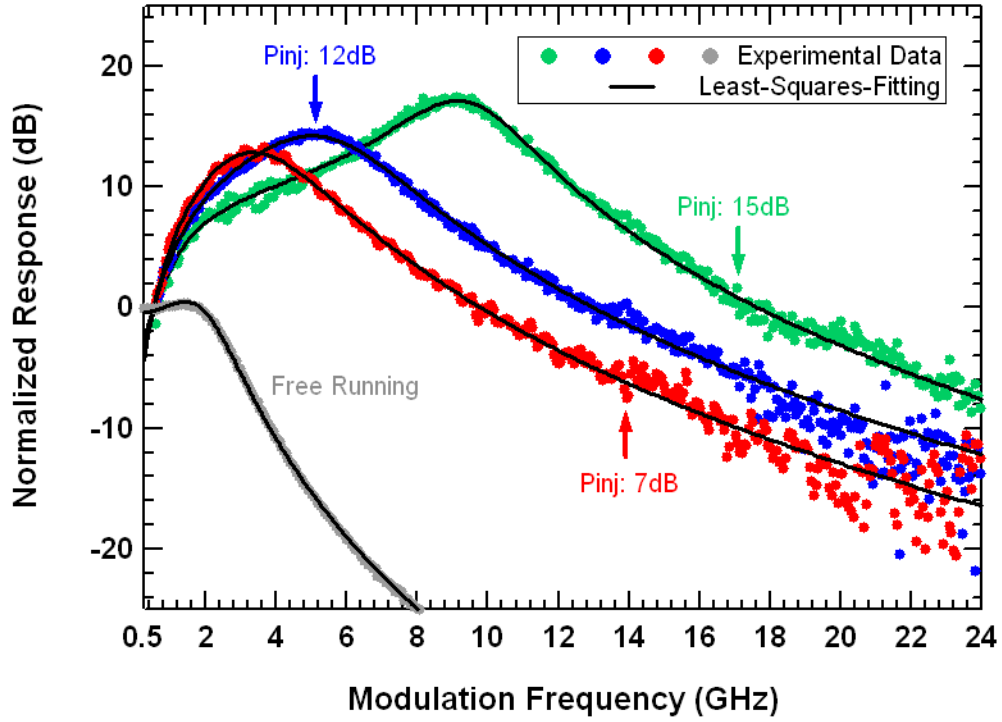
Figure (2.29) Least-squares fit results of the normalized modulation response of the free-running and the injection-locked QD laser for P_{ext}= 7dB and Δf = -6.03 GHz, P_{ext}= 12dB and Δf = -5.97 GHz, P_{ext}= 15dB and Δf = 9.1 GHz.

TABLE (2.3)

Extracted operating parameters for the injection-locked conditions shown in Figure (2.29).

P_{ext} (dB)	Δf (GHz)	η_0 (GHz)	α	ϕ_0 (rad)	R_{FE}	γ_{th} (GHz)
7	-6.03	47.54	**0.521** ±0.8	**1.010** ±0.2	**1.41** ±0.3	**35.93** ±0.4
12	-5.97	80.04	**0.384** ±0.5	**1.133** ±0.3	**2.29** ±0.7	**29.75** ±2.6
15	9.1	116.5	**-0.16** ±0.9	**-1.323** ±0.7	**2.06** ±0.9	**27.7** ±5.7

with the existence of a free-running value as low as 0.6. Near-zero or even negative material linewidth enhancement factors have been previously reported in QD material systems [28]-[30]. Due to the delta function-like density of states in QDs and their random size distribution, the QD gain spectrum is expected to be fairly symmetric around the gain peak. As a result, QD material systems should yield a very small linewidth enhancement factor. Based on intraband carrier dynamic analysis and the complex susceptibility, a negative value for the linewidth enhancement factor was found to be possible in QDs if the effect of size dispersion (inhomogeneous broadening) is sufficiently small [28]. This finding is very important since it indicates that a slave laser's linewidth enhancement factor can be reduced to near zero values (even to negative) in an injection-locked QD laser system under optical injection by increasing the injection strength and/or adjusting the frequency detuning. However, noting the error bars on α in Table (2.3), the modulation response can only be used as a rough indicator that the α is small. Chapter 3 discusses the manipulation of a nanostructure's linewidth enhancement factor with optical injection in greater detail and describes how to measure it more accurately.

The extracted values for the phase shift ϕ_0, are consistent with the theory stating that the steady-state phase offset ranges from $-\pi/2$ at the positive frequency detuning edge to $\cot^{-1}(\alpha)$ at the negative frequency detuning edge. The maximum phase values at the boundaries are used to verify the validity of the extracted values for each case. Based on the extracted values of α, the phase boundaries at negative frequency detuning for $P_{ext} =$ 7, 12 dB are calculated to be 1.1, and 1.204 rad, respectively and for the $P_{ext} = 15$ dB case is equal to -1.571 rad (or $-\pi/2$).

Based on the extracted values for ϕ_0, R_{FE}, η_0, the α and γ_{th}, are calculated for each case. The calculated values for γ_{th} presented in Table (2.3) are relatively similar to each other except for the positive frequency detuning case. For this positive detuning case, there is a slight decrease at higher injection strength due to the out of phase coupling condition between the injected and free-running fields.

As seen in Table (2.3), the fitting results for R_{FE} show a higher value at increased negative frequency detuning and injection strength. This trend corresponds to theory, which describes an increase in the slave laser steady-state field magnitude under negative frequency detuning conditions with increased injection strength. It is also important to verify the validity of the extracted value of R_{FE} for each case, since the theory states it cannot exceed the ratio of the external field amplitude measured at the slave's emitting facet, $R_{FE} \leq (\eta_c \times R_{ext})^{1/2}$. The maximum achievable field enhancement factor for external master powers of 7, 12, and 15 dB are 1.5, 2.5, and 3.6, respectively.

Extracted results for the parasitic roll-off decay time, τ_c, show a significant decrease to ~ 6 ps in the decay rate compared to the 15 ps that was calculated for the free-running case. This decrease is probably due to the device heating as a result of strong optical injection. As indicated in Figure (2.29), the slope of the high frequency roll-off is noticeably modified under optical injection when compared to the free-running case. The decrease in severity of the roll-off contributes to the 3-dB modulation bandwidth improvement, generating the 8-fold improvement over the free-running value. Quantitatively, this roll-off is measured to be approximately 20dB per decade under the optical injection case, compared with a 35dB per decade measured under free-running operation.

The extracted injection-locking parameters given in Table (2.3) can be used to explain the low frequency roll off observed in the unique modulation responses shown in Figure (2.29). Considering the modulation response function given in (2.31), at small modulation frequencies, as $\omega \to 0$, the absolute transfer function can be approximated as follows:

$$H(\omega \to 0) = \frac{\Delta A}{\Delta J} \approx \frac{M(-Z)}{C} \qquad (2.38)$$

As seen in (2.38), a small Z value and/or large C term will increase the low frequency roll-off near DC. Based on the relation between the phase, linewidth enhancement factor, and injection strength given in (2.30), the zero of the function (Z) can vary between 0 to $-(\eta_0/R_{FE})\alpha$ from the negative to positive detuning boundaries. Considering the modulation response function given in (2.31), a smaller Z value is generally desired since it reduces the sensitivity of the denominator and causes the numerator to scale roughly with the modulation frequency. Now to explain the observed low frequency roll off, lets consider the modulation responses of the zero detuning and positive detuning case at $\Delta f = 9.1$ GHz for $P_{ext} = 15$dB as shown in Figure (2.27). The zero detuning modulation response at $P_{ext} = 15$dB is separately simulated using (2.31) and the operating parameters are extracted for this case. Using (2.29) and (2.30), the C and Z terms are calculated for the aforementioned detuning cases and the results are presented in Table (2.4). As shown in Table (2.4), both detuning cases have similar C values but the absolute value of Z is much smaller for the $\Delta f = 9.1$ GHz detuning compared to the zero detuning case. This explains the 22 dB drop seen between the free-running and $\Delta f = 9.1$ GHz detuning case. In contrast, only an 8dB drop is seen between the free-running and zero detuning case as

115

TABLE (2.4)

Calculated *C* and *Z* terms at $\Delta f = 9.1$ GHz and $\Delta f = 0$ GHz for $P_{ext} = 15$dB.

Δf (GHz)	$(C)^{1/3}$ (GHz)	Z (GHz)
0	5.67	-2.98
9.1	5.63	-0.81

shown in Figure (2.27). The small *Z* value for the $\Delta f = 9.1$ GHz detuning case corresponds to a combination of a small linewidth enhancement factor along with the unique steady-state phase condition where $\alpha sin\phi_0$ offsets the $cos\phi_0$ term in equation (2.17). A similar approach can be used to explain the drop in the low frequency response at $P_{ext} = 7$ dB and 12 dB. The $P_{ext} = 7$ dB has the highest low frequency roll-off compared to the 12 dB and 15 dB cases since the *Z* value is relatively small at this case due to a lower injection strength.

2.7 Chapter 2 Summary

This chapter experimentally and theoretically analyzed the high-speed modulation characteristics of injection-locked QDash and QD nanostructure lasers. Using a novel modulation response function that describes the dynamic properties of an injection-locked system, the key operating parameters of both nanostructure laser systems were directly extracted by performing a least-squares-fit of the experimental data. The extracted values were found to be in a good agreement with theory which proved that the

116

response model is a reliable method to extract the key operating parameters of the observed response in the microwave domain. It is also found that the slave laser's linewidth enhancement factor has a significant impact on the modulation response of injection-locked nanostructures due to the unique carrier dynamics in these material systems. For an injection-locked QDash laser, it is found that the observed pre-resonance dip in the modulation response can be virtually eliminated at higher α values by increasing the slave's bias current or reducing the device temperature. In an injection-locked QD laser the linewidth enhancement factor led to a unique modulation response shape that takes advantage of the enhancement of the resonance frequency achieved through optical injection without experiencing the pre-resonance dip that significantly limits the useful bandwidth in the conventional injection-locked response. Lastly, comparing the extracted values of the linewidth enhancement factor under injection-locking to the measured free-running values identify that the slave's linewidth enhancement factor can significantly vary because of the threshold gain shift in both QDash and QD lasers under optical injection. The magnitude of this variation is found to scale with the injection strength and is the highest at the negative frequency edge where the threshold gain shift is significant. This finding is very important since it indicates that by changing the frequency detuning and/or varying the optical injection strength, the slave linewidth enhancement factor can be manipulated in an injection-locked nanostructure laser. In chapter 3, the manipulation of QDash linewidth enhancement factor at zero detuning and under various optical injection strengths is investigated.

2.8   Chapter 2 References

[1]   F. Mogensen, H. Olesen, and G. Jacobsen, "FM noise suppression and linewidth reduction in an injection-locked semiconductor laser," *Electronics Letters*, Vol. 21, No. (16), pp. 696-697, (1985).

[2]   N. Schunk, K. Petermann, "Noise Analysis of Injection-Locked Semiconductor Injection Lasers," *IEEE Journal of Quantum Electronics*, Vol. 22, No. (5), pp. 642-650, (1986).

[3]   I. Petitbon, P. Gallion, G. Debarge, C. Ghabran, "Locking Bandwidth and Relaxation Oscillation of an Injection-Locked Semiconductor Laser," *IEEE Journal of Quantum Electronics*, Vol. 24, No. (2), pp. 148-154, (1988).

[4]   T. B. Simpson, J. M. Liu, A. Gavrielides, "Bandwidth Enhancement and Broadband Noise Reduction in Injection-Locked Semiconductor Lasers," *IEEE Photonics Technology Letters,* Vol. 7, No. (7), pp. 709-711, (1995).

[5]   T. B. Simpson, J. M. Liu, A. Gavrielides, "Small-Signal Analysis of Modulation Characteristics in a Semiconductor Laser Subject to Strong Optical Injection," *IEEE Journal of Quantum Electronics*, Vol. 32, No. (8), pp. 1465-1468, (1996).

[6]   T. B. Simpson, J. M. Liu, "Enhanced Modulation Bandwidth in Injection-Locked Semiconductor Lasers," *IEEE Photonics Technology Letters*, Vol. 9, No. (10), pp. 1322-1324, (1997).

[7]   J. M. Liu, H. F. Chen, X. J. Meng, T. B. Simpson, "Modulation Bandwidth, Noise, and Stability of a Semiconductor Laser Subject to Strong Injection Locking," *IEEE Photonics Technology Letters*, Vol. 9, No. (10), pp. 1325-1327, (1997).

[8]   A. Murakami, K. Kawashima, and K. Atsuki, "Cavity resonance shift and bandwidth enhancement in semiconductor lasers with strong light injection," *IEEE Journal of Quantum Electronics*, Vol. 39, No. (10), pp. 1196-1204, (2003).

[9]   L. Chrostowski, B. Faraji, W. Hofmann, M. C. Amann, S. Wieczorek, W. W. Chow, "40 GHz Bandwidth and 64 GHz Resonance Frequency in Injection-Locked 1.55 µm VCSELs," *IEEE Journal of Selected Topics in Quantum Electronics*, Vol. 13, No. (5), pp. 1200-1208 , (2007).

[10]   E. K. Lau, H. K. Sung, M. C. Wu, "Frequency Response Enhancement of Optical Injection Locked Lasers," *IEEE Journal of Quantum Electronics*, Vol. 44, No. (1), pp. 90-99 , (2008).

[11]   E. K. Lau, X. Zhao, H. K. Sung, D. Parekh, C. Chang-Hasnain, M. C. Wu, "Strong optical injection-locked semiconductor lasers demonstrating >100-GHz resonance frequencies and 80-GHz intrinsic bandwidths," *Optics Express*, Vol. 16, No. (9), pp. 6609-6618, (2008).

[12]   R. Lang, "Injection locking properties of a semiconductor laser," *IEEE Journal of Quantum Electronics*, Vol. 18, No. (6), pp. 976-983, (1982).

[13]   F. Mogensen, H. Olesen, and G. Jacobsen, "Locking conditions and stability properties for a semiconductor laser with external light injection," *IEEE Journal of Quantum Electronics*, Vol. 21, No. (7), pp. 784-793, (1985).

[14]   C. H. Henry, N. A. Olsson, and N. K. Dutta, "Locking range and stability of injection locked 1.54 µm InGaAsP semiconductor lasers," *IEEE Journal of Quantum Electronics*, Vol. 21, No. (8), pp. 1152-1156, (1985).

[15]   T. B. Simpson, J. M. Liu, K. F. Huang, K. Tai, C. M. Clayton, A. Gavrielides, and V. Kovanis, "Cavity enhancement of resonant frequencies in semiconductor lasers subject to optical injection," *Physical Review A*, Vol. 52, No. (6), pp. R4348-51, (1995).

[16]   P. Bhattacharya, D. Klotzkin, O. Qasaimeh, W. D. Zhou, S. Krishna, and D. H. Zhu, "High-speed modulation and switching characteristics of In(Ga)As-Al(Ga)As self-organized quantum-dot lasers," *IEEE Journal of Selected Topics in Quantum Electronics*, Vol. 6, No. (3), pp. 426-438, (2000).

[17]   R. Olshansky, P. Hill, V. Lanzisera, W. Powazinik, "Frequency response of 1.3μm InGaAsP high speed semiconductor laser," *IEEE Journal of Quantum Electronics*, Vol. 23, No. (9), pp. 1410-1418, (1987).

[18]   R. H. Wang, A. Stintz, P. M. Varangis, T. C. Newell, H. Li, K. J. Malloy, and L. F. Lester, "Room-temperature operation of InAs quantum-dash lasers on InP (001)," *IEEE Photonics Technology Letters*, Vol. 13, No. (8), pp. 767-769, (2001).

[19]   C. –Y. Lin, Y. –C. Xin, Y. Li, F. L. Chiragh, and L. F. Lester, "Cavity design and characteristics of monolithic long-wavelength InAs/InP quantum dash passively mode-locked lasers," *Optics Express*, Vol. 17, No. (22), pp. 19739-19748, (2009).

[20]   J. E. Bowers, "High speed semiconductor laser design and performance," *Solid-State Electronics,* Vol. 30, No. (1), pp. 1-11, (1987).

[21]   H. Su, L. F. Lester, "Dynamic properties of quantum dot distributed feed back lasers: high speed, linewidth and chirp," *Journal of Physics D: Applied Physics*, Vol. 38, No. (13), pp. 2112-2118, (2005).

[22] F. Grillot, N. A. Naderi, M. Pochet, C.-Y. Lin, and L. F. Lester, "Variation of the feedback sensitivity in a 1.55-µm InAs/InP quantum dash Fabry-Perot semiconductor laser," *Applied Physics Letters,* Vol. 93, No. (19), pp. 191108, (2008).

[23] F. Grillot, B. Dagens, J. G. Provost, H. Su, L. F. Lester, "Gain Compression and Above Threshold Linewidth Enhancement Factor in 1.3-µm InAs-GaAs Quantum-Dot Lasers," *IEEE Journal of Quantum Electronics*, Vol. 44, No. (10), pp. 946-951, (2008).

[24] E. K. Lau, "High-Speed Modulation of Optical Injection-Locked Semiconductor Lasers," *PhD Dissertation*, UC Berkeley, Dec 2006.

[25] G. Liu, X. Jin, S. L. Chuang, "Measurement of Linewidth Enhancement Factor of Semiconductor Lasers Using an Injection-Locking Technique," *IEEE Photonics Technology Letters*, Vol. 13, No. (5), pp. 430-432, (2001).

[26] C. Dziak, A. J. Moscho, Y. Li, M. Fanto, V. Kovanis, J. Malowicki, L. F. Lester, "Measurement of the Linewidth Enhancement Factor of a 1550-nm Injection-Locked Quantum Dash Laser," *in Proceedings of IEEE Lasers Electro-Optics Society Conference*, pp. 433–434, (2007).

[27] G. P. Agrawal, "Spectral hole-burning and gain saturation in semiconductor lasers: strong-signal theory," *Journal of Applied Physics*, Vol. 63, No. (4), pp. 1232-1235, (1988).

[28] P. M. Smowton, E. J. Pearce, H. C. Schneider, W. W. Chow, and M. Hopkinson, "Filamentation and linewidth enhancement factor in InGaAs quantum dot lasers," *Applied Physics Letters,* Vol. 81, No. (17), pp. 3251-3253, (2002).

[29]　R. R. Alexander, D. Childs, H. Agarwal, K. M. Groom, H. Y. Liu, M. Hopkinson, R. A. Hogg, "Zero and Controllable Linewidth Enhancement Factor in p-Doped 1.3μm Quantum Dot Lasers", *Japanese Journal of Applied Physics*, Vol. 46, No. (4B), pp. 2421-2423, (2007).

[30]　P. K. Kondratko, S. L. Chuang, G. Walter, T. Chung, and N. Holonyak, "Observation of zero and negative linewidth-enhancement factor in tunneling injection quantum-well-dot laser," *in Proceedings of Conference on Lasers and Electro-Optics*, pp. CThI1, (2003).

Chapter 3

Manipulation of the Linewidth Enhancement Factor in QDash Nanostructure Laser under Strong Optical Injection

3.1 Introduction

Two key figures of merit in high-speed performance of directly modulated semiconductor lasers are their limited modulation bandwidth and relatively high linewidth enhancement factor. The modulation bandwidth is limited as a result of suppression of the resonance frequency due to the presence of nonlinear gain saturation and strong damping rates in semiconductor lasers. The linewidth enhancement factor (α-factor) is a critical parameter that determines both the static linewidth of the semiconductor laser and the instantaneous frequency of the device under direct current modulation, also known as the frequency chirp. Frequency chirp of semiconductor lasers leads to a dynamic broadening of the mode spectrum under current modulation and therefore limits the modulation rate in optical communication systems. For instance, frequency chirp has two major drawbacks in wavelength division multiplexing (WDM) systems. First it can interact with the fiber dispersion to create a power penalty which limits the number of channels or the distance over which the generated signal can propagate. Second, chirp broadens the transmitted spectrum and thus limits the channel spacing by interfering with adjacent channels. This channel spacing interference can even

be seen in short transmission links. Therefore, low chirp and high modulation bandwidth semiconductor lasers have been of particular research interest for decades [1]-[6].

3.1.1 α-factor in QD and QDash Nanostructure Lasers

As discussed in previous chapters, compared to QW and bulk material systems, nanostructure lasers such as QD and QDash are known to exhibit many interesting advantages which are due to their unique carrier dynamics resulting from the delta-function-like density of states and three dimensional carrier confinements. More specifically, potential for high differential gain and a small α-factor make QD and QDash laser devices unique from other material structures and suitable for high-speed applications. Below-threshold measurements have reported α-factor values, both negative and less than 1, for QD lasers [7]-[9]. The main drawback is that the carrier density in QD lasers is not clearly clamped at threshold due to the inhomogeneous gain broadening in QDs. As a result, the above threshold α-factor in QDs behave quite differently from the below threshold values, and at higher current densities it becomes more power dependent due to strong gain saturation [10], [11]. Furthermore, strong gain saturation with carrier density increases the damping effect in QDs, limiting their high frequency modulation performance. In chapter 2, both of these limitations were experimentally investigated for free-running QD and QDash lasers. The free-running experimental results show that the above threshold α-factor is highly variable with photon density and also the damping effect increases as a function of current density in these devices.

3.1.2   Controlling the α-factor through Optical Injection-Locking

Chapter 2 discussed an alternative solution to solve the damping effect in QD and QDash lasers through the external control technique of optical injection-locking. On one hand, optical injection was shown to reduce the damping effect of the slave laser by enhancing the resonance frequency and thereby extending the maximum achievable bandwidth of the coupled system [12]. On the other hand, it was also demonstrated that adjusting the frequency detuning and/or injection strength can significantly impact the α-factor in both QDash and QD lasers. Strong optical injection under the stable locking condition shifts the threshold gain of the slave laser and thereby decreases the carrier density which results in a reduced α-factor. The maximum possible threshold gain shift limit defines the lowest achievable α-factor and is proportional to the slave laser's cavity photon decay rate. More specifically, experimental findings from chapter 2 on an injection-locked QD laser indicate that under strong optical injection, the α-factor in this device can be significantly reduced from a free-running value of 2 to near zero or perhaps negative values. In the latter case, the error in the parameter extraction was too large to be definitive. This reduced α-factor decreases the linewidth broadening, therefore reducing the effects of fiber dispersion pulse broadening, allowing for longer transmission lengths and higher bandwidth-length (BL) product [13]. From an application prospective, the combination of large bandwidth and low frequency chirp along with other benefits in optically injection-locked nanostructure lasers is promising for implementation in transmitter modules driving future long-haul and high-speed optical fiber links. The goal of this chapter is to use the benefits of the highly variable α-factor in nanostructure lasers

and experimentally investigate the manipulation of the α-factor in a nanostructure laser device under strong optical injection.

3.1.3 High-Level Objectives of the α-factor Investigation

In Chapter 2, the impact of the slave α-factor on injection-locked QDash and QD nanostructure lasers was theoretically and experimentally investigated. Both theoretical simulations and experimental results on an injection-locked QDash laser showed that a higher slave laser α-factor can impact the injection-locked system modulation response. Particularly, there is a reduction in the undesired pre-resonance dip in the modulation response at the positive frequency detuning edge, making this detuning condition suitable for broadband applications. Unfortunately, large α-factor values lead to significant frequency chirp through fiber transmission which limits the positive frequency detuning case to short-haul applications only.

This chapter exclusively focuses on the impact of strong optical injection on α-factor in the QDash FP laser and the corresponding modulation response at zero-detuning. Emphasis on the zero-detuning case is mainly based on two reasons. First, the zero-detuning case simplifies the theoretical model describing the behavior of the coupled system under modulation, making it easier to simulate and extract the operating parameters of the locked system from measured response data. Second, this case demonstrates a relatively flat modulation response compared to other detuning conditions making it most suitable for broadband applications. From an implementation perspective, the master and slave lasers can be referenced to the same wavelength locker, facilitating

implementation in a compact butterfly package suitable for high-speed applications in optical fiber links.

In this study, manipulation of the slave laser's α-factor in a QDash FP laser with optical injection is investigated using two different approaches. First, using the amplified spontaneous emission (ASE) technique, the QDash material properties, including the net modal gain profile and below-threshold α-factor, are separately measured as a function of wavelength and current density. Knowing the free-running material properties is very important in identifying the optimum free-running operating point at which the α-factor can be manipulated to the lowest possible values under optical injection. Then, the above threshold α-factor is directly measured under optical injection-locking as the injected optical power is varied using the ratio of the frequency modulation (FM) to the amplitude modulation (AM) indices technique. Second, measured experimental modulation response data is used to extract the relevant operating parameters of the coupled system including the threshold gain shift and α-factor, as it was described in chapter 2. The FM/AM measured α-factor values are then compared with the extracted values and the results are correlated with the threshold gain shift caused by optical injection.

It is important to note that the frequency chirp in directly modulated semiconductor lasers is not always considered a disadvantage since light chirping can also be useful for some applications such as narrowband frequency shift keying (FSK) modulation for labeling purposes [14]. Therefore, the external control technique of injection-locking described here along with the benefits of a highly variable α-factor in QD and QDash nanostructure lasers can be further implemented to adjust the desired chirp parameter for such applications.

127

3.2 Characterization of the Material α-factor in a QDash Laser

The α-factor is defined as the ratio of the partial derivatives of the real and imaginary parts of the complex susceptibility (i.e. of the refractive index n and gain g), $\chi(n)=\chi_r+i\chi_i$ with respect to carrier density [15]. Since the induced carrier contribution to the refractive index and the imaginary part of the susceptibility are much smaller than the refractive index in the absence of carriers, the α-factor can be expressed as follows [16], [17]:

$$\alpha = -\frac{\partial \chi_r / \partial N}{\partial \chi_i / \partial N} = -\frac{4\pi}{\lambda} \frac{\partial n / \partial N}{\partial g / \partial N} \qquad (3.1)$$

where $n(\lambda, N)$ is the refractive index of the active medium, $g(\lambda, N)$ is the net modal gain per unit length, λ is the peak emission wavelength in vacuum and N is the carrier density. Both the refractive index and gain terms have wavelength and carrier density dependence.

Since the first introduction of the amplitude-phase coupling parameter (α-factor) in the early 1980's [18], several techniques have been implemented to measure the α-factor in semiconductor lasers. The most commonly used methods are based on the analysis of the amplified spontaneous emission (ASE) [19], the FM/AM response ratio under small-signal modulation [20], linewidth measurements [21], optical feedback interferometeric self-mixing [22] and the injection-locking technique [23]. These techniques can be classified into two different categories: the first type is based on sub-threshold gain/refractive index measurements and can be used to evaluate the *material* α-factor; the second type is based on above-threshold measurements and is capable of measuring the *effective* above-threshold α-factor. When measuring the above-threshold α-factor of a

device subject to optical injection, it is also very important to first evaluate the material α-factor to characterize the related material properties of the device affecting this parameter at higher photon densities.

In the following section, the net optical gain of the QDash FP laser is measured through the ASE technique to identify the wavelength and carrier density dependence of the material α-factor in this device.

3.2.1   ASE/Hakki-Paoli Technique for Determining the Material α-factor

The ASE method of determining the optical gain, also known as the Hakki-Paoli method, is the most common technique for measuring the material α-factor as a function of current density and photon energy [19]. This technique relies on directly measuring the differential gain, *dg*, and differential index, *dn*, as a function of a slight change in the semiconductor laser carrier density in sub-threshold operation. The measurement is typically performed using an optical spectrum analyzer (OSA). The differential index is measured through detection of the frequency shift of the longitudinal FP mode resonances, while the differential gain is obtained by measuring the net modal gain from the FP modulation depth (gain ripple) in the ASE spectra of the laser [24]. Although this method is reliable and straightforward, there are two critical issues that can affect the accuracy of this measurement. First, this method requires the use of a high resolution OSA for the case of closely spaced longitudinal modes and also to minimize the experimental error of the measurement. Second, the thermal peak wavelength shift occurring in CW measurements needs to be eliminated from this measurement in order to only account for the net carrier-induced effects.

The net modal gain, g_{net}, can be extracted from the peak-to-valley ratio of sub-threshold ASE spectra using the following relationship [25]:

$$g_{net} = \frac{1}{L} Ln\left(\frac{1}{\sqrt{R_1 R_2}} \left[\frac{\sqrt{x}-1}{\sqrt{x}+1} \right] \right) \qquad (3.2)$$

where L is the laser cavity length, x is the ratio of the peak-to-valley intensity levels, and R_1 and R_2 are the front and back facet reflectivity, respectively. The data for the net modal gain for various injected current densities are shown in Figure (3.1). Note the blue shift in the gain peak as the pump level increases.
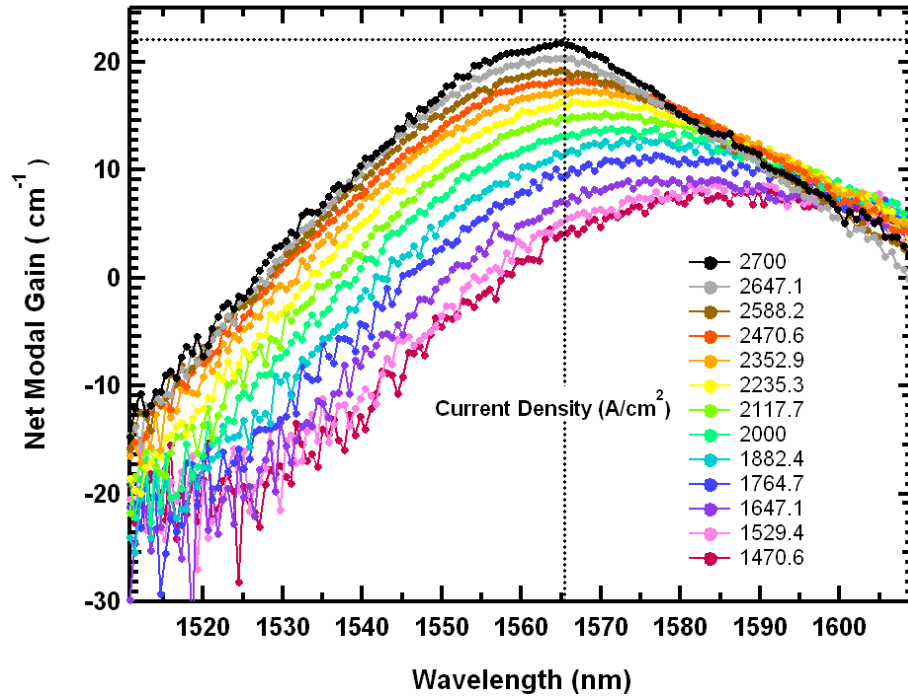
Figure (3.1) Net modal gain as a function of wavelength calculated from the peak-to-valley ratios in ASE spectra ranging from 1470.6 A/cm^2 to 2700 A/cm^2.

Using the measured net gain profiles for a small current increment of ΔI (or small ΔN), dg and dn can be calculated by replacing the partial derivatives with $\Delta g/\Delta I$ and $\Delta n/\Delta I = -(n/\lambda)\Delta\lambda/\Delta I$, respectively [26]. Using the expression in (3.1) and substituting for the differential gain and differential index definitions, yields the following experimental relationship for the material α-factor:

$$\alpha = -\frac{4\pi}{\lambda}\frac{\partial n/\partial N}{\partial g/\partial N} = -\left(\frac{4n\pi}{\lambda^2}\right)\frac{\Delta\lambda/\Delta I}{\Delta g/\Delta I} \qquad (3.3)$$

Using this method, a below-threshold ASE measurement was performed to measure the net modal gain and material α-factor for the QDash FP device described in chapter 2. The experimental setup used for this measurement was similar to the one described in Figure (2.2a) for the free-running device characterization except for the high-speed characterization equipment. For the ASE measurement, the CW current supply was replaced by an ILX LDP-3811 pulsed current source to eliminate the heating effects from the $\Delta\lambda/\Delta I$ measurements. Under CW operation, temperature effects in the QDash laser cavity can offset the blue shift in the peak wavelength resulting from increased bias currents. In order to minimize the temperature effects from the measurement, the device temperature was carefully monitored and kept constant at 20°C throughout the measurement. Then the QDash device was biased using 6 μs pulse widths while the duty cycle varied from 1% to 100% in 10% increments. The measured optical spectra were least-squares-fit using a Gaussian fitting function, and the peak wavelength was recorded for each duty cycle increment. For each sub-threshold bias current, the peak wavelength values were plotted as a function of duty cycle, and the results are shown in Figure (3.2). The plotted data was then extrapolated to 0% duty cycle (at y-axis intercept)
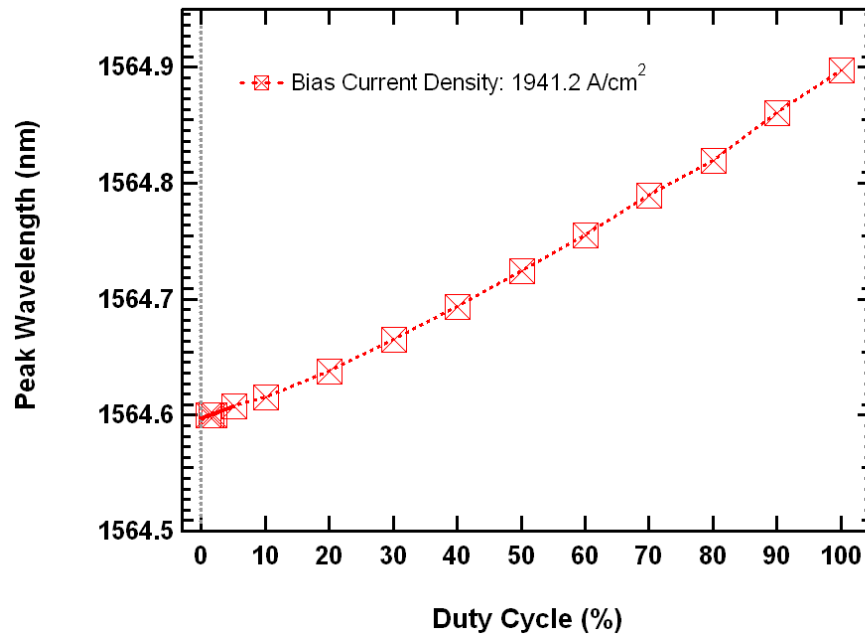
Figure (3.2) Peak wavelength as a function of duty cycle at J=1941.2 A/cm². The pulse width was kept constant at 6 μs for all cases.
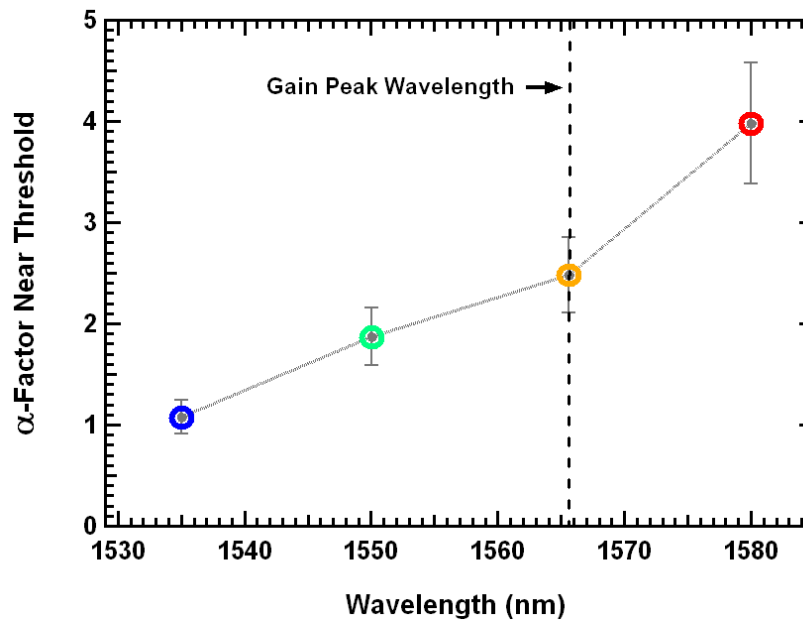
Figure (3.3) Variation of the material α-factor as a function of wavelength taken near threshold at current density value of 2647.1 A/cm².

and a 1 mA current step was used to calculate $\Delta\lambda/\Delta I$. Since the α-factor has wavelength dependence, the material α-factor of the QDash device was calculated using (3.3) at four different wavelengths: 1579.9 nm, 1565.2 nm, 1550.1 nm, 1534.6 nm. The results shown in Figure (3.3) verify that the material α-factor values are smaller at shorter wavelengths with respect to the gain peak at a current density value of 2647.1 A/cm^2 that is close to threshold. This result agrees with theory predicting a larger differential gain at wavelengths blue shifted from the gain peak, resulting in smaller α-factors [27]. Since optical injection by the master laser is at a fixed wavelength and increasing injection strength shifts the threshold condition to lower pump values, the α-factors is expected to progressively decrease with injection as operation is more and more on the blue side of the gain peak. In addition, the α-factors at all wavelengths generally decreases with a lower threshold condition in quantum dashes because of lower carrier population in the excited states [9].

3.3 Direct Measurement of the Above Threshold α-factor in QDash Laser under Optical Injection

In chapter 2, the above-threshold α-factor of the free-running QDash laser as a function of bias current was measured using the injection-locking technique. It was shown that the above threshold α-factor increases from ~1.0 to 11 as the applied bias current is increased from its threshold value to about twice the threshold in the free-running QDash laser. In analyzing the below threshold ASE measurement results, it was found that the material α-factor of the QDash laser fluctuates significantly with bias current. Based on the observation of large variations in both the above and below threshold α-factor for this device, we can predict that under strong optical injection, QDash laser should exhibit even lower α-factor values as a result of the threshold gain shift from its free-running value. In this study, the QDash device's α-factor is directly measured under optical injection as the injection power is varied using the FM/AM modulation technique and a high resolution optical spectrum analyzer (OSA).

3.3.1 Description of the FM/AM Modulation Technique

First demonstrated by Harder *et. al* in 1982, the FM/AM modulation method is an accurate measurement technique to evaluate the above-threshold α-factor of single-mode semiconductor lasers [20]. This technique relies on the high-frequency small-signal modulation of the carrier density of the laser obtained by modulation of the bias current. Since the gain and refractive index are both carrier density dependent, modulation of carrier density will generate amplitude and frequency modulation in the output signal.

From the small-signal modulation analysis it was known that the ratio of the FM/AM modulation indices provides a direct measurement of the above threshold α-factor [20].

Consider the electric field $E(t)$ as a sinusoidally modulated signal composed of a modulation frequency of f_m and a lasing frequency of f_0 as follows [20]:

$$E(t) = E_0 \left(1 + \frac{m}{2}\cos(2\pi f_m t)\right)\cos[2\pi f_0 t + \beta\cos(2\pi f_m t)] \tag{3.4}$$

In (3.4), m is the amplitude modulation index, and $\beta = \Delta f / f_m$ is the frequency modulation index (where Δf is the maximum frequency deviation). Assuming a small-signal modulation scheme ($m<<1$), the spectral density of the field amplitude can be approximated for the center line I_0 (at f_0) and the first sidebands I_1 (at $f_0 \pm f_m$) as the following expressions [28]:

$$I_0 = \left[J_0^2(\beta) + (\frac{m}{2})^2 J_1^2(\beta) \right] \tag{3.5}$$

$$I_1 = \left[J_1^2(\beta) + \left\{ \frac{m}{4}(J_0(\beta) - J_2(\beta)) \right\}^2 \right] \tag{3.6}$$

where $J_n(\beta)$ are n^{th} order Bessel functions. Using (3.5) and (3.6), the FM index β can be numerically evaluated by measuring the relative sideband strength I_1/I_0 from the spectral response of the laser. The AM index m, also known as the modulation depth, can be measured using direct optical signal detection from the ratio of the modulated signal over the carrier signal amplitudes. Under the direct modulation scheme described above, the relationship between m, β, and the α-factor is described as an FM/AM response $2(\beta/m)$ as follows [29]:

$$\frac{2\beta}{m} = \alpha \left[1 + \left(\frac{f_c}{f_m} \right)^2 \right]^{1/2} \qquad (3.7)$$

where $f_c = (1/2\pi) v_g (\partial g / \partial P) P$ is the characteristic frequency related to the group velocity v_g, the output power P, and $\partial g / \partial P = \varepsilon_p g / (1 + \varepsilon_p P)$ which represent the impact of nonlinear gain compression as a function of output power [30]. ε_p is the gain compression factor related to the output power. Note that the ratio of $2\beta/m$ in (3.7) is strongly dependant upon the modulation frequency f_m [30]. As the modulation frequency f_m increases, the FM/AM response decreases rapidly until it reaches an asymptote at $f_m \gg f_c$, in which it then becomes proportional to the α-factor value. Using this approximation and rearranging (3.7), the α-factor can be determined by:

$$\alpha \approx \frac{2\beta}{m} \qquad (3.8)$$

It is important to note that the above expression is only valid for small-signal modulation cases ($m \ll 1$) and high modulation frequencies ($f_m \gg f_c$).

In a similar approach, a modified method was proposed by Zhang *et. al*, which uses a graphical solution to estimate the α-factor [31]. In this method, I_0, along with the first I_1, and second I_2, modulation side bands are measured from the spectral response of the modulated signal. By varying the modulation depth, the ratios of $\xi = I_1 / I_0$ and $\varsigma = (I_1^2 / I_0 I_2)$ are calculated and plotted on a contour diagram with the x- and y- axis being m and β, respectively. As shown in Figure (3.4), the graphical solution is a straight line which intercepts the contour diagram origin. Using the expression (3.8) and at high modulation frequencies, the value of the α-factor can be extracted from the slope of the
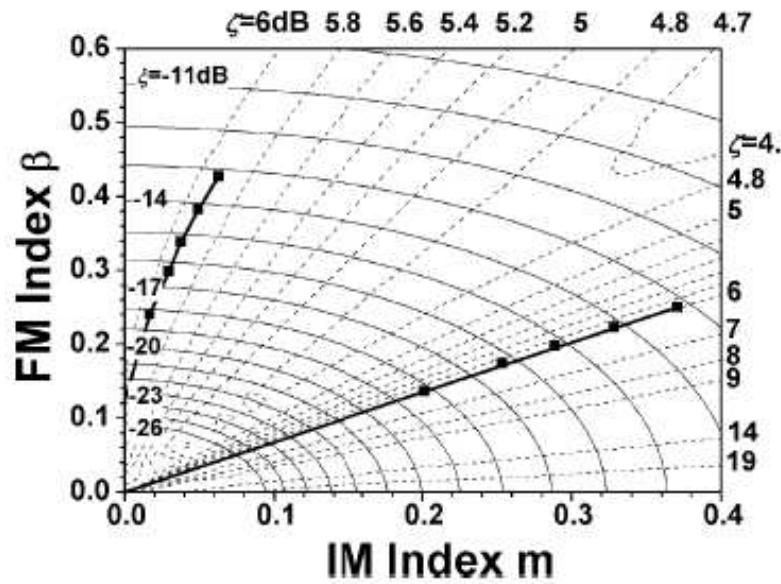
Figure (3.4) Sample contour diagram used to extract m and β from graphical solution [31]. The solid lines correspond to (I_1/I_0) and dashed lines represent $(I_1^2/I_0 I_2)$.

graphical solution. The graphical solution is an easy method to estimate the α-factor of the laser using the FM/AM indices but, there are some limitations associated with this technique. First, when measuring the second order sidebands, the modulation power should be large enough to ensure that the second sidebands are in the dynamic range of the OSA. Second, the accuracy of the measurement can be altered by unwanted second harmonic signals generated by the RF source at high modulation depths. The main problem with this method is the limited dynamic range of the graphical solutions. Moreover, this method cannot be implemented in the injection-locked QDash device in which the α-factor is expected to significantly vary as a function of injection strength.

In this dissertation, the α-factor of the QDash device under optical injection was directly evaluated using the direct measurement of *m*, and *β*. The modulation index *m*

was measured by direct detection using a photodiode and a sampling oscilloscope. The modulation index β was measured using a high resolution OSA. The following section gives the description of the experimental setup used for this measurement.

3.3.2   FM/AM Measurements - Experimental Setup

Figure (3.5) shows the injection-locking setup for measuring the modulation response and α-factor using the FM/AM modulation technique. The injection-locking part of the setup is similar to the one presented in chapter 2. The slave laser was DC biased slightly above threshold at 60mA and directly modulated. The modulated signal was provided by the HP 8722D network analyzer's internal RF source where it was also
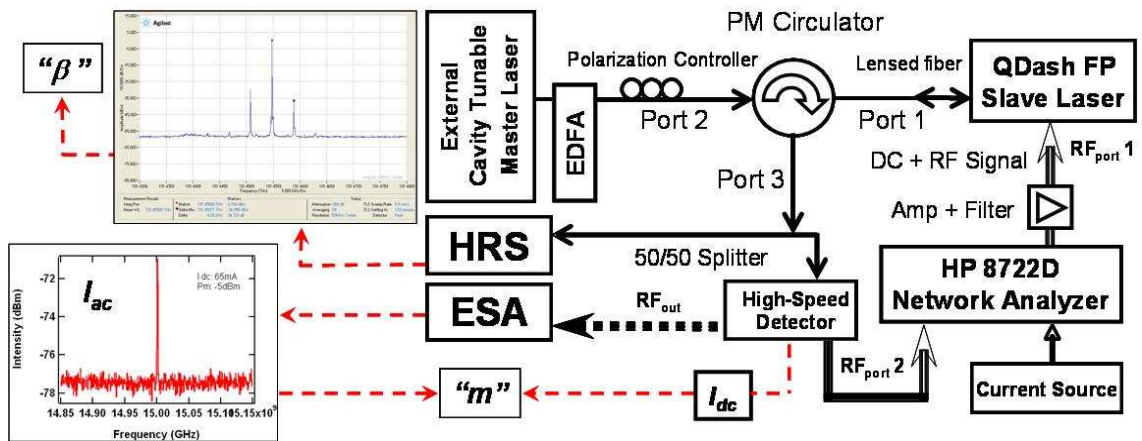
Figure (3.5) Block diagram of the experimental setup used to characterize the modulation response and α-factor of the injection-locked FP QDash using the FM/AM modulation technique (this schematic is not drawn to scale).
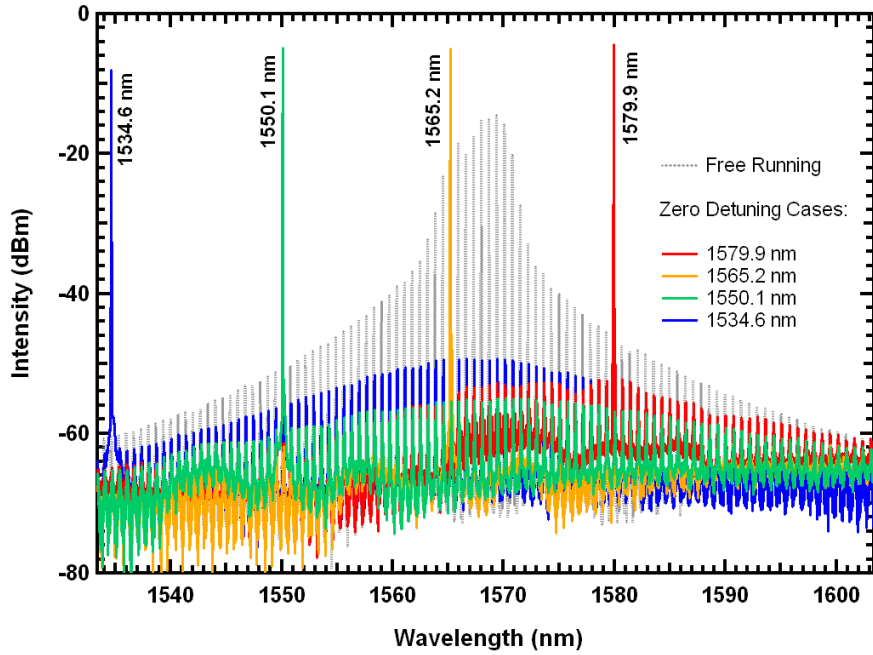
Figure (3.6) Free-Running and zero-detuning injection-locked spectra of the QDash FP slave laser at different wavelengths.

mixed with the DC current through an integrated bias-tee. An 18 GHz RF signal amplifier was connected to RF port 1 of the modulation setup to adjust the RF power as needed. To prevent the second harmonic generation by the RF source, a 20 GHz low-pass filter was used after the amplifier. Using a New Focus external tunable laser, the slave was then injection-locked for the zero-detuning case exactly at four different wavelengths as shown in Figure (3.6). In all of the injection-locking cases, the external power ratio, R_{ext} (master to slave power ratio at the external slave facet), was varied between -3.8 dB to 9.3 dB using a C-band optical amplifier (EDFA) for the 1565.2 nm, 1550.1 nm and 1534.6 nm cases and an L-band amplifier for the 1579.9 nm case. A Santec tunable bandpass filter was placed after the EDFA to eliminate the excess noise coming out of the amplifier (the bandpass filter is omitted from the block diagram for clarity). Also, an in-

line polarization controller was used after the filter to maximize the injected power. The injection-locking setup was capable of a maximum amplified optical power of 27 mW which was limited by an overall 5 dB loss resulting from the polarization controller, bandpass filter and fiber connectors. The AM index m was modified through the ratio of the ac and dc components of the detected modulated signal using an electrical spectrum analyzer (ESA) and a 50 Ω terminator connected to a high-speed photodetector. While the external power ratio was varied, the AM index m was kept constant at 6% for all injection-locking cases by adjusting the RF power output from the amplifier. The FM index β was obtained by measuring the ratio of the first sidebands to the center carrier frequency amplitudes as a function of modulation frequency (f_m=1 GHz - 15 GHz) using an Agilent 83453B high resolution (1 MHz) spectrometer (HRS).

The figure contains the equation:

$$\left|\frac{2\beta}{m}\right| = \alpha\left[1+\left(\frac{f_c}{f_m}\right)^2\right]^{1/2}$$
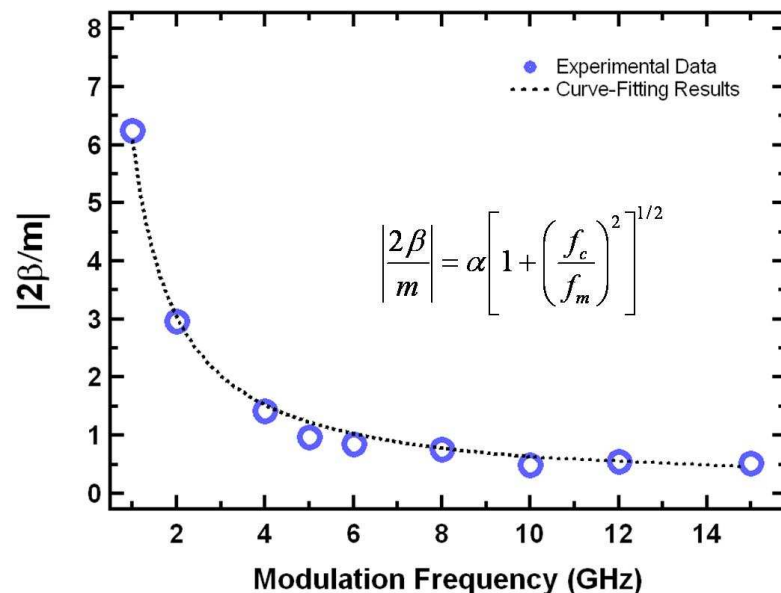
Figure (3.7) Sample injection-locked QDash FM/AM response as a function of modulation frequency curve-fitted to (3.7) to characterize the α-factor.

140

Using the measured center and sideband amplitudes to calculate the relative sideband strength I_1/I_0, β can be found as a function of frequency by plotting the left and right hand-side of (3.5) and (3.6) from the intercept between the two graphs. Since the FM/AM response $2\beta/m$ has strong frequency dependence, the actual value of the α-factor for each case was found by curve-fitting the measured $2\beta/m$ response as a function of modulation frequency using (3.7) as illustrated in Figure (3.7).

3.3.3   FM/AM Measurements - Experimental Results

Figure (3.8) gives the measured FM/AM modulation values of the α-factor as a function of R_{ext} for zero-detuning cases at 1579.9 nm, 1565.2 nm, 1550.1 nm, and 1534.6-
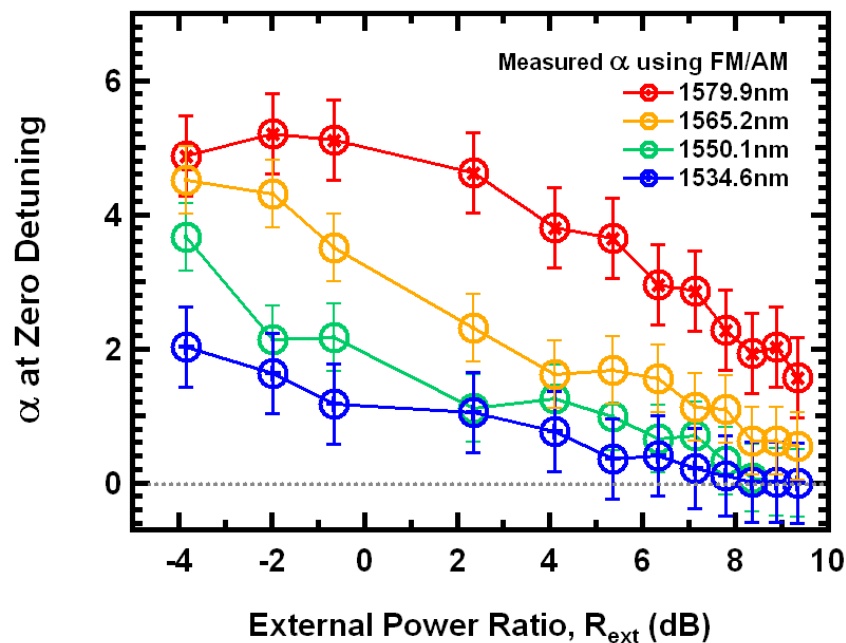
Figure (3.8) Measured α-factor as a function of R_{ext} at zero-detuning cases using FM/AM modulation technique.

141

nm. Measured results for all zero-detuning cases indicate that α-factor decreases significantly as R_{ext} increases, which is due to the decreasing carrier density caused by the injection-induced threshold shift and the associated red shift of the gain peak. As also predicted by theory and expected from the experimentally measured material α-factor, strong optical injection-locking at lower wavelengths from the gain peak resulted in lower α-factor for the QDash slave laser. The lowest α-factors were generally very close to zero and obtained for the 1534.6 nm zero-detuning case from R_{ext}= 7.8 to 9.3 dB. To the best of our knowledge this is the lowest α-factor ever reported for an InP based QDash laser.

3.4 Extracting the α-factor and Threshold Gain Shift using the Zero-Detuning Modulation Response Data

For comparison and also to confirm the accuracy of the measured α-factor values, the experimental modulation response data at each zero-detuning case was used to extract the relevant operating parameters of the system as described in chapter 2. Since the FM/AM method used here only measures positive values, the α-factor sign can also be identified by the extracted values from the simulations. The FM/AM measured α-factor values are then compared with the extracted values and the results are correlated with the threshold gain shift caused by optical injection. As described in the previous chapter for zero-detuning case, the injection-locking modulation response function can be simplified through reduced expressions for the steady-state phase offset as $\phi_0 = -\tan^{-1}(\alpha)$, the zero of the function, $Z = -(\eta_0/R_{FE})[1+\alpha^2]^{1/2}$ and the threshold gain shift, $\gamma_{th} = (2\eta_0/R_{FE})[1+\alpha^2]^{-1/2}$.

Using these simplified equations to fit measured response data, the number of fitting

parameters is reduced using known free-running terms and by applying proper constraints

on R_{FE}, and γ_{th}. The maximum injection strength, η_0, is separately calculated using (2.36)

and was tightly constrained during the curve-fitting. By solving a quadratic expression

arising from the steady-state slave field equation given in (2.27) and the simplified

expression for γ_{th} at zero-detuning, one can generate an initial guess value for R_{FE} using

the resulting quadratic equation in R_{FE}^2:

$$R_{FE}^4 - \left[\left(\frac{1}{\gamma_P} \right) \left(\frac{2\eta_0}{\sqrt{1+\alpha^2}} \right) + 1 \right] R_{FE}^2 - \left(\frac{\gamma_N}{\omega_r^2} \right) \left(\frac{2\eta_0}{\sqrt{1+\alpha^2}} \right) = 0 \qquad (3.9)$$

Using the measured FM/AM values, the α-factor was allowed to fluctuate between

Figure (3.9) Free-running and injection-locked modulation responses at zero-detuning as a function of R_{ext}. The zero-detuning response data corresponds to the optical injection locking near the gain peak wavelength at 1565.2 nm. The experimental response data is curve-fitted using the simplified modulation response function.

a reasonable positive and negative range. Both the α-factor and γ_{th} were directly extracted using the modulation response function presented in (2.31). Figure (3.9) shows the normalized zero-detuning modulation response data at zero-detuning and near the gain peak wavelength at 1565.2 nm for various values of R_{ext}. The response data at this zero-detuning case shows that as the injection strength increases, the 3-dB modulation bandwidth improves as a result of an enhanced resonance frequency until the response curve drops below the 3-dB line at R_{ext}=7.1 dB where the damping effect is more dominant. The maximum 3-dB bandwidth at R_{ext}=6.3 dB is about 18 GHz, which corresponds to a 4X improvement compared to the free-running case. The curve-fits of the modulation response data in Figure (3.9) give an α-factor value and the related threshold gain shift as a function of R_{ext}. For comparison, the extracted and measured α-factor values along with the corresponding threshold gain shifts in GHz are plotted as a function of R_{ext} in Figure (3.10). The extracted values of the α-factor at zero-detuning near the gain peak are in good agreement with the FM/AM technique measured values. As described earlier, the maximum possible threshold gain shift is the cavity photon decay rate, γ_p, which is approximately 312 GHz for the QDash laser under investigation. As indicated in Figure (3.10), the extracted values for the threshold gain shift show a significant increase with R_{ext}. The highest threshold gain shift for the zero-detuning case near the gain peak is about 198 GHz which is about 63% of the maximum possible value.

Using a similar approach, the zero-detuning modulation responses at 1579.9 nm, 1550.1 nm and 1534.6 nm are curve-fitted and the extracted results are compared in Figures (3.11) through (3.13) with the α-factor values measured by the FM/AM technique. The operating parameters extracted through least-squares-fitting data collected

Figure (3.10) Comparison between measured and extracted α-factor and extracted threshold gain shift at zero-detuning cases as a function of R_{ext}. The measured and extracted values correspond to the injection-locking case near the gain peak wavelength at 1565.2 nm.

for each case are presented in Table (3.1)-(3.3). Sample zero-detuning modulation responses and corresponding curve-fitting results at these wavelengths are also shown in Figures (3.11)-(3.13). The modulation responses at 1579.9 nm shown in Figure (3.11a) indicate strong damping effects with increased R_{ext} compared to the zero-detuning responses near the gain peak wavelength at 1565.2 nm. The increased damping effect observed in the modulation responses at longer wavelengths from the gain peak is due to the non-linear gain compression scaling with the slave field enhancement as the injection strength is increased. As a consequence of this damping effect, the maximum 3-dB bandwidth is limited to only 8 GHz at R_{ext}=-0.6 dB. The zero-detuning modulation
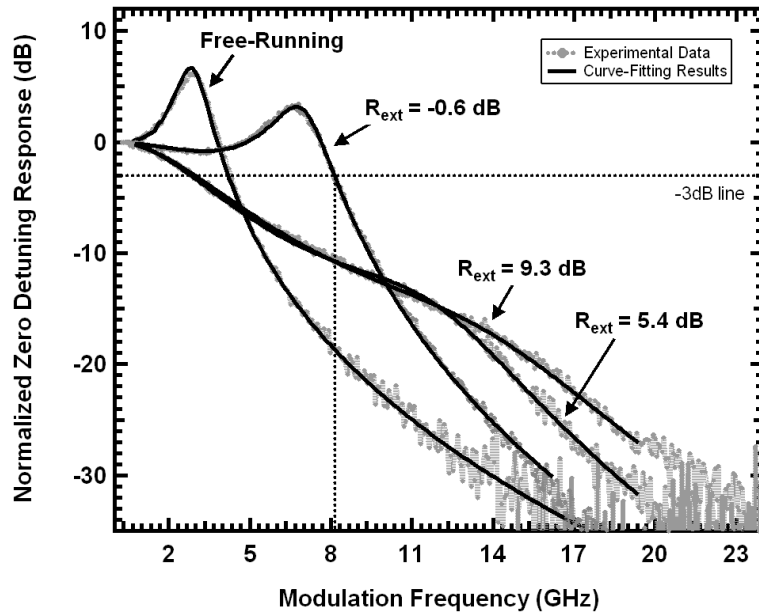
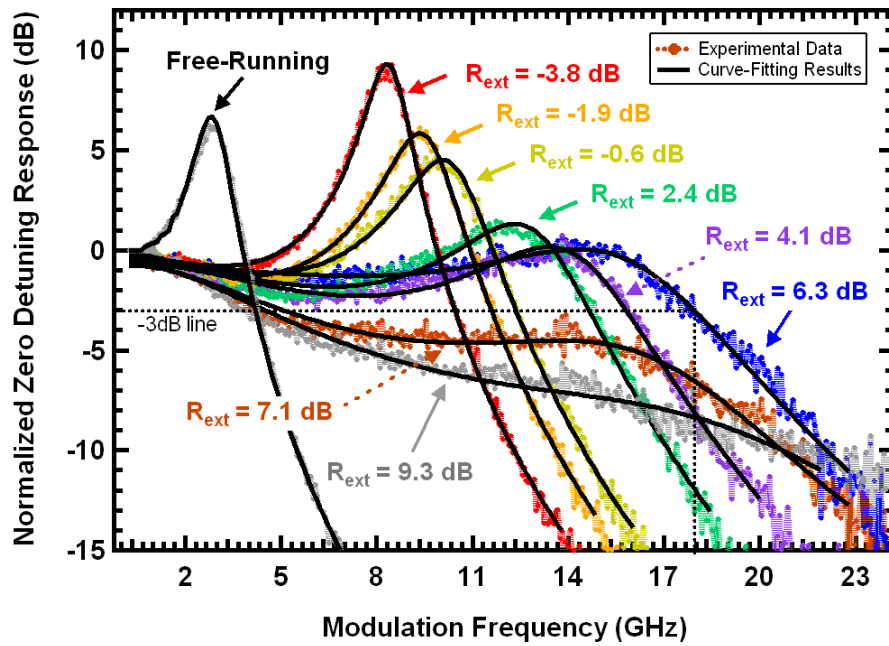*Figure (3.11a) Free-running and injection-locked modulation responses at zero-detuning as a function of R_{ext} for the mode at 1579.9 nm. The experimental response data are curve-fitted using a simplified modulation response function.*
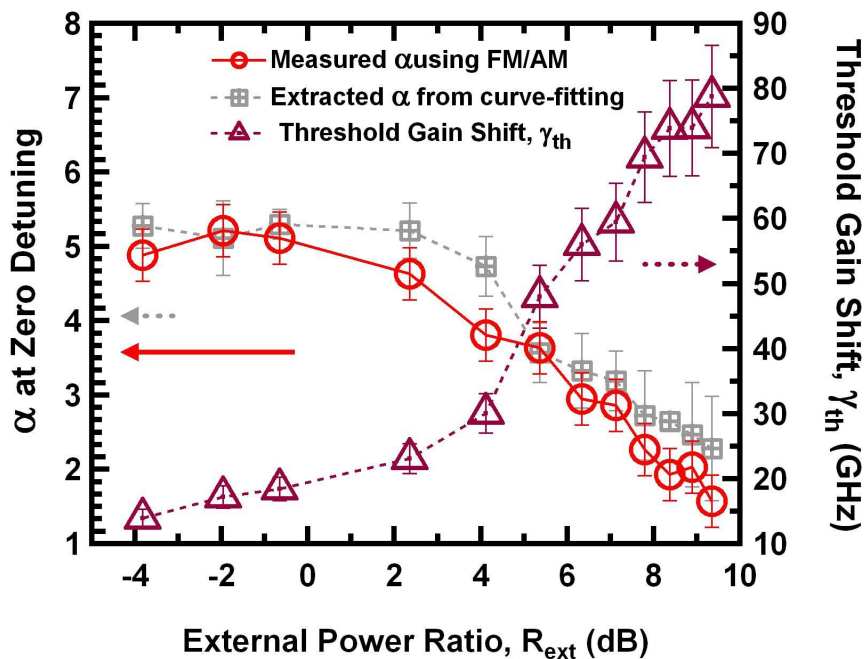
Figure (3.11b) Comparison between measured and extracted α-factor and extracted threshold gain shift at zero-detuning cases as a function of R_{ext}. The measured and extracted values correspond to the injection-locking case at 1579.9 nm.
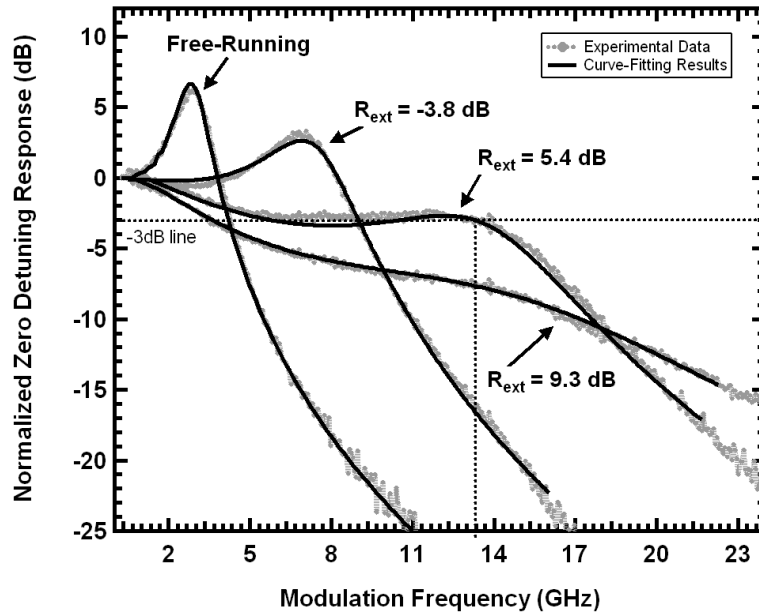
Figure (3.12a) Free-running and injection-locked modulation responses at zero-detuning as a function of R_{ext} for the mode at 1550.1 nm. The experimental response data are curve-fitted using a simplified modulation response function.
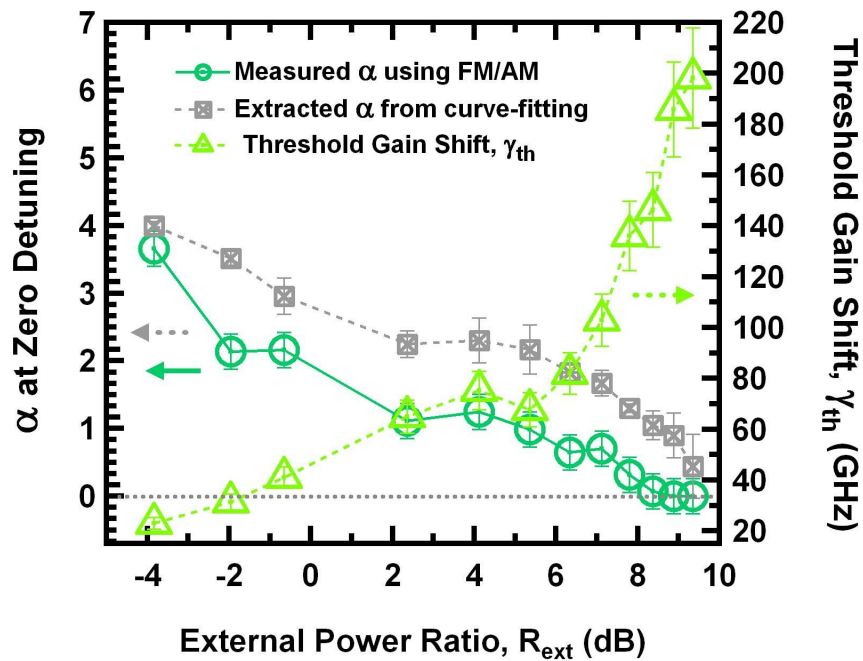
Figure (3.12b) Comparison between measured and extracted α-factor and extracted threshold gain shift at zero-detuning cases as a function of R_{ext}. The measured and extracted values correspond to the injection-locking case at 1550.1 nm.

147
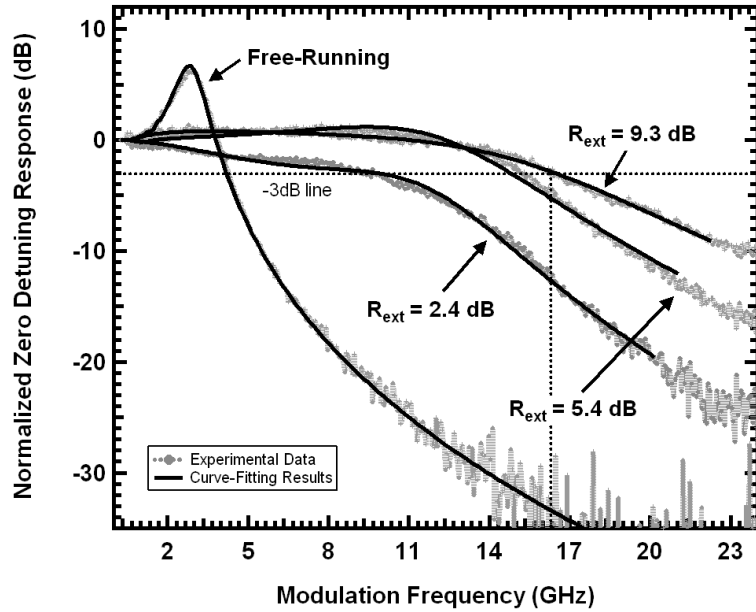
Figure (3.13a) Free-running and injection-locked modulation responses at zero-detuning as a function of R_{ext} for the mode at 1534.6 nm. The experimental response data are curve-fitted using a simplified modulation response function.
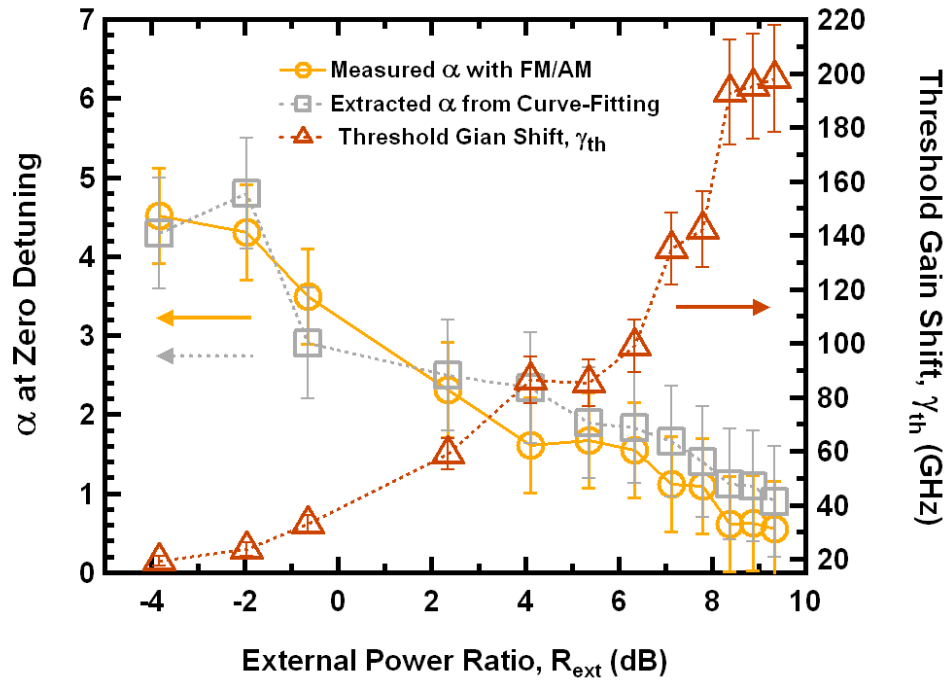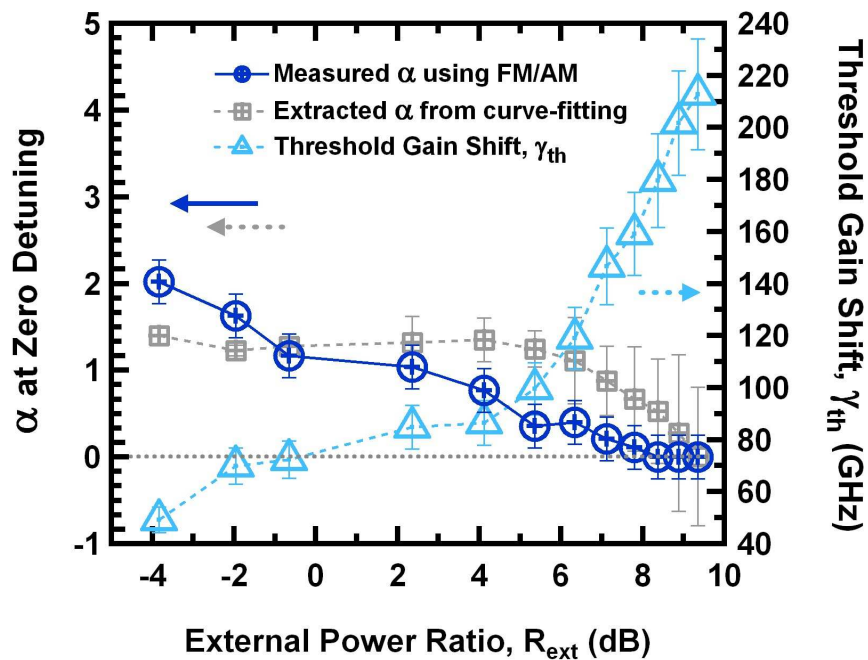

Figure (3.13b) Comparison between measured and extracted α-factor and extracted threshold gain shift at zero-detuning cases as a function of R_{ext}. The measured and extracted values correspond to the injection-locking case at 1534.6 nm.

TABLE (3.1)

Extracted injection-locking operating parameters at 1579.9 nm obtained from the least-squares-fit of experimental data.

R_{ext} (dB)	η_0 (GHz)	α	R_{FE}	γ_{th} (GHz)
-0.6	71.4 ±2	5.1 ±0.09	1.27 ±2×10^{-5}	19.3 ±4.2
5.4	146.8 ±4.6	3.6 ±0.4	1.48 ±3×10^{-4}	50.6 ±6.1
9.3	230 ±5.7	2.28 ±0.7	2.01 ±1×10^{-3}	79 ±9.5

TABLE (3.2)

Extracted injection-locking operating parameters at 1550.1 nm obtained from the least-squares-fit of experimental data.

R_{ext} (dB)	η_0 (GHz)	α	R_{FE}	γ_{th} (GHz)
-3.8	51.1 ±2.7	4 ±0.06	1.15 ±2×10^{-4}	21.5 ±0.9
5.4	147.3 ±5	2.53 ±0.3	1.63 ±1×10^{-4}	77.8 ±3.1
9.3	228.9 ±9.2	0.4 ±0.5	1.93 ±3×10^{-2}	198.2 ±18

TABLE (3.3)

Extracted injection-locking operating parameters at 1534.6 nm obtained from the least-squares-fit of experimental data.

R_{ext} (dB)	η_0 (GHz)	α	R_{FE}	γ_{th} (GHz)
2.4	96.2 ±0.8	1.32 ±0.3	1.32 ±5×10^{-3}	84.8 ±2.3
5.4	145.6 ±2.4	1.25 ±0.5	1.62 ±7×10^{-3}	99 ±7.5
9.3	229 ±7.1	0.001 ±0.8	2.16 ±2×10^{-1}	212.7 ±10.1
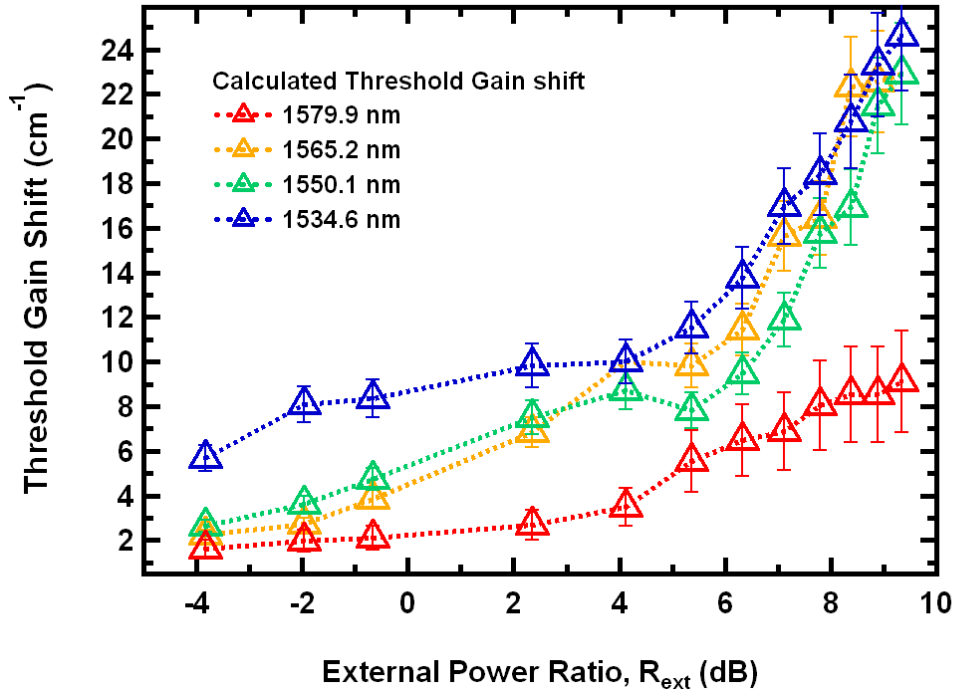
Figure (3.14) Calculated threshold gain shift for zero-detuning cases (as a function of R_{ext}) at 1579.9 nm, 1565.2 nm, 1550.1 nm, and 1534.6 nm.

responses shown in Figures (3.12a) and (3.13a) for 1550.1 nm and 1534.6 nm cases are relatively less damped compared to the previous case and have maximum 3-dB bandwidths of 13.3 GHz and 16.3 GHz respectively. Most notably, these values are only slightly lower than the maximum 3-dB bandwidth of the zero-detuning responses near the gain peak wavelength at 1565.2 nm. For the zero-detuning case at 1534.6 nm, the combination of a zero alpha-factor and the near flat modulation response shown in Figure (3.13a) for R_{ext} = 9.3 dB is close to ideal for an optical transmitter. This result is a first of its kind!

Some general comments can be made upon analyzing the α-factor values extracted from each case and using the modulation response function described in chapter

2. Considering the simplified modulation response function and associated parametric terms A and B at zero-detuning, the relationship between the phase, α-factor, and R_{FE} modifies the interaction between the injection strength, damping rate, and resonance frequency. As the α-factor is decreased, the damping rate driven by the A term increases at a faster rate than the enhanced resonance frequency expressed by the B term, resulting in a damped response at higher injection strengths as observed in Figures (3.12a) and (3.13a). Going back to the zero-detuning responses at 1579.9 nm, the α-factor is larger at this case which causes R_{FE} to scale much faster with injection strength. Another trend to notice for this case is that the A, and B terms are more sensitive to R_{FE} rather than the α-factor. Thus as the injection strength is increased, the A term increases and the B term decrease with R_{FE}^2 which lead to the heavily damped responses shown in Figure (3.11a).

As previously described in detail, the extracted α-factor and corresponding threshold gain shift values as a function of R_{ext} for different zero-detuning cases at 1579.9 nm, 1550.1 nm and 1534.6 nm are shown in Figures (3.11b)-(3.13b). The extracted α-factor values for these cases are within reasonable experimental error range which verifies the validity of the measured values using the FM/AM technique. The extracted values for the threshold gain shift in Figures (3.11b)-(3.13b) show a significant increase with R_{ext} for each wavelength. For a better side-by-side comparison, the corresponding threshold gain shift values are separately plotted as a function of R_{ext} in Figure (3.14). In this figure, the extracted threshold gain shift values are normalized to the group velocity as γ_{th}/v_g to express the gain shift in cm^{-1}. The results shown in Figure (3.14) verify that the overall threshold gain shift is larger for injection-locking cases at 1550.1 nm and 1534.6 nm compared to the case at 1565.2 nm which explains, in part, the lower α-factor

151

values at lower wavelengths from the gain peak. From the curve-fitting results an α-factor of 0.001 (or 0.0 within the curve-fitting error range) was extracted for the zero-detuning case at 1534.6 nm and R_{ext}=9.3 dB. The largest threshold gain shift for the zero-detuning case at 1534.6 nm is about 24.6 cm^{-1} which is about 68% of the maximum possible value and 5% more than that of the zero-detuning case at the gain peak. The maximum threshold gain shift for this case is equivalent to a reduced threshold current density of 1458 A/cm^2 from its free-running value. The extracted value for maximum threshold gain shift at 1550.1 nm case is about 64% of the maximum possible value which is only 1% higher than the shift at the gain peak. The largest gain shift at 1579.9 nm case is about 25% of the maximum possible value and 38% lower than the peak gain which explains the larger α-factor values found for this case.

To conclude, the QDash slave laser α-factor at zero-detuning and under strong optical injection was measured using the FM/AM technique. Using a small-signal response function describing the modulation characteristics of an injection-locked system under zero-detuning, the α-factor and threshold gain shift were extracted from measured microwave data as a comparison. The results verify that the QDash slave laser's α-factor can be manipulated through the threshold gain shift as a result of strong optical injection. As a result of this manipulation, an α-factor of 0.001 ($\pm$ 0.8) was obtained via simulation and an α-factor of 0.0 ($\pm$ 0.25) was obtained experimentally.

3.5 Chapter 3 References

[1] K. Inoue, "An experimental study on chirp noise in a directly modulated semiconductor laser," *IEICE Transactions on Communications*, Vol. E81-B, No. (6), pp.1197-1202, (1998).

[2] J. Feng, T. R. Chen, and A. Yariv, "On chirp control in two-section distributed-feedback semiconductor lasers," *Applied Physics Letters*, Vol. 67, No. (20), pp. 2913-2915, (1995).

[3] C. Y. Tsai, "Effects of carrier heating on the frequency chirping of semiconductor lasers," *Electronics Letters*, Vol. 33, No. (24), pp. 2043-2045 (1997).

[4] M. Bhattacharya, R. Mukherjee, and T. Chattopadhyay, "Reduction of frequency chirping in semiconductor lasers through injection locking," *IETE Journal of Research*, Vol. 45, No. (5), pp. 341-344, (1999).

[5] R. Vinzio, Z. Toffano, and A. Destrez, "Analytical formulation of distortion and chirp in CATV DFB lasers including spatial hole burning," *IEEE Journal of Quantum Electronics*, Vol. 34, No. (2), pp. 311-317, (1998).

[6] G. E. Shtengel, R. F. Kazarinov, G. L. Belenky, and C. L. Reynolds, "Wavelength chirp and dependence of carrier temperature on current in MQW InGaAsP-InP lasers," *IEEE Journal of Quantum Electronics*, Vol. 33, No. (8), pp. 1396-1402, (1997).

[7] P. M. Smowton, E. J. Pearce, H. C. Schneider, W. W. Chow, and M. Hopkinson, "Filamentation and linewidth enhancement factor in InGaAs quantum dot lasers," *Applied Physics Letters*, Vol. 81, No. (17), pp. 3251-3253, (2003).

[8]   A. V. Uskov, E. P. O'Reilly, D. McPeake, N. N. Ledentsov, D. Bimberg, and G. Huyet, "Carrier-induced refractive index in quantum dot structures due to transitions from discrete quantum dot levels to continuum states," *Applied Physics Letters*, Vol. 84, No. (2), pp. 272-274, (2004).

[9]   A. A. Ukhanov, "Study of the carrier-induced optical properties in III-V quantum confined laser nanostructures," *PhD Dissertation*, the University of New Mexico, (2004).

[10]   J. Muszalski, J. Houlihan, G. Huyet, and B. Corbett, "Measurement of linewidth enhancement factor in self-assembled quantum dot semiconductor lasers emitting at 1310nm," *Electronics Letters*, Vol. 40, No. (7), pp. 428-430, (2004).

[11]   A. Markus, J. X. Chen, O. Gauthier-Lafaye, J.-G. Provost, C. Paranthoen and A. Fiore, "Impact of intraband relaxation on the performance of a quantum-dot laser," *IEEE Journal of Selected Topics in Quantum Electronics*, Vol. 9, No. (5), pp. 1308-1314, (2003).

[12]   T. B. Simpson, J. M. Liu, A. Gavrielides, "Small-signal analysis of modulation characteristics in a semiconductor laser subject to strong optical injection," *IEEE Journal of Quantum Electronics*, Vol. 32, No. (8), pp. 1465-1468, (1996).

[13]   N. A. Olsson, H. Temkin, R. A. Logan, L. F. Johnson, G. J. Dolan, J. P. van der Ziel, and J. C. Campbell, "Chirp free transmission over 82.5 km of single mode fibers at 2 Gbit/s with injection locked DFB semiconductor lasers," *Journal of Lightwave Technology*, Vol. 3, No. (1), pp. 63-67, (1985).

[14]   A. Lopez, I. Garces, M. A. Losada, J. J. Martinez, A. Villafranca, and J. A. Lazaro, "Narrow-FSK optical packet labeling scheme for optical ethernet

networks," *IEEE Photonics Technology Letters,* Vol. 18, No. (16). pp. 1696-1698, (2006).

[15]   K. Vahala, L. C. Chiu, S. Margalit, and A. Yariv, "On the linewidth enhancement factor α in semiconductor injection lasers," *Applied Physics Letters*, Vol. 42, No. (8), pp. 631-633, (1983).

[16]   R. Lang, "Lateral transverse mode instability and its stabilization in stripe geometry injection lasers," *IEEE Journal of Quantum Electronics*, Vol. 15, No. (8), pp. 718-726, (1979).

[17]   K. Vahala, and A. Yariv, "Semi-classical theory of noise in semiconductor lasers-part 1," *IEEE Journal of Quantum Electronics*, Vol. 19, No. (6), pp. 1096-1101, (1983).

[18]   C. Henry, "Theory of the linewidth of semiconductor lasers," *IEEE Journal of Quantum Electronics*, Vol. 18, No. (2), pp. 259-264, (1982).

[19]   I. D. Henning, and J. V. Collins, "Measurement of the semiconductor linewidth broadening factor," *Electronics Letters*, Vol. 19, No. (22), pp. 927-929, (1983).

[20]   C. Harder, K. Vahala, and A. Yariv, "Measurement of the linewidth enhancement factor a of semiconductor lasers," *Applied Physics Letters*, Vol. 42, No. (4), pp. 328-330, (1983).

[21]   Z. Toffano, A. Destrez, C. Birocheau, and L. Hassine, "New linewidth enhancement determination method in semiconductor lasers based on spectrum analysis above and below threshold," *Electronics Letters*, Vol. **28**, No. (1), pp. 9-11, (1992).

[22]   Y. Giuliani, and S. Donati, "Measurement of the linewidth enhancement factor of semiconductor lasers based on the optical feedback self-mixing effect," *IEEE Photonics Technology Letters*, Vol. 16, No. (4), pp. 990-992, (2004).

[23]   G. Liu, X. Jin, S. L. Chuang, "Measurement of linewidth enhancement factor of semiconductor lasers using an injection-locking technique," *IEEE Photonics Technology Letters*, Vol. 13, No. (5), pp. 430-432, (2001).

[24]   B. W. Hakki, and T. L. Paoli, "Gain spectra in GaAs double-heterostructure injection lasers," *Journal of Applied Physics*, Vol. 46, No. (3), pp. 1299-1306, (1975).

[25]   D. J. Bossert and D. Gallant, "Improved method for gain/index measurements of semiconductor lasers," *Electronics Letters*, Vol. 32, No. (4), pp. 338–339, (1996).

[26]   T. C. Newell, D. J. Bossert, A. Stintz, B. Fuchs, K. J. Malloy, and L. F. Lester, "Gain and linewidth enhancement factor in InAs quantum-dot laser diodes," *IEEE Photonics Technology Letters*, Vol. 11, No. (12), pp. 1527-1529, (1999).

[27]   B. Riou, N. Trenado, F. Grillot, F. Mallecot, V. Colson, M.F. Martineau, B. Thédrez, L. Silvestre, D. Meichenin, K. Merghem and A. Ramdane, "High performance strained-layer InGaAsP/InP laser with low linewidth enhancement factor over 30 nm," *in proceedings of IEEE European Conference on Optical Communication*, (2003).

[28]   B. Moller, E. Zeeb, U. Fiedler, T. Hackbarth, and K. J. Ebeling, "Linewidth enhancement factor of vertical-cavity surface-emitting laser diodes," *IEEE Photonics Technology Letters*, Vol. 6, No. (8), pp. 921-923, (1994).

[29] R. Schimpe, J. E. Bowers, and T. L. Koch, "Characterization of frequency response of 1.5 μm InGaAsP DFB laser diode and InGaAs pin photodiode by heterodyne measurement technique," *Electronics Letters*, Vol. 22, No. (9), pp. 453-454, (1986).

[30] L. Olofsson, and T. G. Brown, "Frequency dependence of the chirp factor in 1.55 μm distributed feedback semiconductor lasers," *IEEE Photonics Technology Letters*, Vol. 4, No. (7), pp. 688-691, (1992).

[31] T. Zhang, N. H. Zhu, B. H. Zhang, and X. Zhang, "Measurement of chirp parameter and modulation index of a semiconductor laser based on optical spectrum analysis," *IEEE Photonics Technology Letters*, Vol. 19, No. (4), pp. 921-923, (2007).

Chapter 4

Two-Color Multi-Section Quantum Dot Distributed Feedback Laser

4.1   Introduction

Previous chapters studied the external control of the multi-mode nanostructure QD and QDash Fabry-Perot (FP) lasers by optical injection-locking as potential candidates for a wide variety of applications such as a chirp-free and high-speed optical communication system. After the successful demonstration of QD lasers in 1993 [1, 2], many unique dynamic properties of these nanostructures have been verified on actual laser devices including DFB lasers [3]. These properties were summarized in chapter 1 and the impact of external control techniques on the overall performance of nanostructure lasers was discussed. Among the interesting properties of QD and QDash lasers is the large inhomogeneous broadening of the gain spectrum as a result of size dispersion in dots which is usually considered as an important figure of merit in high-speed performance of such lasers. This chapter is focused on manipulating the spectral properties of a multi-section QD DFB laser by actually taking advantage of this usually undesired characteristic of QDs and combining it with the external control techniques of asymmetric pumping and optical feedback in order to generate simultaneous two-color emission in a single device.

4.2 Motivation for the Two-Color Multi-Section Laser

Terahertz (THz) technology has a wide variety of applications in fields as diverse as next generation computing and communications technologies, medical and pharmaceutical fields as well as basic material science and homeland security [4]-[8]. Recently, significant progress has been made in the field of THz source generation, which has created engineering opportunities that exploit this new technology [9]. Specifically, there has been interest in the development of THz optoelectronic sources since their electronic addressability and tunability would make them easier to operate [10]. For this particular source, two coherently interfering optical modes are typically generated by two single-mode lasers, and the light is absorbed in an ultrafast photoconductive semiconductor [11]-[13]. This process creates time varying electron and hole densities that, under the influence of an applied electric field, are accelerated and generate a THz wave that is equal to the difference frequency between the two optical modes [14]. Among other uses, such THz signals can be coupled to a radiating antenna for transmission [15], and the frequency of the THz signal can be changed by varying the wavelengths of the optical modes. In order to tune and stabilize the frequency output of the semiconductor lasers, an external cavity is commonly used that requires a relatively bulky opto-mechanical design. Thus, it is highly desirable to develop a THz signal source that is more compact and inexpensive to fabricate. One possible approach is to use a dual-mode semiconductor laser that features a device with two longitudinal modes simultaneously emitting at two different frequencies from a single or combined laser cavity [16]. The use of the dual-mode laser has the advantage of being free of optical alignment issues since there is no need to align two laser beams, which is critical for

159

photomixing efficiency. Several optical cavity approaches have been studied that achieve simultaneous two-color generation from a compact, monolithic system [17]-[20]. The dual-mode laser source for THz generation has been previously studied in bulk and quantum well (QW) semiconductor lasers [18]-[21], but very little is known about the behavior of QD active regions in these types of devices.

Compared to QW and bulk materials, nanostructures such as quantum dots (QDs) are known to have superior characteristics due to their ultrafast carrier dynamics, ultralow threshold current density, reduced linewidth enhancement factor, and improved temperature characteristics [22]-[25]. Simultaneous ground state (GS) and excited state (ES) with multi-mode emissions have been previously observed in QD material when increasing the bias current well above the threshold [26, 27]. The technical approach described in this chapter simultaneously addresses the need for compact size, low fabrication cost, and high performance by concurrently generating two single-mode emission peaks–one line from the GS and the other from the ES of the laser device. The laser source used in this investigation is a two-section Laterally Loss-Coupled (LLC) Distributed Feedback (DFB) laser in which the Bragg grating is coupled only to the QD ES. Two-color operation is realized through simultaneous GS emission that is uncoupled to the Bragg grating due to inhomogeneous broadening in the QD active medium.

In order to accurately characterize the performance of the DFB device under investigation, the values of the index and gain coupling coefficients are calculated by using the numerical least-squares-fitting of the sub-threshold spectra. The two-color emission is then demonstrated in the DFB device by using either 1) an asymmetric bias configuration or 2) an external optical feedback stabilization under uniform pumping

conditions. Finally, it is suggested that the combination of both techniques while taking the advantage of unique characteristics of the QD gain media can further optimize the performance of the two-section QD DFB laser as a continuous-wave (CW) THz source by purifying and stabilizing the two-color operation in a well controlled manner.

4.3   DFB Device Structure, Fabrication and Characterization

In both index-guided and gain-guided DFB devices the grating structure is incorporated into the laser waveguide such that the emission wavelength is determined by the effective refractive index of the active material and the grating pitch size. These two DFB structures require at least two growth steps that often are complicated and have very low yield. In the LLC-DFB processing technique, a metal grating is patterned lateral to a narrow ridge-waveguide (RWG) that couples to the evanescent part of the guided mode. It is important to note that the LLC–DFB device structure has the advantages of a gain-coupled device without requiring re-growth, which makes this approach applicable to all material systems. In 1999, Kamp *et. al*, developed a complex LLC-DFB laser emitting at 980 nm based on a single layer of InGaAs/GaAs QD [28]. A threshold current of 14 mA, and a side-mode suppression ratio (SMSR) of > 50 dB was obtained in these devices [28]. Previous studies reported only a small penalty in threshold current and efficiency due to the metal absorption in the DFB lasers fabricated by this method [29]. The resulting gain coupling coefficients in these DFB devices were estimated to be around 5-20 cm^{-1} which was found to be sufficient for a stable single-mode operation [28]. The LLC-DFB devices studied in this dissertation were fabricated by using similar processing techniques. The QD laser material (wafer# ZLG-560) was grown and provided by Zia

161

Laser, Inc. The QD LLC-DFB device processing steps are presented in the following section.

4.3.1   InAs/InGaAs QD Structure and Fabrication

The epitaxial structure and two-section waveguide design are schematically shown in Figure (4.1a). The InAs/InGaAs dots-in-a-well (DWELL) laser structure was grown by elemental source molecular beam epitaxy on a (001) n^+-GaAs substrate. The active region consists of six stacks of InAs QDs embedded in $In_{0.15}Ga_{0.85}As$ QWs each separated by undoped GaAs barrier layers. The upper and lower cladding layers were 1.30 µm thick $Al_{0.66}Ga_{0.34}As$. Before starting the fabrication, the grown laser structures were first characterized by making broad area lasers in order to evaluate the laser material performance as well as peak gain wavelength which was later used to calculate the grating pitch size. Room temperature photoluminescence (PL) measurements show that the QD material has a nominal GS lasing around 1240 nm.

The flow chart of the LLC DFB processing procedure for the two-section DFB laser is shown in Figure (4.1b). The device fabrication starts with formation of 3-4 µm wide ridge-waveguides defined by standard contact photolithography and etched by the inductively coupled plasma (ICP) etching technique. The ridges were etched down to a distance of 150-200 nm above the cladding/core waveguide boundary. Exact control of the etch depth is critical, since the coupling strongly depends on the distance between the core and the grating. Usually higher etch depths provides better wavelength control but at the same time it increases the threshold of the device due to the presence of the metal grating and its loss at infrared wavelengths.
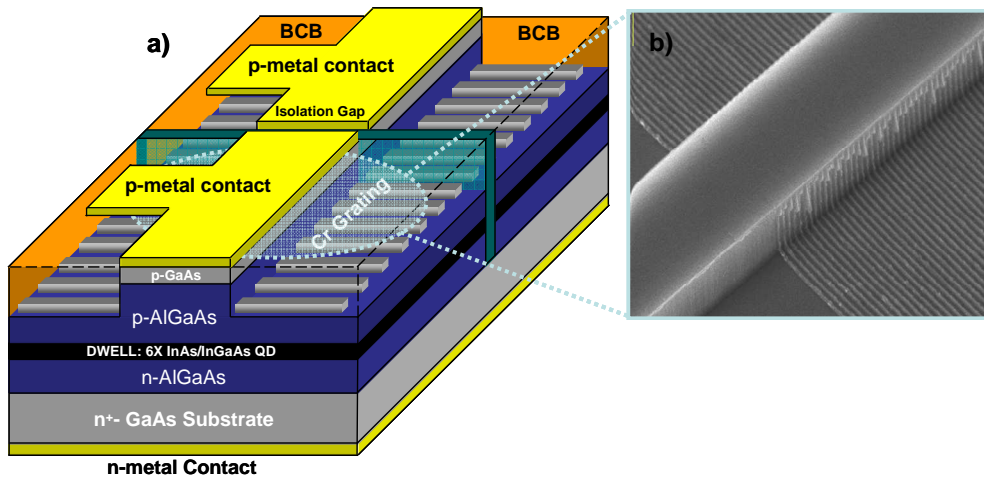
Figure (4.1a) Oblique schematic view of the epitaxial layers and two-section cavity structure of the InAs QD LLC-DFB laser. (b) Oblique SEM image of the 100 nm wide chromium grating lines adjacent to the ridge waveguide processed by electron-beam lithography and metal evaporation.
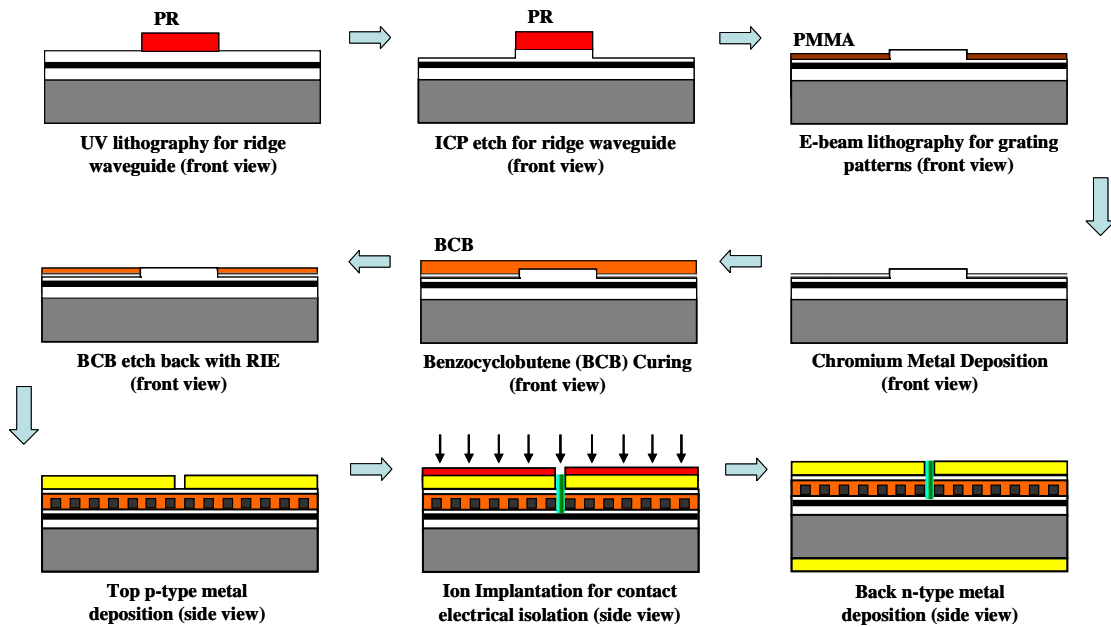
Figure (4.1b) The flow chart of the processing procedure for a two-section LLC DFB laser.

163

As illustrated in Figure (4.1b), the two-section LLC-DFB laser bars were fabricated by patterning 100 nm wide lateral absorptive chromium grating lines adjacent to 3 μm wide ridges using 200 nm thick 495C3 PMMA (Poly Methyl Methacrylate) resist and a JEOL JBX-6300FS electron beam lithography system followed by metal evaporation and liftoff. The first order metal gratings constructed of 25-35 nm thick Cr lines have average pitch sizes of around 190 nm with 50% duty cycle. After surface planarization using benzocyclobutene (BCB), the Ti/Pt/Au layers were deposited to form the p-metal contact. The electrical isolation between the two 500-μm long sections was provided by proton implantation with an isolation resistance of >10 MΩ. Finally, the substrate was lapped and polished, and a Ge/Au/Ni/Au n-metal contact layer was deposited and annealed at ~380 °C. The two-section QD DFB laser was cleaved at both facets and has a total cavity length of 1 mm.

4.3.2 LLC-DFB Device Light-Current Characteristics

Figure (4.2a) represents the light-current characteristic, L(I), measured under uniform pumping and at room temperature. When the two laser sections are uniformly biased, the QD ES begins lasing with a threshold current density of ~3000 A/cm^2, and the device has single-mode emission at 1193 nm with a strong SMSR > 40 dB as illustrated in Figure (4.2a). The slope efficiency reported here is 0.12 mW/mA and values as high as 0.24 mW/mA have been reported for LLC-DFB lasers [3]. Asymmetric HR/HR coating of the laser facets while maintaining the DFB operation can significantly improve the power performance of the device. Although there is no obvious stop band observed in the spectra, the side-modes around 1 nm away from the lasing mode might be due to the
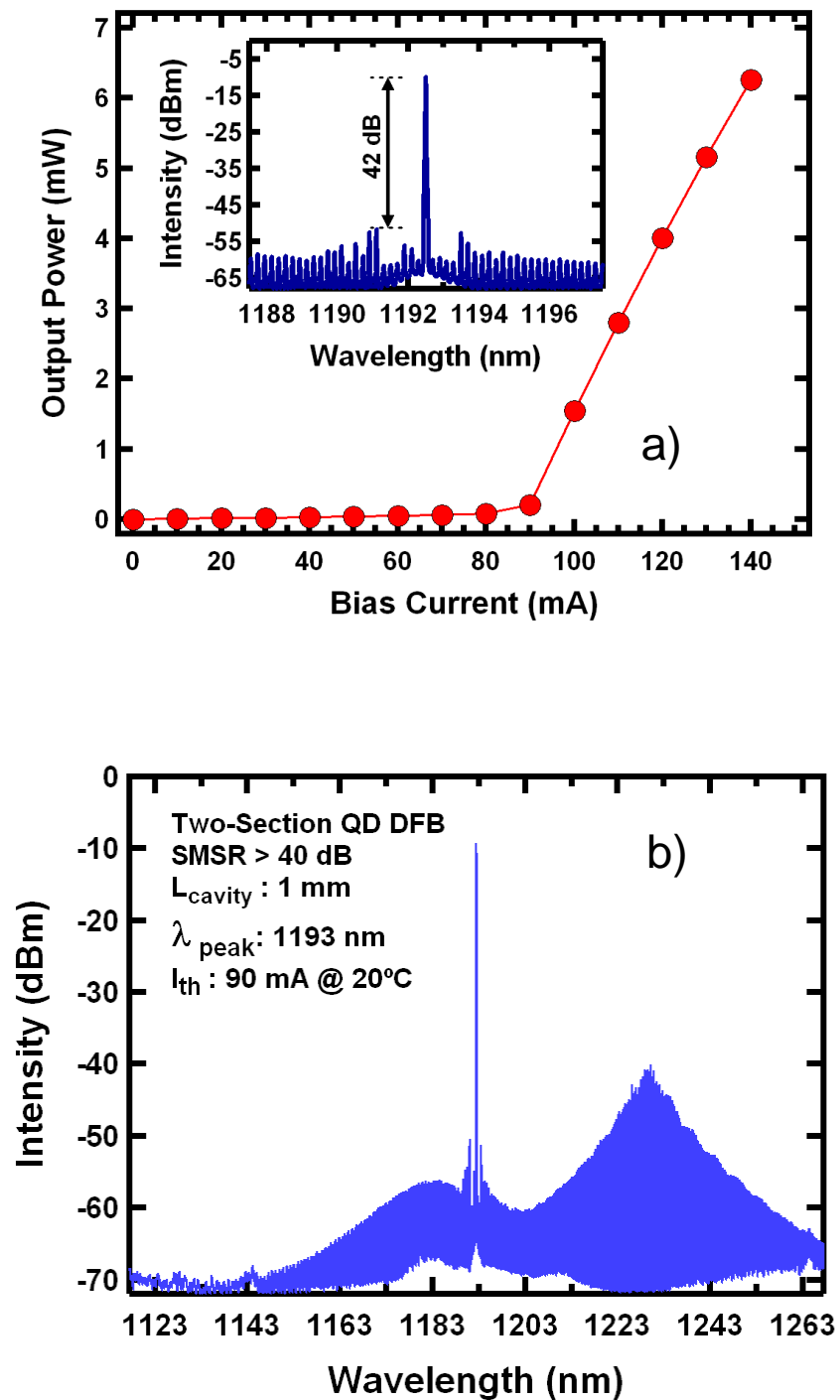
Figure (4.2)(a)Room temperature Light-Current characteristics of the two-section QD DFB laser. The inset figure shows the optical spectrum of the solitary laser at 110 mA with a side-mode suppression ratio of > 40 dB. (b) Broad optical spectrum of the two-section DFB laser at 110 mA indicating the existence of the ES and GS peaks under uniform pumping conditions.

165

residual index coupling of the Chromium metal grating. Figure (4.2b), which is the above threshold and wide-span spectra under uniform pumping condition of 90 mA, illustrates the strongly-coupled ES emission peak about 40 nm apart and 30 dB above the broad Fabry-Perot (FP) GS peak.

The temperature shift of the DFB mode was measured to be around 0.1 nm/°C, which agrees with the wavelength shift rate reported for the thermal effect on the refractive index in GaAs based materials [30]. The QD gain peak was found to shift at a rate of ~0.16 nm/°C, which indicates that QD DFB devices have a wider range of temperature tuning compared to QWs [31]. The detailed study of the temperature performance of the QD material used in this work can be found in [30].

4.3.3 Evaluation of the Coupling Coefficient in the LLC-DFB Laser

The κ-value, or the coupling coefficient, is an important design parameter in evaluating the performance of any type of DFB laser. The complex coupling coefficient is described by:

$$\kappa = \kappa_{index} + i\kappa_{gain} = \tilde{\kappa}e^{i\theta} \qquad (4.1)$$

where κ_{index} and κ_{gain} are the index coupling and gain coupling coefficients, respectively. The mixture of index and gain coupling is described by the phase, θ, at a given coupling strength, $\tilde{\kappa}L$ (where L is the cavity length). Besides the evaluation of the coupling coefficient, the spatial phase of the grating at the front and back facets should also be determined since they affect the laser performance. The previous methods used for calculating the coupling coefficient in conventional DFB structures with embedded gratings involve approximations which are no longer valid in RWG LLC-DFB structures

and the few available methods for gain-coupled DFB lasers are very complicated [32]. Therefore, in this work an improved computer-based program called LAPAREX (Laser Parameter Extraction) developed by T. Nakura *et. al.* at the University of Tokyo was used to predict the κ-value of the device under investigation [33]. This program enables a predictive calculation of the coupling coefficient for both the gain and index-coupled DFB structures through numerical least-squares-fitting of the measured sub-threshold spectrum with a theoretical sub-threshold fitting algorithm derived from static coupled-mode equations [33]. The fitting function consists of 13 fitting parameters, three of which need to be separately determined and kept constant during the curve fitting. The fixed parameters are known from the device geometry and DFB design parameters, including the cavity length, L, grating period, Λ, and front and back facet reflectivities, R_f and R_b, respectively. The freely varying fitting parameters reduce to κ_{index} and κ_{gain}, front (θ_f) and back (θ_b) facet phases, the net peak gain (g), the effective refractive index (n_{eff}), and the index dispersion ($dn/d\lambda$) that can be separately extracted. The least-squares fitting algorithm starts with determining the initial guess values for freely varying fitting parameters from known device parameters such as cavity length, grating period, and facet reflectivities as described in [33]. The initial guess values are very important since they can be compared to the final extracted values to determine the reliability of curve-fitting results.

Sub-threshold spectra measured from a 1-mm long two-section QD LLC-DFB device uniformly biased at 60 mA and 70 mA along with the curve fitting results are shown in Figure (4.3) and Figure (4.4). The DFB device has a first-order grating, a cavity length of L= 1 mm, a grating period of Λ = 190 nm, and front and back facet reflectivities

167
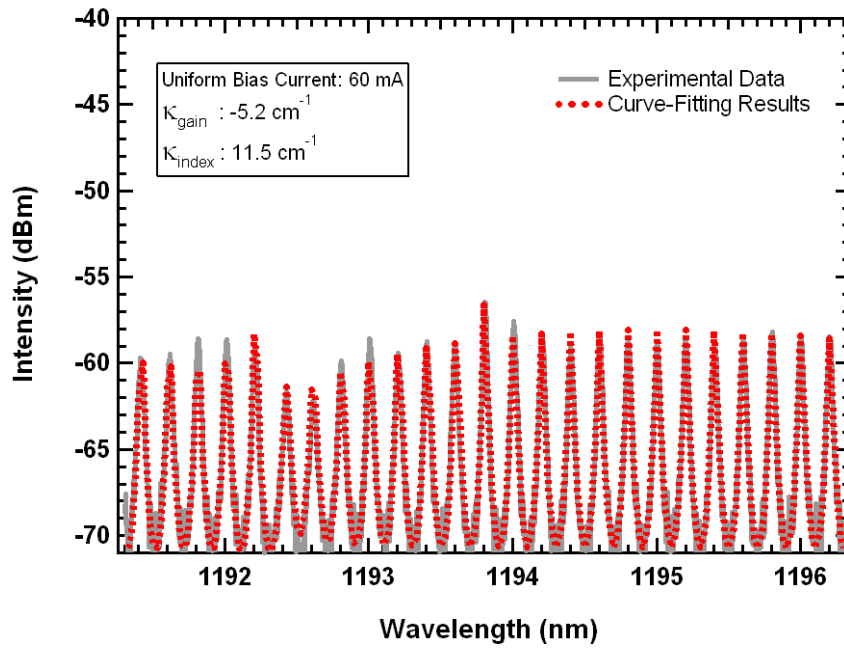
Figure (4.3) Sub-threshold spectra of the two-section LLC DFB laser biased uniformly at 60 mA.
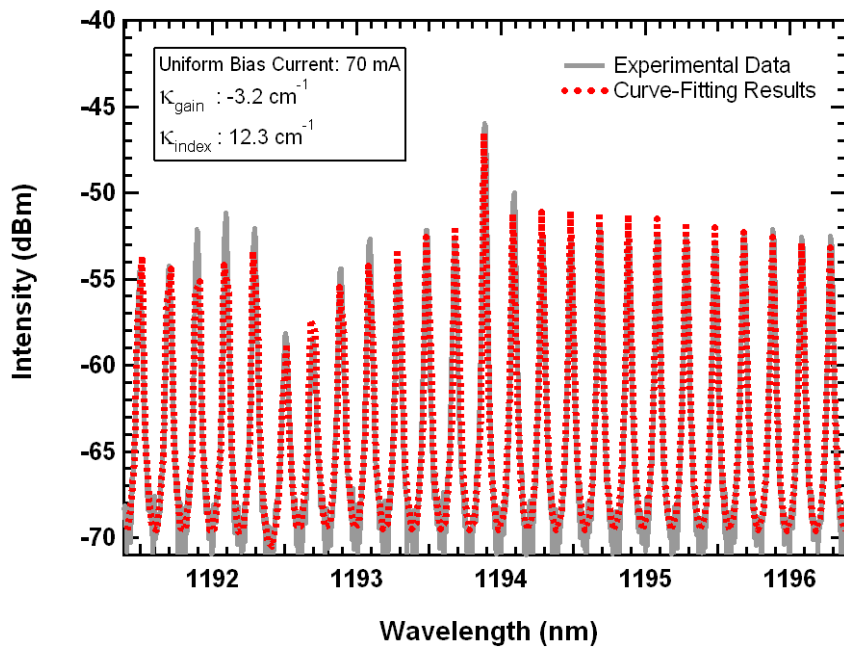
Figure (4.4) Sub-threshold spectra of the two-section LLC DFB laser biased uniformly at 70 mA.

of $R_f = R_b = 32\%$. These parameters were kept constant during the curve-fitting. Extracted values for the front and back facet phases, the effective refractive index at the Bragg wavelength, the net peak gain, and the wavelength dispersion of the refractive index at a 70 mA uniform bias current were found to be $\theta_f = -109°$ and $\theta_b = 107°$, $n_{eff} = 3.25$, $g = 1.35$ cm^{-1}, and $dn/d\lambda = -0.23$ μm^{-1}, respectively. The error analyses for the coupling coefficient values are evaluated based on a one standard deviation confidence interval and are observed to be less than 10% of the extracted values.

Least-squares-fitting of the sub-threshold spectra at different uniform bias currents ranging from 60 mA to 70 mA predict a gain coupling coefficient value of $\kappa_{gain} = -5.2$ to -3.2 cm^{-1}, respectively, as shown in Figure (4.5). The negative sign confirms the anti-phase complex coupling condition as indicated in extracted values for facet phases. The results shown in Figure (4.5) for the extracted gain coupling coefficient indicate that the magnitude of κ_{gain} reduces with increased bias current which is due to the saturation of the Cr grating absorption coefficient at higher photon densities [33].

Extracted values of the index coupling coefficient shown in Figure (4.6), indicate that this parameter remains relatively unchanged at $\kappa_{index} = 11.5$ to 12.3 cm^{-1} as the bias current is increased. This is probably due to the fact that since the absorptive grating material has a relatively high refractive index, increased photon absorption has a negligible impact on the refractive index of the grating material in the two-section QD DFB.
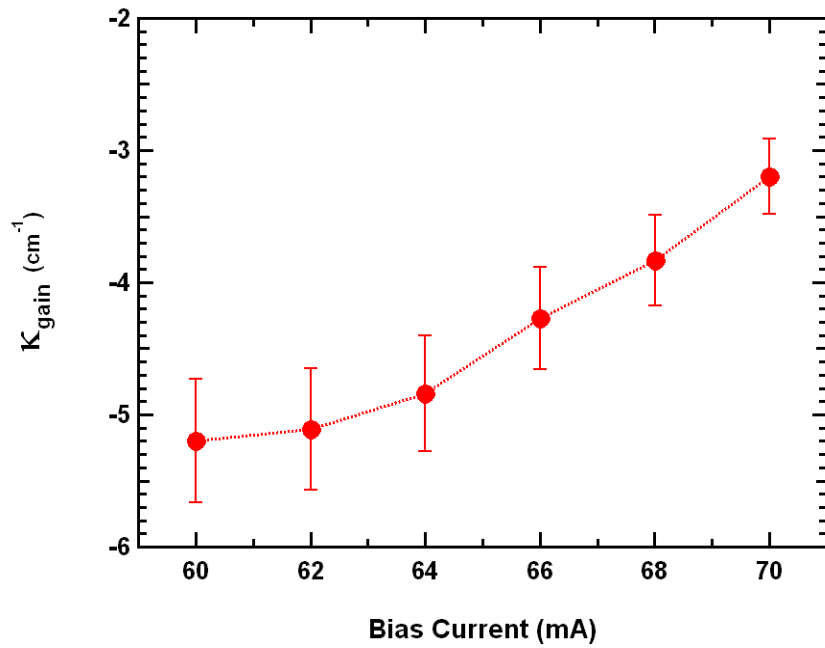
Figure (4.5) Extracted values of the gain coupling coefficient for the LLC DFB laser as a function of uniform bias current ranges from 60 mA -70mA.
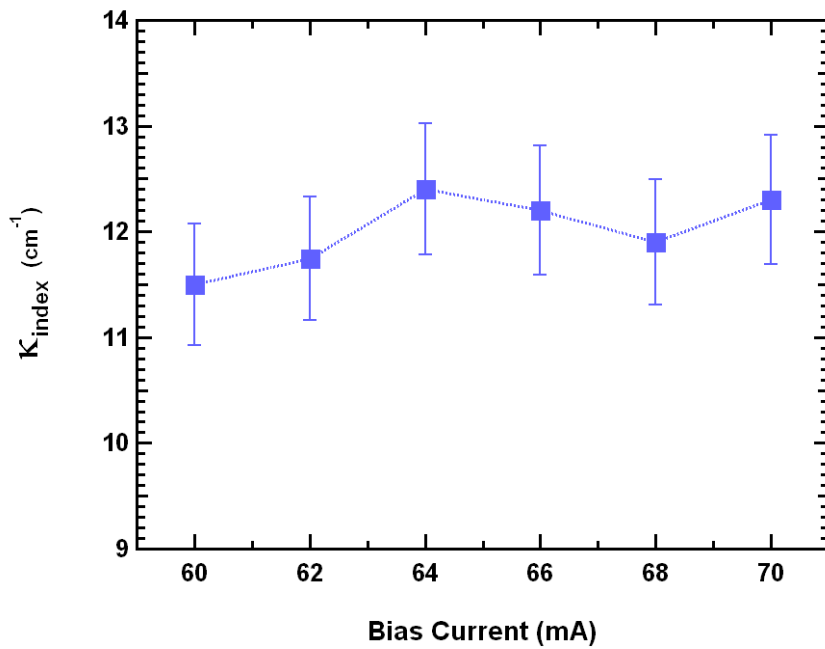
Figure (4.6) Extracted values of the gain coupling coefficient for the LLC DFB laser as a function of uniform bias current ranges from 60 mA -70mA.

170

4.4 Generation of Two-Color Emission through Asymmetric Pumping

Figure (4.7) illustrates the optical spectrum of the two-section DFB under uniform and asymmetric bias conditions. It is shown that under asymmetric pumping conditions, where the two sections were biased at 40 mA and 60 mA, respectively, the powers between the GS and ES modes can be equalized. This phenomenon is mainly attributed to the unique carrier dynamics of the QD active gain medium that provides an ES emission close to the GS level. In addition, the inhomogeneous broadening provided by the QD media is crucial towards achieving the two-color emission in a controllable manner.

As opposed to thin-film QW materials, which are homogeneously broadened, the QD media has a wide spectral bandwidth as a result of an inhomogeneously broadened gain in these materials due to QD size dispersion [34]. Although the variation in dot size is normally an unwanted reality, such broadening, which is significant in QD-based materials, can be leveraged to our benefit and allows for GS excitation. When the two sections are biased asymmetrically, the non-uniform distribution of the carriers shifts the refractive index in the active medium which accordingly alters the contribution of the loss/gain mechanism to the ES level provided by the distributed Bragg reflectors. This result also indicates that the total carrier density is not clamped above the threshold, which again can be explained by inhomogeneity of the gain broadening in QDs [26]. Therefore, the excitation of the GS can be realized by enforcing the non-uniform distribution of carriers and simultaneously taking advantage of the inhomogeneous gain broadening in QD active media. As a result, a two-color laser with, in this case, an 8 THz difference frequency is realized by combining the benefits of a stable ES-coupled emission peak originating from the distributed Bragg reflector mechanism, the

171
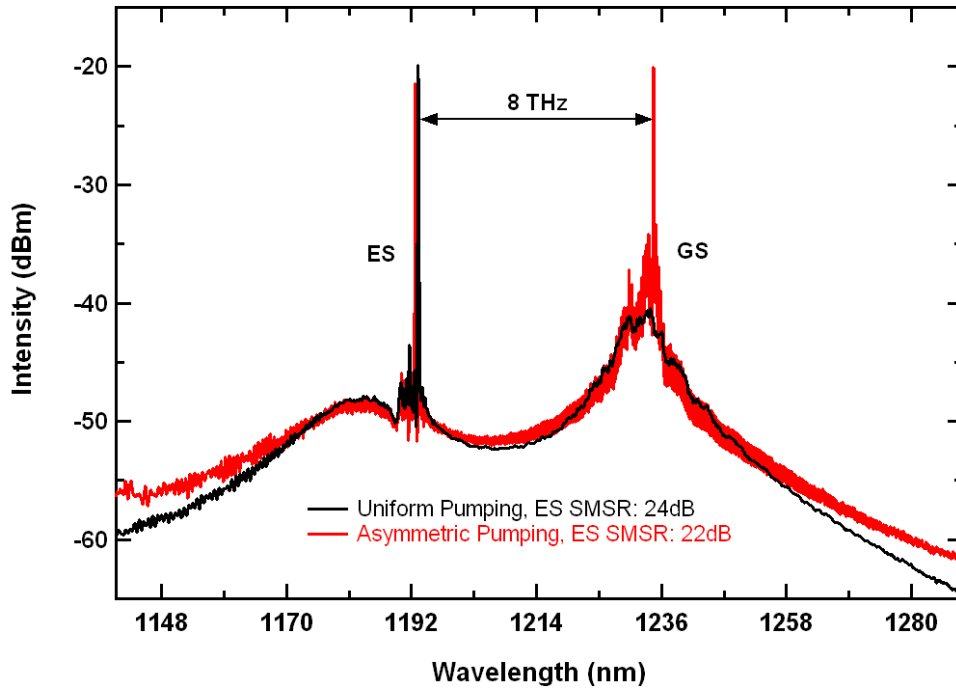
Figure (4.7) Wide-span spectra of the QD DFB laser under uniform and asymmetric bias conditions. Under asymmetric pumping, the SMSR for the GS emission is 14 dB.

inhomogeneous broadening provided by the QD media, and the asymmetric pumping configuration of the two-section laser diode.

It is important to note that depending on the significance of the inhomogeneous broadening in the nanostructure material under consideration, the frequency difference between the two laser modes can be further tuned to the desired value. For instance, the inhomogeneous broadening in the InAs/GaAs QD laser systems is typically around 40 meV to 50 meV, yet for InAs/InP QD based material it can be as large as 70 meV at room temperature [35]. As a result, a smaller energy separation of ~30 meV between the GS and the ES emissions and consequently smaller difference frequency can be obtained in the InAs/InP material system as opposed to the InAs/GaAs QD materials which have a

172

larger GS and ES energy separation of ~70 meV. Therefore when choosing the appropriate material system for the THz generation source, the magnitude of the inhomogeneous broadening which is a unique signature of the nanostructures can be further taken into the account as an alternative design consideration.

4.5 Generation of Two-Color Emission through Applying External Optical Feedback

Remarkably, it was demonstrated that under uniform bias condition, the external optical feedback can trigger the GS emission while the excited state remains unchanged. Figure (4.8) shows the optical spectra measured at 110 mA under uniform pumping in the presence of external optical feedback. The experimental setup used to provide optical feedback to the laser was based on a four-port Polarization-Maintained (PM), 50/50 fiber coupler as schematically illustrated in Figure (4.9). The DFB laser output light was injected into port 1 of the coupler using a PM lensed fiber. The optical feedback was created by an external cavity through a high-reflectivity coated fiber connected to port 2 of the coupler. The applied external feedback level was controlled via a fiber-based variable optical attenuator (VOA) and its value was determined by measuring the output power at port 4. The impact of the external optical feedback on the above threshold spectra was analyzed at port 3 of the fiber coupler via an optical spectrum analyzer (OSA) with a frequency resolution of 2.1 GHz. An optical polarization controller (PC) unit was used to adjust the external feedback beam polarization to be identical to that of the emitted light to maximize the feedback effects. In order to enforce the mode stability, the two-section DFB device was epoxy-mounted on a heat sink and the temperature was maintained at 20 $^{\circ}$C. The coupling loss was calculated to be about 4 dB and was carefully monitored and kept constant throughout the entire measurement. Figure (4.8) shows that as the feedback level is increased from the lowest value (-50 dB) to the highest (-25 dB), the GS FP emission is enhanced and narrowed. Most notably, optical feedback does not affect the ES DFB emission peak located at 1193 nm. The lasing peak is similar to the

174
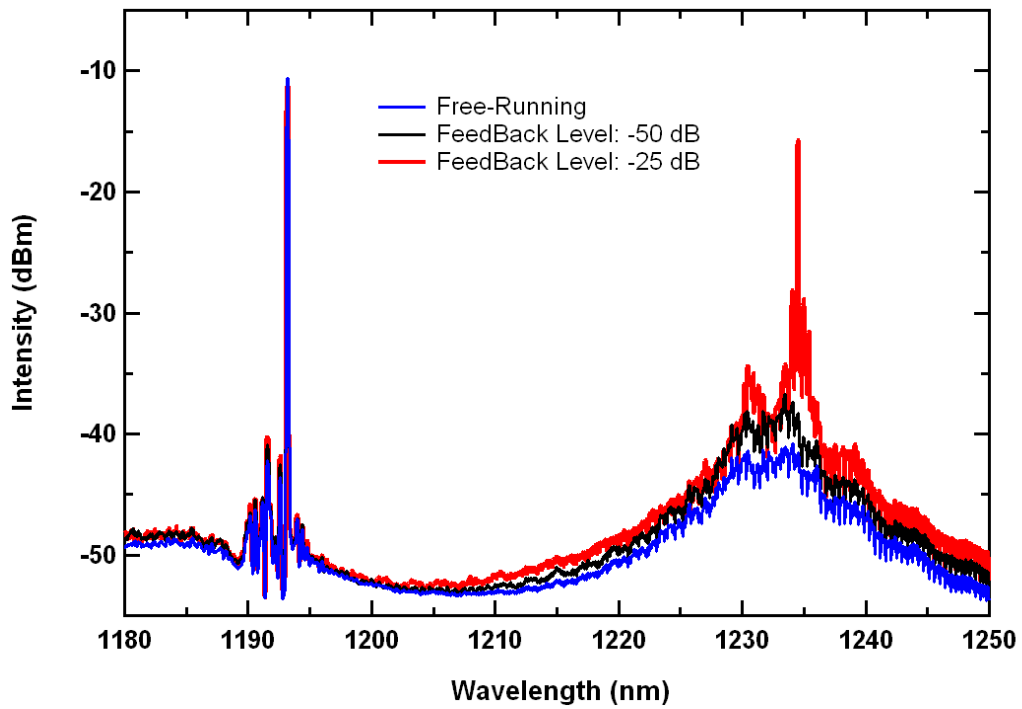
Figure (4.8) Broad optical spectra at uniform bias of 110 mA under free-running (no feedback) and external optical feedback level ranges from -50 dB to -25 dB.
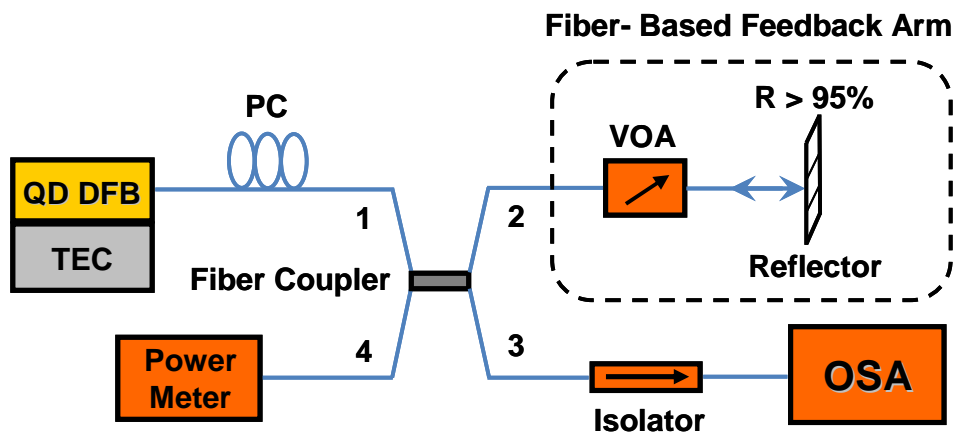
Figure (4.9) Schematic diagram of the experimental optical feedback setup.

solitary laser and remains stable even under the strongest feedback level. This robustness of the ES emission is attributed to the existence of a larger photon density in the cavity provided by the ES coupling through the absorptive metal grating. Similar to the case of asymmetric bias configuration in the two-section QD DFB, the inhomogeneous broadening provided by the QD media helps to reach the two-color emission. Such a broadening when properly combined with external optical feedback permits the excitation and narrowing of the GS emission.

It is important to note that no significant evidence of linewidth broadening or coherence collapse was observed in the ES mode over the entire range of applied feedback levels. This finding confirms that the ES emission on the QD DFB is less sensitive to external reflections as was recently demonstrated in similar QD material system [36]. Such a solid feedback resistivity might be due to the smaller value of the linewidth enhancement factor in the ES emission which is expected to assist in improving the laser's stability under the influence of external optical feedback [37, 38].

4.6 Chapter 4 References

[1]   N. Kirstaedter, N. N. Ledentsov, M. Grundmann, D. Bimberg, V. M. Ustinov, S. S. Ruvimov, M. V. Maximov, P. S. Kopev, Z. I. Alferov, U. Richter, P. Werner, U. Gosele, and J. Heydenreich, "Low-threshold, large T_0 injection-laser emission from (InGa)As quantum dots," *Electronics Letters*, Vol. 30, No. (17), pp. 1416-1417, (1994).

[2]   N. N. Ledentsov, V. M. Ustinov, A. Y. Egorov, A. E. Zhukov, M. V. Maksimov, I. G. Tabatadze, P. S. Kopev, "Optical properties of heterostructures with InGaAs-GaAs quantum clusters," *Semiconductors*, Vol. 28, No. (8), pp. 832-834, (1994).

[3]   H. Su, and L. F. Lester, "Dynamic properties of quantum dot distributed feedback lasers: high speed, linewidth and chirp," *Journal of Physics D: Applied Physics*, Vol. 38, No. (13), pp. 2112–2118, (2005).

[4]   M. Koch, "Terahertz Communications: A 2020 Vision," in *Terahertz Frequency Detection and Identification of Materials and Objects*, R. E. Miles, X. –C. Zhang, H. Eisele, A. Krotkus, eds. (Springer, New York, 2007).

[5]   P. H. Siegel, "Terahertz technology in biology and medicine," *IEEE Transactions on Microwave Theory and Techniques*, Vol. 52, No. (10), pp. 2438–2447, (2004).

[6]   P. F. Taday, "Applications of terahertz spectroscopy to pharmaceutical sciences," *Philosophical Transactions of the Royal Society of London A.*, Vol. 362, No. (1815), pp. 351–364, (2004).

[7]   S. Wang, B. Ferguson, D. Abbott, and X.-C. Zhang, "T-ray imaging and tomography," *Journal of Biological Physics*, Vol. 29, No. (2), pp. 247–256, (2003).

[8]   C. Baker, T. Lo, W. R. Tribe, B. E. Cole, M. R. Hogbin, and M. C. Kemp, "Detection of concealed explosives at a distance using terahertz technology," *In proceedings of IEEE on T-Ray Imaging, Sensing, and Retection*, (Institute of Electrical and Electronics Engineers, New York, 2007), pp. 1559–1565.

[9]   D. Saeedkia, and S. Safavi-Naeini, "Terahertz photonics: optoelectronic techniques for generation and detection of terahertz waves," *IEEE Journal of Lightwave Technology*, Vol. 26, No. (15), pp. 2409–2423, (2008).

[10]   A. Klehr, J. Fricke, A. Knauer, G. Erbert, M. Walther, R. Wilk, M. Mikulics, and M. Koch, "High-power monolithic two-mode DFB laser diodes for the generation of THz radiation," *IEEE Journal of Selected Topics in Quantum Electronics*, Vol. 14, No. (2), pp. 289–294, (2008).

[11]   M. Tani, O. Morikawa, S. Matsuura, and M. Hangyo, "Generation of terahertz radiation by photomixing with dual- and multiple-mode lasers," *Semiconductor Science and Technology*, Vol. 20, No. (7), pp. S151–S163, (2005).

[12]   M. Naftaly, M. R. Stone, A. Malcoci, R. E. Miles, and I. C. Mayorga, "Generation of continuous-wave terahertz radiation using two-color laser with Fabry-Perot etalon," *Electronics Letters*, vol. 41, No. (3), pp. 128–129, (2005).

[13]   L. F. Lester, K. C. Hwang, P. Ho, J. Mazurowski, J. M. Ballingall, J. Sutliff, S. Gupta, J. Whitaker, and S. L. Williamson, "Ultra-fast long-wavelength photodetectors fabricated on low-temperature InGaAs on GaAs," *IEEE Photonics Technology Letters*, Vol. 5, No. (5), pp. 511–514, (1993).

[14] E. R. Brown, "THz generation by photomixing in ultrafast photoconductors," *International Journal of High Speed Electronics and Systems*, Vol. 13, No. (2), pp. 497–545, (2003).

[15] K. A. McIntosh, E. R. Brown, K. B. Nichols, O. B. McMahon, W. F. DiNatale, and T. M. Lyszczarz, "Terahertz measurements of resonant planar antennas coupled to low-temperature-grown GaAs photomixers," *Applied Physics Letters*, Vol. 69, No. (24), pp. 3632–3634, (1996).

[16] J. C. Pearson, K. A. McIntosh, and S. Verghese, *Long-Wavelength Infrared Semiconductor Lasers* (John Wiley & Sons, 2005), Chap. 7.

[17] C. -L. Wang and C. -L. Pan, "Tunable multiterahertz beat signal generation from a two-wavelength laser-diode array," *Optics Letters*, Vol. 20, No. (11), pp. 1292–1294, (1995).

[18] P. Pellandini, R. P. Stanley, R. Houdrè, U. Oesterle, M. Ilegems, and C. Weisbuch, "Dual-wavelength laser emission from a coupled semiconductor microcavity," *Applied Physics Letters*, Vol. 71, No. (7), pp. 864-866, (1997).

[19] M. Hofmann, E. Bründermann, M. Havenith, M. Matus, J. V. Moloney, A. S. Moskalenko, M. Kira, S. W. Koch, S. Saito, and K. Sakai, "Fourwave mixing and direct terahertz emission with two-color semiconductor lasers," *Applied Physics Letters*, Vol. 84, No. (18), pp. 3585–3587, (2004).

[20] S. Zolotovskaya, V. I. Smirnov, G. B. Venus, L. B. Glebov, and E. U. Rafailov, "Two-color output from InGaAs laser with multiplexed reflective Bragg mirror," *IEEE Photonics Technology Letters*, vol. 21, No. (15), pp. 1093-1095, (2009).

[21] M. Hyodo, M. Tani, S. Matsuura, N. Onodera, and K. Sakai, "Generation of millimeter-wave radiation using a dual-longitudinal-mode microchip laser," *Electronics Letters*, Vol. 32, No. (17), pp. 1589–1591, (1996).

[22] P. Bhattacharya, D. Klotzkin, O. Qasaimeh, W. Zhou, S. Krishna, and D. Zhu, "High-speed modulation and switching characteristics of In(Ga)As–Al(Ga)As self-organized quantum-dot lasers," *IEEE Journal of Selected Topics in Quantum Electronics*, Vol. 6, No. (3), pp. 426–438, (2000).

[23] A. Stintz, G. T. Liu, H. Li, L. F. Lester, and K. J. Malloy, "Low threshold current density 1.3μm InAs quantum dot lasers with the dots-in-a-well structure," *IEEE Photonics Technology Letters*, Vol. 12, No. (6), pp. 591-593, (2000).

[24] T. C. Newell, D. J. Bossert, A. Stintz, B. Fuchs, K. J. Malloy, and L. F. Lester, "Gain and linewidth enhancement factor in InAs QD laser diodes," *IEEE Photonics Technology Letters*, Vol. 11, No. (12), pp. 1527-1529, (1999).

[25] C. Y. Jin, H. Y. Liu, T. J. Badcock, K. M. Groom, M. Gutiérrez, R. Royce, M. Hopkinson, and D. J. Mowbray, "High-performance 1.3-μm InAs/GaAs quantum-dot lasers with low threshold current and negative characteristic temperature," *In proceedings of the IEE Optoelectronics*, Vol. 153, No. (6), pp. 280–283, (2006).

[26] A. Markus, J. X. Chen, C. Paranthoën, and A. Fiore, "Simultaneous two-state lasing in quantum-dot lasers," *Applied Physics Letters*, Vol. 82, No. (12), pp. 1818-1820, (2003).

[27] M. A. Cataluna, D. I. Nikitichev, S. Mikroulis, H. Simos, C. Simos, C. Mesaritakis, D. Syvridis, I. Krestnikov, D. Livshits, and E. U. Rafailov, "Dual-wavelength mode-locked quantum-dot laser, via ground and excited state

transitions: experimental and theoretical investigation," *Optics Express*, Vol. 18, No. (12), pp. 12832-12838, (2010).

[28] M. Kamp, J. Hofmann, F. Schafer, M. Reinhard, M. Fischer, T. Bleuel, J. P. Reithmaier, and A. Forchel, "Lateral coupling -a material independent way to complex coupled DFB lasers," *Optical Materials*, Vol. 17, No. (1), pp. 19–25, (2001).

[29] S. Kuen, and C. Liew, "Above-threshold analysis of loss-coupled DFB lasers: threshold current and power efficiency," *IEEE Photonics Technology Letters*, Vol. 7, No. (12), pp. 1400-1402, (1995).

[30] L. Zhang, R. Wang, Z. Zou, T. Newell, D. Webb, P. Varangis, and L. F. Lester, "InAs quantum dot DFB lasers on GaAs for uncooled 1310nm fiber communications," *In proceedings of Optical Fiber Communication Conference* in Atlanta, GA., (2003).

[31] M. Kamp, M. Schmitt, J. Hofmann, F. Schafer, J. P. Reithmaier, and A. Forchel, "InGaAs/AlGaAs quantum dot DFB lasers operating up to 213 degrees C," *Electronics Letters*, Vol. 35, No. (23), pp. 2036-2037 (1999).

[32] D. M. Adams, D. T. Cassidy, and D. M. Bruce, "Scanning photoluminescence technique to determine the phase of the grating at the facets of gain-coupled DFB's," *IEEE Journal of Quantum Electronics*, Vol. 32, No. (7), pp. 1237-1242 (1996).

[33] T. Nakura, Y. Nakano, "LAPAREX-An automatic parameter extraction program for gain- and index-coupled distributed feedback semiconductor lasers, and its

application to observation of changing coupling coefficients with currents," *IEICE Transactions on Electronics*, Vol. 83, No. (3), pp. 488-495, (2000).

[34] P. Bhattacharya, "Lasers: structures and properties" in *Semiconductor Optoelectronic Devices*, E. Svendsen, R. Kernan, P. Daly, eds. (Prentice Hall, Upper saddle river, NJ, 1994).

[35] F. Grillot, K. Veselinov, M. Gioannini, I. Montrosset, J. Even, R. Piron, E. Homeyer, S. Loualiche, "Spectral analysis of 1.55-μm InAs/InP (113)B quantum-dot lasers based on a multipopulation rate equations model," *IEEE Journal of Quantum Electronics*, Vol. 45, No. (7), pp. 872-978, (2009).

[36] C. Mesaritakis, C. Simos, H. Simos, S. Mikroulis, I. Krestnikov, E. Roditi, and D. Syvridis, "Effect of optical feedback to the ground and excited state emission of a passively mode locked quantum dot laser," *Applied Physics Letters*, Vol. 97, No. (6), pp. 061114, (2010).

[37] F. Grillot, N. A. Naderi, M. Pochet, C.-Y. Lin and L. F. Lester, "Variation of the feedback sensitivity in a 1.55μm InAs/InP quantum-dash Fabry-Perot semiconductor laser," *Applied Physics Letters*, Vol. 93, No. (19), pp. 191108, (2008).

[38] F. Grillot, N. A. Naderi, M. Pochet, C.-Y. Lin, P. Besnard and L. F. Lester, "Tuning of the critical feedback level in 1.55-μm quantum dash semiconductor laser diodes," *IET Optoelectronics*, Vol. 3, No. (6), pp. 242-247, (2009).

182

Chapter 5

Conclusions and Future Research

5.1 Summary and Conclusion

This dissertation studied the impacts of external control techniques of optical injection-locking, optical feedback, and asymmetric pumping on the performance of nanostructure QD and QDash lasers. Explicitly this study focused on optimizing the solitary laser's intrinsic parameters through externally controlled perturbations. Consequently the overall impacts of this optimization on the dynamical performance of a laser system's direct modulation and spectral characteristics are investigated for different nanostructure structures.

First, external control via optical injection is investigated by primarily focusing on modeling the injection-locked behavior of a nanostructure laser system under direct modulation. Knowing the key operating parameters of the injection-locked system gives a better understanding of the underlying physics and can be further used to optimize the high-speed modulation performance of such a coupled system. Using a small-signal analysis of three coupled rate equations describing an injection-locked system, a novel modulation response function is demonstrated which successfully models the key operating parameters of the system [1]. It is shown that the model implicitly incorporates nonlinear gain through the relaxation oscillation frequency and damping rate of the free-running slave laser. The impact of gain compression is evaluated for the slave device by

examining the variation of the square of the relaxation oscillation frequency as a function of output power. The presented model can be used to confidently extract microwave characteristics and operating parameters of the injection-locked system by reducing the number of fitting parameters and providing acceptable physical constraints to the remaining fitting terms. This eliminates the reliance on curve-fitting schemes to fully calculate all of the operating parameters and leads to more accurate extracted parameters.

Using this model, the characteristic parameters of an injection-locked system were extracted for a QDash FP slave laser from experimentally collected response data for varied levels of frequency detuning. Under the zero-detuning condition, a three-fold improvement in 3-dB modulation bandwidth compared to the free-running case was observed for the QDash laser under investigation. The validity of the model was examined based on the extracted value's correlation with theoretically expected values. The extracted parameters included the maximum injection ratio, linewidth enhancement factor, and threshold gain shift. As opposed to previous work which primarily focuses on analyzing experimental data in the spectral domain [2]-[5], this model demonstrates that reliable curve-fitting results can be generated when operating in the microwave domain. In addition, the model not only showed how the linewidth enhancement factor, damping rate, and free-running oscillation impacted the observed pre-resonance dip at the positive frequency detuning edge, but indicated how the dip can be virtually eliminated in a QDash FP laser by either increasing the slave bias current or reducing the device temperature [1], [6]. More specifically, eliminating the pre-resonance dip by manipulating the linewidth enhancement factor is found to further enhance the 3-dB modulation bandwidth up to 4X compared to the free-running case. Thus, the injection-

locked QDash laser system can be controlled such that it is suitable for large bandwidth applications.

Next, the high-speed modulation characteristics of an injection-locked QD FP laser under strong injection are investigated experimentally with a focus on optimizing the broadband modulation responses and enhancing the 3-dB modulation bandwidth [7]. It is found that the QD FP device has a unique modulation response that is characterized by a rapid low frequency rise along with a slightly slower parasitic decay rate (compared to the free-running response) that enhances the 3-dB bandwidth of the coupled system up to 8X compared to the free-running case at the expense of losing modulation efficiency of about 20 dB at low frequencies. Similarly, using the predictive modulation response function, the key operating parameters of the QD device under strong injection were directly extracted by performing a least squares fit of the experimental data. The extracted values were found to be in a good agreement with theory which proved that the response model is a reliable method to extract the key operating parameters of the observed unique response in the microwave domain. Comparing the extracted values of linewidth enhancement factor under strong injection-locking to the measured free-running value, a significant decrease from 2 to -0.16 is identified; this finding indicates that the QD FP laser's linewidth enhancement factor can be manipulated by optical injection to near zero or even negative values. The unique broadband responses, along with their associated small linewidth enhancement factor observed in this work show that the injection-locked QD FP lasers has the potential to be optimized as an integrated high-speed photonic transmitter to be used in future high performance RF optical links.

As a companion study, the manipulation of the linewidth enhancement factor of an injection-locked QDash laser system at zero-detuning and under strong optical injection was also investigated [8]. Using the amplified spontaneous emission technique, the QDash material properties, including the net modal gain profile and below threshold linewidth enhancement factor, are separately measured as a function of wavelength and current density. From the slave laser's measured net modal gain profile, an optimum free-running operating point is identified at which the linewidth enhancement factor is expected to be manipulated to the lowest possible values using strong optical injection. The injection-locked QDash laser's above threshold linewidth enhancement factor was directly measured as the injected optical power is varied using the FM/AM technique. For comparison, the injection-locked QDash linewidth enhancement factor and corresponding threshold gain shifts for varied injection strengths were separately extracted from measured microwave data using a simplified form of the modulation response function at the zero-detuning condition. The extracted linewidth enhancement factor values from the curve fits are found to be within experimental error from the measured values using the FM/AM technique. The experimental findings verify that the QDash linewidth enhancement factor can be manipulated down to near zero values through the threshold gain shift as a result of strong optical injection. As a result of this manipulation, a linewidth enhancement factor value of 0.0 ($\pm$ 0.25) was directly measured from FM/AM measurements and a value of 0.001 ($\pm$ 0.8) was separately obtained from simulation which corresponds to a threshold gain shift of 24.6 cm^{-1} at zero-detuning and a 9.3 dB injected external power ratio. From an application prospective, measured near zero linewidth enhancement factors along with the enhanced bandwidth advantages offered in

the direct modulation of injection-locked QDash laser devices are promising for implementation in transmitter modules driving future long-haul and high-speed optical fiber links.

Unrelated to the optical injection-locking work discussed previously, asymmetric pumping and an external optical feedback were both used to demonstrate dual-color operation in a single QD laser by simultaneously generating two single-mode emission peaks–one line from the ground state and the other from the excited state of the QD device [9]. An 8 THz frequency difference is realized by applying two different external control techniques in a two-section laterally loss coupled QD DFB laser with a strongly coupled excited state emission.

As a first step in this study, the absorptive grating coupling strength values of the DFB device, specifically the gain and index coupling coefficients, were determined using a least squares fitting method of the sub threshold spectra. The extracted values for the gain coupling coefficient from least squares fitting method was found to be between -5.2 to -3.2 cm^{-1} as the bias current was increased from 60 mA to 70 mA, respectively. It was also shown that the index coupling coefficient remains relatively constant at 11.5 to 12.3 cm^{-1} for the same bias range.

It was found that when the DFB laser is biased above threshold, the excited state emission can be relatively stable while the ground state emission is excited and narrowed via either asymmetric pumping of the two-sections or by applying an external feedback. Under asymmetric bias conditions, the powers of the ground state and excited state modes of the two-section device can be made equal, which is mainly attributed to the unique carrier dynamics of the QD gain medium. It is also shown that the combination of

significant inhomogeneous broadening and an excited state coupled mode operation allows the manipulation of the QD states through external optical stabilization. These findings suggest that the combination of both external control techniques can further optimize the performance of the two-section QD DFB laser as a compact and low cost CW THz source by purifying and stabilizing the dual-color operation in a well controlled manner.

5.2   Proposed Future Research

The interesting and novel results found within this investigation have created several new research ideas for the future work. A full investigation on the manipulation of the linewidth enhancement factor in semiconductor nanostructure lasers through optical injection can be further extended to other types of nanostructure material systems including QD lasers that have a highly variable phase-amplitude coupling factor [7]. Also previously discussed was the idea that the QD laser's linewidth enhancement factor can be externally controlled and manipulated to negative values using an optical injection-locking technique. This novel finding is very important since a laser source with a tunable and/or negative linewidth enhancement factor can be implemented in an optical transmitter module enabling integrated chirp compensation mechanism for long-haul optical fiber data transmission links. However, negative linewidth enhancement values cannot be directly measured using the FM/AM technique described in this work and thus it is suggested that a FM/AM phase measurement using a Mach-Zehnder interferometer [10], [11] or a time-resolved frequency chirp measurement technique [12] should be

employed to completely characterize the magnitude and sign of the linewidth enhancement factor in such devices.

In addition, a long term development plan for the injection-locked nanostructure laser architecture should include a fully controllable and compact butterfly packaged device with all the required elements integrated monolithically onto a single chip. Recent efforts on this topic have demonstrated a mutual injection-locking scheme in a two-section QW DFB device by controlling the bias current on each section [13]. However, the proposed design is not capable of fine wavelength tuning and cannot handle sufficiently strong optical injection strengths. One possible approach to creating a proper monolithic master-slave laser integration would be through an HR/AR coated multi-section partial DFB design constructed of a FP modulated gain section as the slave, two grating sections with strong coupling coefficients as the master, and a phase control section. This integration can be further extended to implement other external control techniques such as the optical gain-lever technique to improve the RF gain performance as was previously demonstrated in a bench top scale [14]. Combining all the benefits of directly modulated injection-locked nanostructure lasers, including the enhanced modulation bandwidth along with chirp compensation capabilities in a single integrated design promises a headway towards a compact, chirp-free, and ultrafast (>100 Gb/s) digitally modulated optical transmitter module for future long-haul data links.

In regards to the dual-color operation demonstration, simultaneous combination of the two methods of asymmetric pumping and optical feedback might be beneficial toward stabilizing and purifying the overall operation of the dual-mode emission. One promising way to improve the mode stability is to investigate the impact of weak optical

189

injection on the operation of the dual-color laser source [15]. This combined with an in-depth study of the carrier population in the excited state and ground state of the QD material will improve our understanding of the operational limits and allow for the optimization of this unique laser. In the future, tuning the dual-color emission can be realized through separate design considerations such as fabricating each electronically isolated section with a different grating pitch size and/or optimizing the asymmetric bias configuration. In addition, temperature tuning of the dual-color emissions is possible since the DFB mode and the excited FP mode are each expected to be tuned at slightly different rates with temperature. Furthermore, compared to existing technologies, the design and approach described in this dissertation combined with current chip scale photomixing capabilities [16], [17] have the potential to implement this method to create a single chip coherent THz source. After successful demonstration of a stable and tunable two-color laser source, it would be beneficial to develop an efficient and compact photomixing technique and study the methods to optimize the laser output power and optical-to-electrical efficiency characteristics. The power performance of the two-section DFB device needs to be improved since THz signal generation requires high power laser sources for better conversion efficiency. Several ways of improving the emitted power of the device include, but are not limited to: improving the grating coupling coefficient, AR/HR coating the emitting facets, using a tapered DFB configuration, and by improving the active region gain via optimizing the number of QD stacks and dot density.

With the advancement of this technology, the future of THz generation and detection can be targeted toward a low-cost, compact, and all-on-chip design that can be inserted into, or form the basis for, a variety of commercial products.

5.3 Chapter 5 References

[1]   N. A. Naderi, M. Pochet, F. Grillot, N. B. Terry, V. Kovanis, and L. F. Lester, "Modeling the injection-locked behavior of a quantum dash semiconductor laser," *IEEE Journal of Selected Topics in Quantum Electronics*, Vol. 15, No. (3), pp. 563-571, (2009).

[2]   T. B. Simpson, J. M. Liu, A. Gavrielides, "Bandwidth Enhancement and Broadband Noise Reduction in Injection-Locked Semiconductor Lasers," *IEEE Photonics Technology Letters,* Vol. 7, No. (7), pp. 709-711, (1995).

[3]   T. B. Simpson, J. M. Liu, A. Gavrielides, "Small-Signal Analysis of Modulation Characteristics in a Semiconductor Laser Subject to Strong Optical Injection," *IEEE Journal of Quantum Electronics*, Vol. 32, No. (8), pp. 1465-1468, (1996).

[4]   T. B. Simpson, J. M. Liu, "Enhanced Modulation Bandwidth in Injection-Locked Semiconductor Lasers," *IEEE Photonics Technology Letters*, Vol. 9, No. (10), pp. 1322-1324, (1997).

[5]   J. M. Liu, H. F. Chen, X. J. Meng, T. B. Simpson, "Modulation Bandwidth, Noise, and Stability of a Semiconductor Laser Subject to Strong Injection Locking," *IEEE Photonics Technology Letters*, Vol. 9, No. (10), pp. 1325-1327, (1997).

[6]   N. A. Naderi, M. Pochet, F. Grillot, Y. Li, and L. F. Lester, "Temperature Effects on the Modulation Response of an Injection-Locked InAs/InP Quantum-Dash Laser," *In proceedings of IEEE Conference on Indium Phosphide and Related Material*, pp. 292-294, (2009).

[7] N. A. Naderi, M. Pochet, V. Kovanis, and L. F. Lester, "Bandwidth enhancement in an injection-locked quantum dot laser operating at 1.31-μm," *In proceedings of the Photonics West SPIE*, Vol. 7597, pp. 759719-759719-12 (2010).

[8] N. A. Naderi, M. C. Pochet, F. Grillot, A. Shirkhorshidian, V. Kovanis, L. F. Lester, "Manipulation of the linewidth enhancement factor in an injection-locked quantum-dash Fabry-Perot laser at 1550nm," *In proceedings of IEEE Photonics Society Conference*, pp. 427-428, (2010).

[9] N. A. Naderi, F. Grillot, K. Yang, J. B. Wright, A. Gin, and L. F. Lester, "Two-color multi-section quantum dot distributed feedback laser," *Optics Express*, Vol. 18, No. (26), pp. 27028–27035, (2010).

[10] W. V. Sorin, K. W. Chang, G. A. Conrad, and P. R. Hernday, "Frequency domain analysis of an optical FM discriminator," *Journal of Lightwave Technology*, Vol. 10, No. (6), pp. 787-793, (1992).

[11] J. –G. Provost, and F. Grillot, "Measuring the chirp and the linewidth enhancement factor of optoelectronic device with a Mach-Zehnder interferometer," *In proceedings of IEEE Photonics Society Conference*, pp. 425-426, (2010).

[12] A. Villafranca, J. Lasobras, R. Escorihuela, R. Alonso, and I. Garces, "Time-resolved chirp measurements using complex spectrum analysis based on stimulated Brillouin scattering," *In proceedings of Optical Fiber communication Conference*, pp. 1-3, (2008).

[13] H.-K. Sung, T. Jung, M. C. Wu, D. Tishinin, K. Y. Liou, and W. T. Tsang, "Optical generation of millimeter-waves using monolithic sideband injection

locking of a two-section DFB laser," *In proceedings of IEEE Conference on Lasers and Electro-Optic Society*, Vol. 2, pp. 1005-1006, (2003).

[14] H.-K. Sung, T. Jung, M. C. Wu, D. Tishinin, K. Y. Liou, and W. T. Tsang, "Optical injection-locked gain-lever distributed Bragg reflector lasers with enhanced RF performance," *In proceedings of International Topical Meeting on Microwave Photonics*, pp. 225-228, (2004).

[15] M. Al-Mumin, C. Kim, I. Kim, N. Jaafar, G. Li, "Injection locked multi-section gain-coupled dual mode DFB laser for terahertz generation," *Optics Communication*s, Vol. 275, pp. 186-189, (2007).

[16] H. Page, S. Malik, M. Evans, I. Gregory, I. Farrer, and D. Ritchie, "Waveguide coupled terahertz photoconductive antennas: Toward integrated photonic terahertz devices," *Applied Physics Letters*, Vol. 92, No. (16), pp. 163502(1)-(3), (2008).

[17] M. Tani, Y. Hirota, C. T. Que, S. Tanaka, R. Hattori, M. Yamaguchi, S. Nishizawa and M. Hangyo, "Novel terahertz photoconductive antennas," *International Journal of Infrared and Millimeter Waves*, Vol. 27, No. (4), pp. 531-546, (2006).